Eindhoven University of Technology

MASTER

Design for Ba II 4554 / Hbeta

imaging polarimetry with the Dutch Open Telescope

Snik, F.

Award date:
2005

Design for Ba II 4554 / Hβ imaging polarimetry with the Dutch Open Telescope

Frans Snik
EPG 05-03

f.snik@astro.uu.nl

DOT
DUTCH OPEN TELESCOPE

Universiteit Utrecht

Table of contents

0. Abstract

The Dutch Open Telescope (DOT) simultaneously observes dynamic processes in different layers of the solar atmosphere at high resolution (0.2"). Most of these processes are believed to be driven by magnetic fields. Therefore an additional polarimetric channel for the DOT is designed which will be able to measure the magnetic field topology within the same field of view as the other channels. This new channel is based on an extremely narrow-banded Lyot filter that can be tuned to the ionized Barium line at 4554 Å and the second Hydrogen Balmer line (Hβ; 4861 Å).

The strong Barium line is suitable for the creation of photospheric Dopplergrams due to its high atomic mass. Spectropolarimetric observations show that the circularly polarized profile of Ba II 4554 is surprisingly sensitive to the longitudinal Zeeman effect, which is explained by the steepness of the line wings due to the large atomic mass, possibly in combination with the presence of hyperfine split components in the line wings. More accurate modeling is required to obtain valid inversion curves in both line wings for the longitudinal field strength. The line also yields a significant degree of linear polarization for observations near the limb of the Sun. Depolarization due to the Hanle effect can be utilized to retrieve information on weak magnetic fields. Both the Zeeman effect and the Hanle effect produce polarimetric signals in the chromospheric Hβ line, but the lower signal strengths and the complicated line formation hamper interpretation of the observations.

The Ba II 4554 / Hβ imaging polarimeter is based on liquid crystal variable retarders (LCVRs) as polarization modulators in combination with the Lyot filter's entrance polarizer. The flexibility of the LCVRs is exploited to enable specific wavelength calibration, selection of the coordinate system of linear polarization and first order compensation of instrumental polarization cross-talk. The optical configuration is designed such that the unavoidable instrumental polarization is minimized and constant in time. Spurious polarization signals due to atmospheric disturbances are to a large extent removed with the Speckle reconstruction method. The signal to noise ratio of polarimetric observations can also be significantly boosted by applying demagnification and using longer integration times at the expense of spatial resolution.

The future Ba II 4554 photospheric magnetograms will be able to observe magnetic structures of about 150 km with field strengths down to 100 G. It is expected that Hanle effect observations can be performed at a resolution of about 1". The range of applicability of Hβ imaging polarimetry has to be explored after installation.

F.1.1.

Solar active region 10675, photographed by the Dutch Open Telescope on La Palma on September 29th 2004 at 8:23 UT. The three images are taken cospatially and cotemporally in three different narrow wavelength bands. The color scheme is false. The field of view of these mosaics is 141x106", which amounts to roughly 102x77 Mm on the Sun. For comparison the Earth is depicted at the same scale. The radius of the Sun has an apparent size of about 15' from the Earth. See also the synoptic image of figure 2.3.
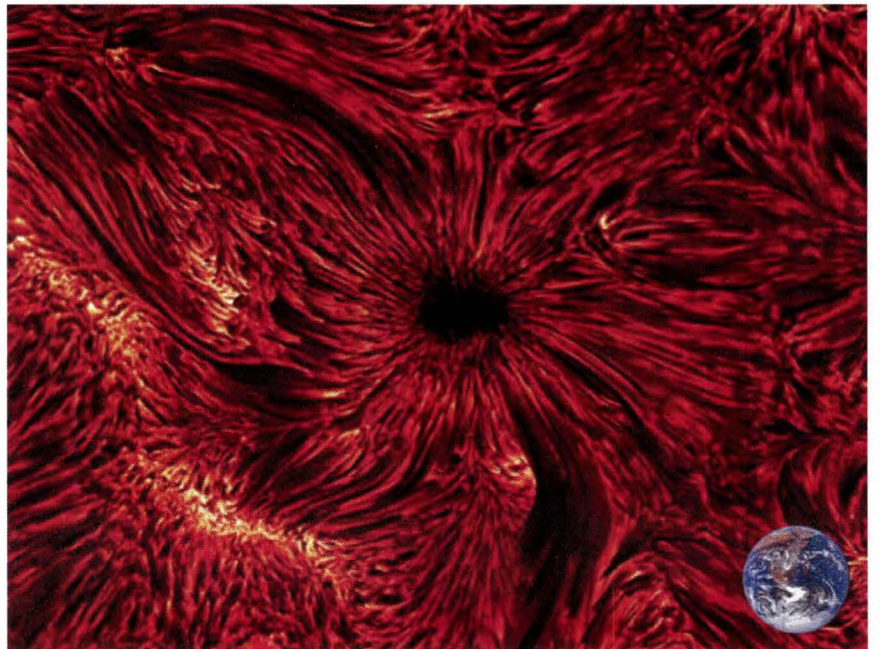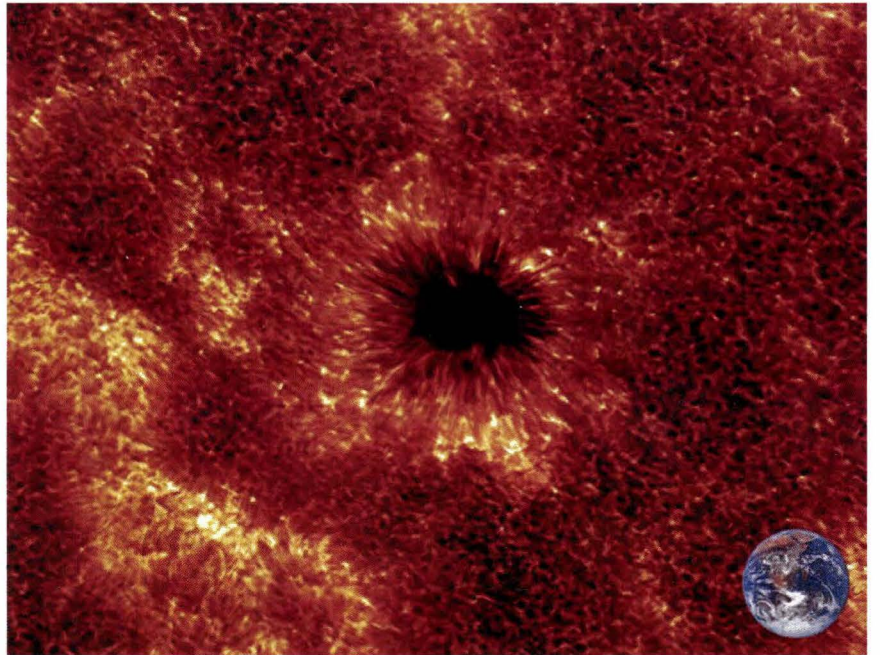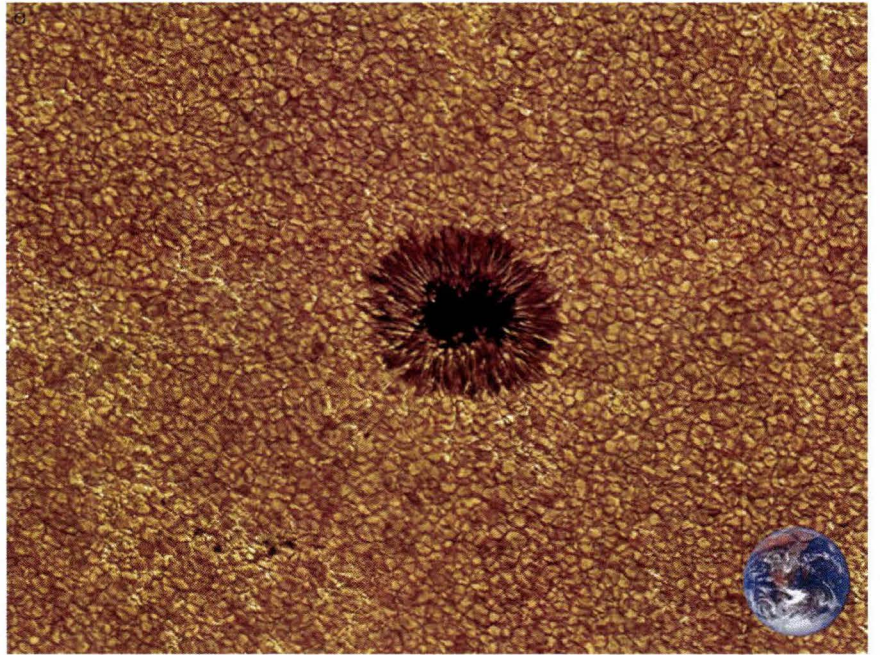
a) The photosphere (G band).
b) The lower chromosphere (Ca II H).
c) The upper chromosphere (Hα).
See text for explanation.

This image sequence featured as February 16th 2005 Astronomy Picture of the Day.

1. Introduction

The Sun is the only star in the universe we can study in great detail. It presents us with a unique opportunity to observe astrophysical plasma phenomena at length scales that are impossible to observe for other stars, and at length and energy scales that are not feasible in a laboratory environment. Furthermore, the Sun is the only celestial body -next to asteroids and meteorites- that has a definite influence on Earth.

Figure 1.1 features three images of the solar atmosphere as observed by the Dutch Open Telescope (DOT; see section 5.1). All three images are taken cospatially and simultaneously on September 9th, 2004. They show active region 10675 in three different narrow wavelength bands.

According to the Eddington-Barbier relation for radiative transfer (e.g. Rybicki & Lightman 1979), photons in an optically thick medium as the Sun escape on average at a location and in a direction of optical thickness unity (or optical depth unity, if the Earth is taken as a reference). In other words, photons can only escape when their mean-free-path becomes larger than the structure ahead of them. In the solar atmosphere the opacity and therefore the optical depth varies with wavelength. Continuum photons escape at a certain radial position where the plasma density allows them to. This layer in the solar atmosphere is called the photosphere (696 Mm from the center of the Sun) and it appears as the 'surface' of the Sun. Here, the heat which is generated by the fusion core and transported by the radiative zone (up to 0.7-0.8 solar radii) and the convection zone, is suddenly radiated into outer space. Therefore, the image of the photosphere (figure 1.1.a) is dominated with the view of the sudden halt of the convection by the radiation loss, called the granulation pattern. The most prominent phenomenon in the photosphere is the occurrence of sunspots: large areas of magnetic flux (up to 4 kG[1,2]) that reduce upwards heat flow. Therefore they are colder (about 4000 °K, compared to the 5800 °K of the surrounding quiet Sun) and appear darker. The central area of a sunspot is called the umbra and it is surrounded by the penumbra, which consists of inclined magnetic flux tubes. The number of sunspots on the face of the Sun varies with a period of eleven years due to the 22 years' magnetic cycle of the solar dynamo.

Figure 1.1.a is an observation of the photosphere at a resolution of 140 km on the Sun. It is taken in a wavelength band around 4305 Å labeled G by Fraunhofer. It consists of many absorption lines of the CH molecule. This molecule dissociates in a kG magnetic environment. Therefore magnetic flux tubes with a diameter of a few hundreds of kilometers appear bright between the granular cells in this image, since the opacity change from the dissociation allow photons from deeper, hotter layers to shine trough, even more than in continuum wavelengths at which opacity reduction is given only by the low gas density in the tubes. (e.g. Keller et al. 2004).

[1.] The correct measure of magnetic fields on the Sun is the magnetic flux density [G]. It is related to the magnetic field strength through the permeability of the medium. For brevity and readability, the magnetic flux density will be addressed as magnetic field strength throughout this report.

[2.] It is more convenient to adopt the Gauss (G) as a unit to measure magnetic fields instead of the SI unit Tesla (=10^4 G). The Ångström (Å) will be used to indicate wavelength, with 1 Å= 0.1 nm.

Generally, at a wavelength of an absorption line of a certain molecule the solar atmosphere has a different opacity than the continuum opacity. Photons from different absorption lines will escape at different altitudes in the solar atmosphere, due to differences in element abundances and atomic level population processes. This way one can observe different layers of the solar atmosphere ('tomography'). The light in the core of one the strongest lines in the solar spectrum (Ca II H at 3968 Å; the resonance line of once ionized Calcium) samples the lower chromosphere at a few hundred kilometers above the photosphere (figure 1.1.b). Here the solar atmosphere looks radically different from the photosphere: the granulation pattern appears reversedly: there are only bright features above the dark intergranular lanes of the photosphere due to local heating in the reversed convection flows (Rutten et al. 2004b, Leenaarts & Wedemeyer-Böhm 2005). Also the magnetic features of the photosphere are more pronounced and spread out here.

A myriad of structures in the upper chromosphere (up to several thousand of kilometers) is revealed by absorption and emission of the red Hydrogen Balmer α line (Hα; 6563 Å) in figure 1.1.c. Hydrogen atoms are of course ubiquitous in the solar atmosphere and both the upper and lower level of the Balmer lines are largely dependent on the radiation field, which largely complicates the interpretation of Hα images. Nonetheless it is clear that structures that follow magnetic field lines dominate the picture. The magnetic fibrils from the sunspot fan out to form a canopy-like structure and the field lines connect at other magnetic elements in the photosphere. The dark structure that spreads out southwards is a small filament, a high arc of 'cold' plasma which strongly absorbs the light from below. Such filaments appear as prominences when observed off the limb of the Sun.

The images of figure 1.1 show a drastic transition from convection-driven phenomena to magnetic phenomena within a mere fraction of a percent of the solar radius. The chromosphere and the million degrees corona, which spreads out to several solar radii, are highly inhomogeneous and dynamic due to their magnetic nature. Many physical processes in the solar atmosphere are driven by magnetic fields on all scales: from the small reconnection events (nanoflares) that are thought to be at least partially responsible for heating the corona to the big X-ray flares and coronal mass ejections, that can cause aurorae, damage satellites, harm astronauts and frequent flyers and even knock out power grids (Quebec in 1989) on Earth. There may even be a connection between solar activity and the Earth's climate (e.g. Krivova & Solanki 2004).

The DOT is able to observe the solar atmosphere at high resolution in the above-mentioned wavelengths. It can maintain its resolution for several hours and track the Sun steadily and without rotation of the image. Figure 1.1 shows that the DOT is able to resolve key magnetic elements that govern dynamic processes on the Sun. This way the DOT provides unique tomographic movies of dynamic processes in the solar atmosphere (to be found at the DOT website http://dot.astro.uu.nl). To get a better understanding of the role of solar magnetism in these processes it is vital to also measure magnetic field strengths and the magnetic topology alongside observations like figure 1.1. Polarimetry is a successful technique to do so. It is therefore a logical step to outfit the DOT with a polarimeter, which will simultaneously map the magnetic fields within the field of view of the current wavelength channels.

This report describes the design of this polarimetry channel. It will operate at two different absorption lines that are reachable by the exceptionally narrow-banded (80mÅ) tunable Lyot filter that will be used (Aleksandrovich et al. 1975, Kushtal & Skomorovsky 2002): the resonance line of ionized Barium (Ba II 4554 Å) and the second Balmer line (Hβ; at 4861 Å). Chapter 2 reviews the physical mechanisms that create polarization and their use for or influence on magnetic field measurements. Chapter 3 focuses on the theoretical background of two spectral lines which the instrument will observe. Also spectropolarimetric measurements in the Barium line are presented and discussed. Chapter 4 gives an overview of the technical issues of building a polarimeter. Chapter 5 describes the instrumental set-up of the DOT in general and the proposed extension for polarimetry in particular. Finally, in chapter 6 conclusions will be drawn about the instrument's capabilities and limitations of measuring magnetic fields.

2. Solar polarimetry

This chapter describes several mechanisms that create polarization in the solar atmosphere. The first section defines the framework of the description of polarization. The second section reviews the different mechanisms and discusses their use for measuring magnetic fields. Also mechanisms with no direct connection with magnetism are mentioned, particularly in the context of magnetic field measurements.

2.1. Polarization formalisms

Polarization is an intrinsic property of an electromagnetic (EM) wave. It is described as the temporal evolution of the electric vector in an inertial plane perpendicular to the propagation direction. Decomposing that vector into its x and y components (z being the propagation direction), The Jones polarization vector is defined as:

E.2.1.
$$\vec{J} = \begin{bmatrix} \hat{E}_x e^{i\varphi_x} \\ \hat{E}_y e^{i\varphi_y} \end{bmatrix}.$$

$\hat{E}_{x,y}$ denote the amplitude of the electric vector in direction x,y and $\varphi_{x,y}$ describe the phase relation between those two vectors during their sine wave propagation with wavelength λ.

For $\varphi_x - \varphi_y = n\lambda$ (n integer) the electric vector propagates in fixed plane through x,y=(0,0) with an angle θ defined as $\tan\theta = \hat{E}_y / \hat{E}_x$. In the reference frame the vector will oscillate on a line with angle θ through the origin. This state of the EM wave is called linear polarization. Note that the state with a certain θ is equal to the state with $\theta+180°$. If $\varphi_x - \varphi_y = (n+\frac{1}{2})\lambda$ linear polarization is created at angle $-\theta$.

If $\hat{E}_x = \hat{E}_y$ and the phase difference equals $\frac{1}{4}\lambda$, the motion of the electric vector in the plane is circular and counterclockwise. This is left-circular polarization. A phase difference of $\frac{3}{4}\lambda$ creates right-circular polarization.

In general, a Jones vector with certain values for and $\varphi_{x,y}$ describes elliptical polarization. Therefore there is no such thing as an unpolarized EM wave, when evaluated at one intersection.

Most photodetectors do not measure the state of the electric vector of the incident EM waves, but just count the photons. Therefore it is more convenient to adopt the Stokes formalism as the preferred way of describing polarization. The Stokes vector is defined as (conform Shurcliff 1962):

E.2.2. $$\vec{S} = \begin{bmatrix} I \\ Q \\ U \\ V \end{bmatrix}.$$

F.2.1.
a) Definition of the Stokes vector. See text for explanation.

$$Q = \updownarrow - \leftrightarrow \qquad I = \updownarrow + \leftrightarrow$$
$$U = \searchvec - \nearrow \qquad = \searchvec + \nearrow$$
$$V = \circlearrowleft - \circlearrowright \qquad = \circlearrowleft + \circlearrowright$$

b) Stokes components sampled by different polarizers.

$$\updownarrow : (I+Q)/2$$
$$\leftrightarrow : (I-Q)/2$$
$$\searchvec : (I+U)/2$$
$$\nearrow : (I-U)/2$$
$$\circlearrowleft : (I+V)/2$$
$$\circlearrowright : (I-V)/2$$

Figure 2.1.a gives a graphical illustration of the different components of the Stokes vector. The Q component is defined as the difference of the photon flux through a linear polarizer at 0 degrees with the flux through a linear polarizer at ±90°. The U component describes the linear polarization at -45° from Q. This way Q and U describe the full two-dimensional state of linear polarization. Stokes V is defined as the difference of flux with right-circular polarization and flux with left-circular polarization.

Stokes I is a measure for the intensity of the beam regardless of polarization. It is therefore defined as the sum of fluxes in two orthogonal polarization states. So I is measured by adding the signal through a polarizer at 0° (+Q) and the signal at ±90° (-Q). It is also measured by adding the signals in +U and –U or +V and –V.

This definition gives a direct operational description for the use of linear and 'circular' polarizers (see chapter 4 for practical examples) to measure the polarization state according to the Stokes formalism. The transmission of each type of polarizer is given in figure 2.1.b. In this formalism polarimetry has become a form of differential photometry.

The useful ratio X/I (with $X=Q,U,V$) is the degree of polarization in 'direction' X. If the incident photon flux is fully polarized (in other words: if all EM waves are equal),

then $I = \sqrt{Q^2 + U^2 + V^2}$.

Just like the Jones vector, the Stokes vector has four components and describes the full polarization state. The difference is that Jones calculus can only describe one EM wave, where Stokes calculus describes the average state of a photon ensemble. Therefore Stokes calculus is not adequate to handle interference effects. In the Jones calculus the modification of the polarization vector is described by 2x2 matrices.

8

Those matrices can be transformed into 4x4 Mueller matrices M, which are applied on the Stokes vector:

E.2.3. $\vec{S}' = M \cdot \vec{S}$.

For instance, the Mueller matrices for complete polarizers in direction +Q and –Q are given by:

E.2.4. $\frac{1}{2}\begin{pmatrix} 1 & 1 & 0 & 0 \\ 1 & 1 & 0 & 0 \\ 0 & 0 & 0 & 0 \\ 0 & 0 & 0 & 0 \end{pmatrix}, \frac{1}{2}\begin{pmatrix} 1 & -1 & 0 & 0 \\ -1 & 1 & 0 & 0 \\ 0 & 0 & 0 & 0 \\ 0 & 0 & 0 & 0 \end{pmatrix}$.

The matrices for U and V are obtained when swapping components with subscripts i=2 or j=2 with i=3,4 and j=3,4.
Pure reflections will mirror the positive direction of rotation in the coordinate systems of Q, U and V. The corresponding Mueller matrix is:

E.2.5. $\begin{pmatrix} 1 & 0 & 0 & 0 \\ 0 & -1 & 0 & 0 \\ 0 & 0 & 1 & 0 \\ 0 & 0 & 0 & -1 \end{pmatrix}$ or $\begin{pmatrix} 1 & 0 & 0 & 0 \\ 0 & 1 & 0 & 0 \\ 0 & 0 & -1 & 0 \\ 0 & 0 & 0 & -1 \end{pmatrix}$.

The axis of Q (and therewith also U) can be freely chosen. It is therefore useful to describe a rotation of the coordinate system by angle α with Mueller matrices:

E.2.6. $R(\alpha) = \begin{pmatrix} 1 & 0 & 0 & 0 \\ 0 & \cos 2\alpha & \sin 2\alpha & 0 \\ 0 & -\sin 2\alpha & \cos 2\alpha & 0 \\ 0 & 0 & 0 & 1 \end{pmatrix}$.

If the beam traverses n components that affect the polarization state with Mueller matrix M_n, the Stokes vector of the emergent beam is:

E.2.7. $\vec{S}' = M_n M_{n-1} M_{n-2} ... M_3 M_2 M_1 \cdot \vec{S}$.

A medium with multiple components that modifies the polarization state (such as a layer of the solar atmosphere or a polarimetric instrument) can therefore be described with a single Mueller matrix M_{total}, defined as the product of the matrices of its components. Therefore, both full Stokes radiative transfer calculations on the Sun and analysis of instrumentation are performed in the Stokes formalism.
In general the Mueller matrix of an instrument looks like this:

E.2.8. $M_{instr} = \begin{pmatrix} I \to I & Q \to I & U \to I & V \to I \\ I \to Q & Q \to Q & U \to Q & V \to Q \\ I \to U & Q \to U & U \to U & V \to U \\ I \to V & Q \to V & U \to V & V \to V \end{pmatrix}$.

The diagonal elements describe the transmission of the Stokes components. All off-diagonal elements describe cross-talk between the different Stokes components. As seen in equation 2.6, the elements Q↔U indicate rotation of the direction of linear polarization. The elements I↔X point to (partial) polarization or depolarization in direction X (conform equation 2.4). The elements Q,U↔V describe a transition from linear to circular polarization (and vise versa) and therefore indicate phase retardation between the two components at ±45° from Q or U.

Chapter 4 gives an extensive overview on the physical backgrounds of the elements in the instrumental Mueller matrix. The next section focuses on the creation and modification of polarization in the solar atmosphere.

2.2. Polarization effects in the solar atmosphere

Trujillo Bueno (2003a) has derived an Eddington-Barbier-like relation for polarized radiative transfer, which shows that the degree of polarization of photons from the solar atmosphere in direction X is approximately equal to the fractional polarization in direction X that is created at optical depth unity (neglecting selective absorption effects and magneto-optical effects, see sections 2.2.2 and 2.2.4). So next to information contained in regular spectra (temperature stratification, Doppler shifts, broadening by turbulence, etc.) it is also advantageous to analyze the polarization state of solar photons. The next sections show that particularly magnetic fields create and modify polarization.

2.2.1. Zeeman effect

The Zeeman effect was discovered in a laboratory. It involves the splitting of spectral lines in the presence of magnetic fields. The effect is explained in terms of energy differences between the degenerate sublevels of a quantum level with quantum number J (due to Russel-Saunders coupling of the angular momentum quantum number L and the spin quantum number S), caused by the interaction of the sublevel's magnetic moment with the magnetic field vector. Such a level with quantum number J is split into (2J+1) sublevels according to:

E.2.9.   a) $\Delta E_Z = \mu_B g_L m_J |B|$

b) $\Delta \lambda_Z = \dfrac{\mu_B}{hc} g_L m_J \lambda^2 |B|$,

with μ_B the Bohr magneton, h Planck's constant, c the speed of light, g_L the Landé factor for that quantum level and m_J the quantization of the angular momentum in the direction of the magnetic field.

For polarization effects due to the Zeeman effect it is instructive to adopt a simple three-dimensional oscillator model for a triplet transition with J=1 for the upper level and J=0 for the lower level (see figure 2.2.a).

The oscillator is oriented to the magnetic field vector and the oscillators in the x and the y direction are coupled. This coupling due to the magnetic field indicates Larmor precession of the magnetic moments of the two upper sublevels with $m_J=\pm1$. They will precess circularly around the field vector counterclockwise and counterclockwise respectively with frequencies $\omega_0 \pm \omega_L$, the latter component being the Larmor frequency. In accordance with equation 2.9.a, radiation from the transitions with $\Delta m_J=1$ will be blueshifted in the direction of the field vector. Radiation with $\Delta m_J=-1$ is redshifted. The components with $\Delta m_J=\pm1$ are called σ components (after "senkrecht", which is German for perpendicular). In connection with their precession, the σ components are circularly polarized in the direction of the field vector. Therefore an observer on a line of sight coincident with the field direction will see left-circular polarization in the blue wing of the line and right-circular polarization in the red wing. In Stokes V, the spectral profile will have an antisymmetric profile around line centre. An observer of an opposite polarity field (figure 2.2.b) will see the negative profile. For zero field the positive and negative circular polarization profiles are not shifted in wavelength and therefore cancel out to an unpolarized signal in Stokes V. For higher fields, a lesser fraction of both circular polarization signals is cancelled and the profile in Stokes V becomes stronger and broader. This effect is called the longitudinal Zeeman effect.

The third upper sublevel (the z oscillator) will oscillate parallel to the field vector and is therefore called the π component. Radiation from the transition with $\Delta m_J=0$ will be linearly polarized in a direction perpendicular to the magnetic field vector. In that direction the σ components are seen edge-on, so their emergent polarization will also be linearly polarized, but in the direction perpendicular to the linear polarization from the π component. With +Q defined parallel to the field vector, the spectral profile in Stokes Q will be symmetric with respect to line center: positive polarization is created in the center and negative polarization in the wings. Analogous to the longitudinal Zeeman effect, the profiles of the transverse Zeeman effect will get stronger and broader with increasing field. The combination the profiles in Stokes Q and U can determine the azimuth angle of the magnetic field vector. For example, there is a sign change in Q when the transverse field rotates by 90°. There is an 180° ambiguity of this measurement due to the fact that a field in opposite direction will show the exact same linear polarization profiles (compare figures 2.2.a and 2.2.b).

F.2.2.
Oscillator model for the emergent polarization of a triplet transition due to the Zeeman effect
a) for a positive polarity field,
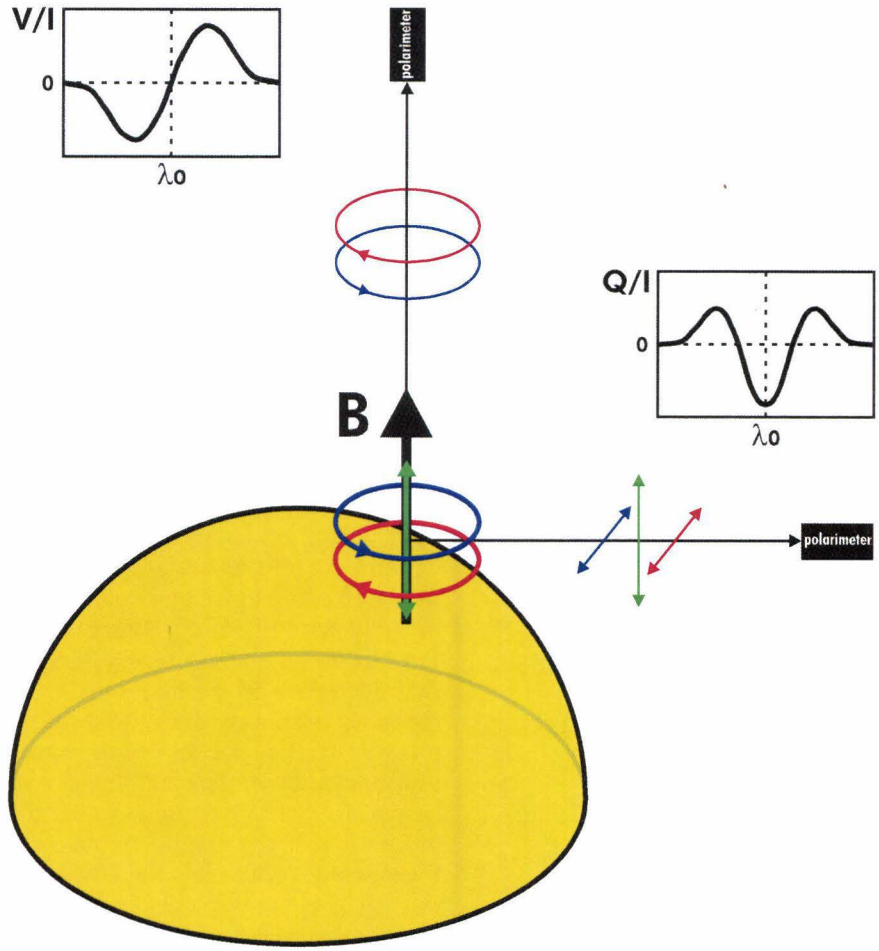
b) for a negative polarity field.
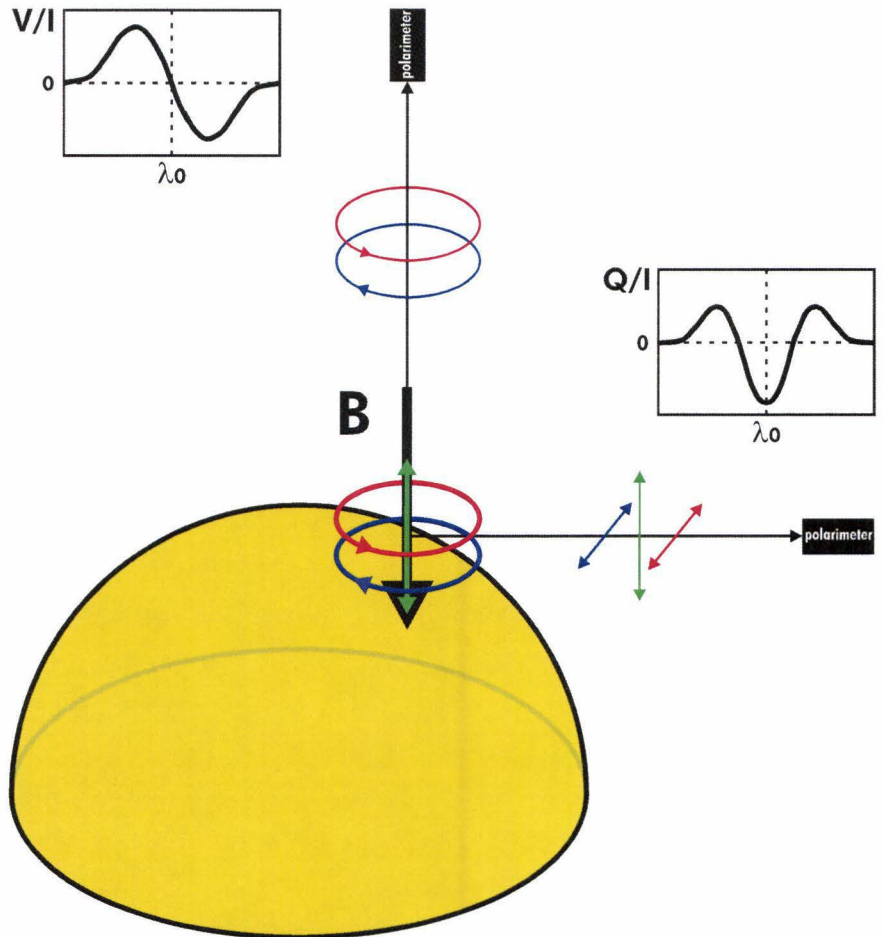
A full quantum-mechanical treatment of the polarized line formation in a magnetic field is given by Landi degl'Innocenti & Landi degl'Innocenti (1973) and Jefferies etal. (1989). For a magnetic splitting smaller than the broadness of the line (mostly due to Doppler broadening), a simplified first order relation of the Stokes parameters is given by:

E.2.10.   a) $Q(\lambda) = -\left(\dfrac{\mu_B}{2hc} g_L \lambda^2\right)^2 \dfrac{d^2 I}{d\lambda^2} B \sin^2 \gamma \cos 2\chi$,

b) $U(\lambda) = -\left(\dfrac{\mu_B}{2hc} g_L \lambda^2\right)^2 \dfrac{d^2 I}{d\lambda^2} B \sin^2 \gamma \sin 2\chi$,

c) $V(\lambda) = -\dfrac{\mu_B}{hc} g_L \lambda^2 \dfrac{dI}{d\lambda} B \cos \gamma$,

with γ the inclination and χ the azimuth angle of the field vector with respect to the line of sight. In this weak field approximation the profiles in Q and U are linearly dependent on the transverse field strength and the second derivative of the unpolarized line profile. The ratio of U and Q is equal to tan2χ, which determines the field azimuth (with 180° ambiguity).

The Stokes V signal is linearly dependent on the line of sight field strength and the first derivative of the line profile. Equation 2.10.c is the so-called magnetograph formula. It tells us that a measurement of the circular polarization is a direct measurement of the line of sight magnetic polarity and field strength if the line profile is known. Stokes V images taken in the wing of a Zeeman sensitive line (where $dI/d\lambda$ has an extremum) are therefore called magnetograms (see the example of figure 2.3). The magnetogram formula harbors a first order term and therefore the signal level reaches the 10% range for relatively weak fields (a few hundred Gauss). The quadratic dependence on the wavelength shows that it pays of to do Zeeman measurements in the red or infrared as the dependence of the Doppler broadening on the wavelength is only linear.

F.2.3.
Synoptic magnetogram on September 29th 2004 by the MDI instrument on the SOHO satellite. The regions of large positive or negative signal coincide with active region. Note the reversed polarities of active regions on both hemispheres due to the solar dynamo and the intermittent fields in quiet regions.
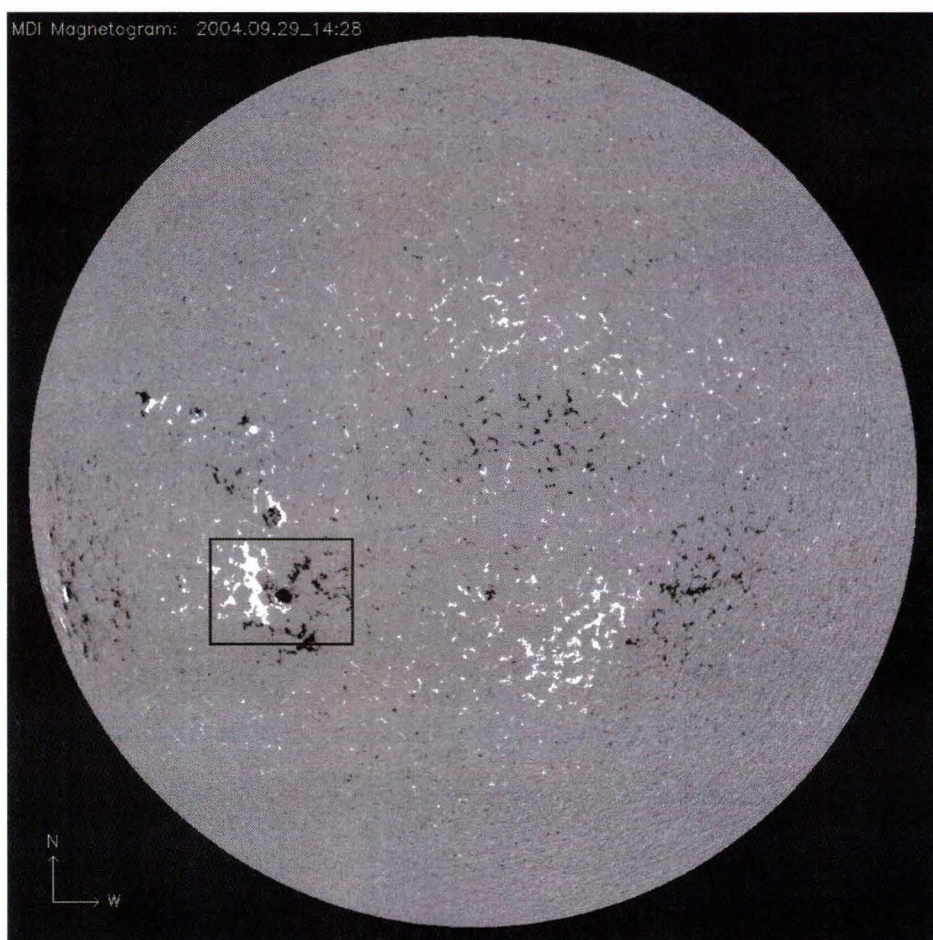
The transverse Zeeman effect is a second order effect and therefore the signal level is much lower than that of magnetograms. Full Stokes measurements enable inversion of the full magnetic field topology, but it requires sufficient polarimetric sensitivity and spectral information, either through line scans of a tunable filter or by slit-jaw scans of a spectrograph. The resulting maps of magnetic field strength, direction and polarity are called vector magnetograms.

Due to the selection rules of electric dipole transitions, any transition with an upper or lower level of degeneracy >3 will consist of σ and π components. The magnetograph formula is still valid when utilizing the effective Landé factors for the total of the σ and π components conform Landi degl'Innocenti (1982). The effective Landé factors are weighted averages of the individual Landé factors of the sublevels of the particular transition.

A field topology with opposite polarities within a resolution element will cause cancellation of the regular magnetogram signal, which still constitutes a correct measurement of the line of sight magnetic flux. Due to the 180° ambiguity, the transverse Zeeman effect still generates a signal for opposite polarity fields.
If only a fraction f (called the filling factor) of the resolution element is permeated by a magnetic field, the emergent Stokes vector is composed of both a magnetic and a non-magnetic signal. The ratio of two lines that are formed under the same conditions, but with different Zeeman sensitivity, allows one to infer that filling factor (Stenflo 1994). This way, magnetic structures smaller than the observation's spatial resolution can be analyzed.

Jefferies & Mickey (1991), Cauzzi et al. (1993) and Graham at al. (2002) have shown that the magnetograph formula accurately retrieves the longitudinal field strength within 20% for fields smaller than 3.5 kG/g_L for typical solar lines. For a Zeeman splitting larger than the Doppler broadening, the magnetogram signal will undergo Zeeman saturation (Stenflo 1994), which causes a severe underestimate of the field strength.
The center of gravity method by Semel (see Rees & Semel 1979) allows a more accurate retrieval of strong fields, as it is sensitive to both the strength of the Stokes V signal and blue- / redshifts of the profile. The center of gravity from line center of the profile of ½(I±V) -the signal obtained by the circular polarizers of figure 2.1.a- is defined as:

E.2.11.
$$\Delta\lambda_{r,l} = \frac{\int_{-\infty}^{\infty}[I_c - (I(\lambda) \pm V(\lambda))]\Delta\lambda d(\Delta\lambda)}{\int_{-\infty}^{\infty}[I_c - (I(\lambda) \pm V(\lambda))]d(\Delta\lambda)} = \mp \frac{\int_{-\infty}^{\infty}V(\lambda)\Delta\lambda d(\Delta\lambda)}{\int_{-\infty}^{\infty}(I_c - I(\lambda))d(\Delta\lambda)},$$

for even and odd functions for I(λ) and V(λ) respectively. I_c is the intensity of the nearby continuum. The longitudinal magnetic field is then retrieved by:

E.2.12.
$$B_{LOS} = \frac{hc}{\mu_B}\frac{1}{g_L\lambda^2}\Delta\lambda_l.$$

Cauzzi et al. (1993) and Uitenbroek (2003) show that this method is accurate within about 10% for solar magnetic fields and that it is independent of spectral resolution. However, for strong fields (>1.5 kG) the presence of the π component in the I-profile gives rise to an underestimate of the field strength.

The presence of large magnetic and velocity gradients, lead to deviation from the (anti-) symmetry of the profiles in I and V, especially in strong lines with a range of formation heights along the line wing. This also limits the validity of both the weak field and the center of gravity method for retrieving the longitudinal field.
Solanki et al. (1987) proved that formulae 2.10.a and b are not useful for an accurate determination of the transverse field vector. It is therefore necessary to adopt more intricate inversion models based on full Stokes radiative transfer with specific model atoms and model atmospheres to accurately retrieve the full magnetic vector at optical depth unity.

Some atomic nuclei have a non-zero value of its magnetic moment, which is indicated by quantum number I. In the absence of external magnetic fields, the quantum number J will interact with this nuclear magnetic moment I and form a new quantum number F $(=|J-I|...(J+I))$, which now governs the electronic energy levels. This hyperfine splitting (HFS) is destroyed by increasing the external magnetic field until J and I are valid individual quantum numbers again (the Back-Goudsmit effect). Lopez Ariste et al. (2002) showed that spectral lines subject to hyperfine splitting have anomalous Stokes spectra for weak fields. The hyperfine splitting can cause net circular polarization when integrating over the entire Stokes V-profile. This behavior is a useful diagnostic for low field strengths ($<\sim 1$ kG) to which the ordinary Zeeman effect is not particularly sensitive.

A further increase of the field strength to the so-called Paschen-Back regime will eventually also destroy the L-S coupling. For typical magnetic field strengths only the quantum states of molecules and light atoms as Hydrogen or Helium have to be described with the incomplete Paschen-Back effect (Socas-Navarro 2004, Asensio Ramos et al. 2005).

2.2.2. Hanle effect

Also the Hanle effect was discovered in a laboratory. This effect is associated with the creation of linear polarization in scattered light from an anisotropically illuminated atom. Figure 2.4.a illustrates this effect with an oscillator model for the high solar atmosphere (conform Trujillo Bueno 2001).

In this case the oscillator only receives light from below and therefore there is a certain degree of anisotropy in the illumination. It is assumed that the radial radiation of the Sun is unpolarized and can be represented by two orthogonally polarization states, that drive the oscillator. It is clear that coherently scattered light at 90° is linearly polarized in the direction parallel to the solar limb.
The presence of a vertical magnetic field does not influence this effect (figure 2.4.b). In this case it is more convenient to consider the unpolarized unidirectional pumping beam to be a superposition of left- and right-circular polarization states.

In the framework of quantum-mechanics anisotropic pumping of an atom in a vertical field will create population imbalances in the substates of a level with a degeneracy of at least three. This effect is illustrated in figure 2.5 for a transition with J_u=1 and J_l=0.

F.2.5.
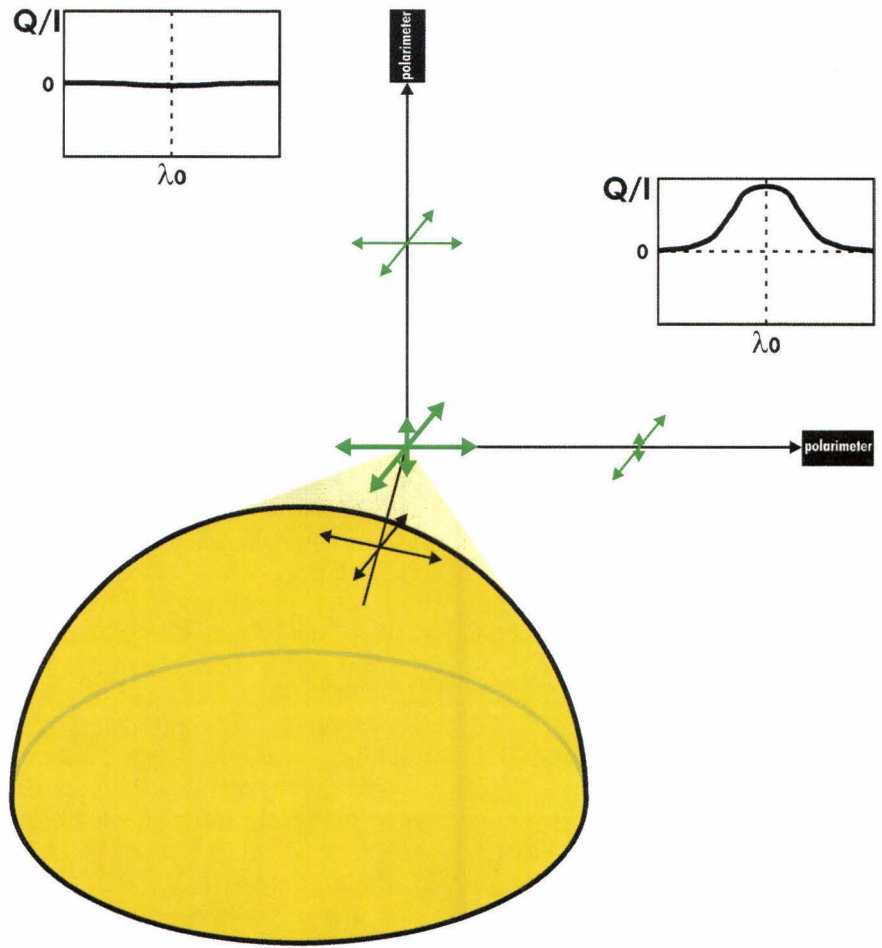The creation of population imbalances in upper level quantum level substates by anisotropic illumination conform figure 2.4.b.

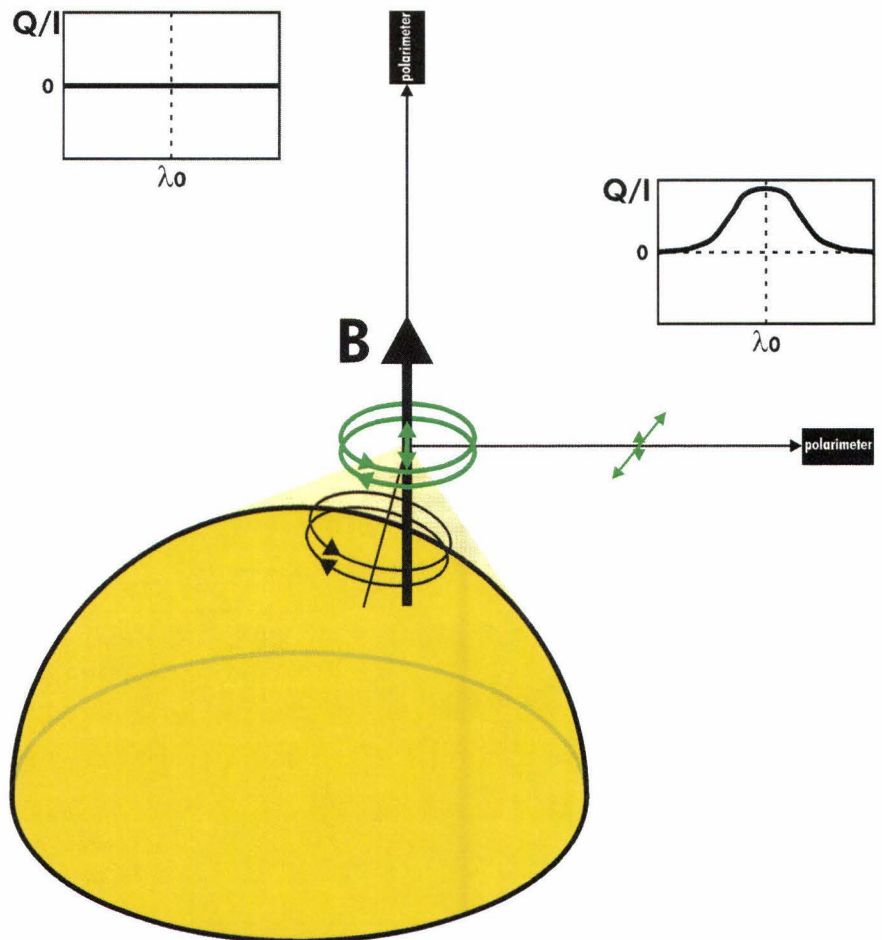$$m_J = -1 \qquad m_J = 0 \qquad m_J = 1$$

$$m_I = 0$$
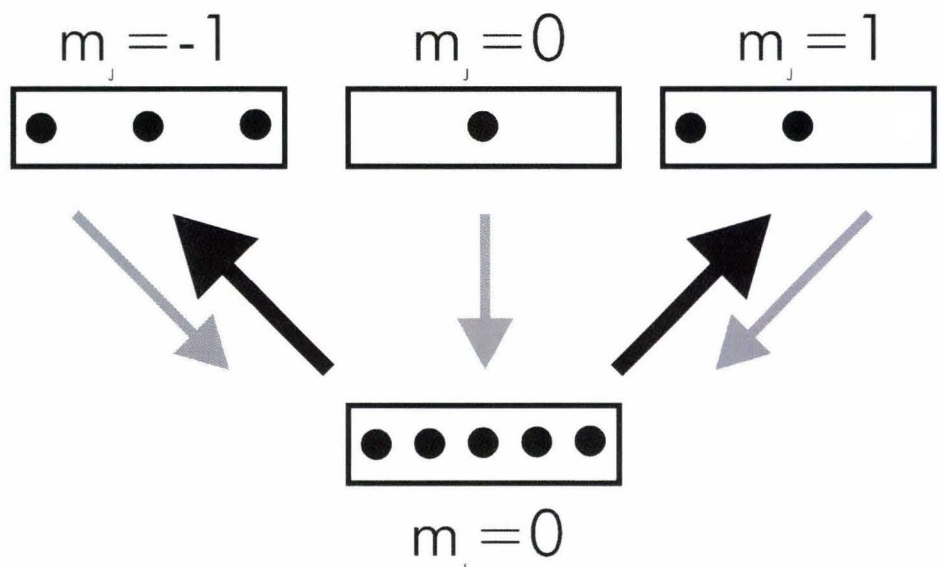
F.2.4.
Oscillator model for the creation of scattering polarization due to anisotropic illumination in the solar atmosphere
a) at zero field

b) in the presence of a vertical field.
Adopted from Trujillo Bueno (2001)

15

The circularly polarized components of the radiation are only absorbed by σ transitions and therefore the upper substates with $m_j = \pm 1$ will be populated to a larger extent than the $m_j = 0$ substate.

This atomic alignment can also be created in degenerate lower levels by means of depopulation pumping and polarization of one level can be transferred to the other level through repopulation pumping. The emergent polarization depends largely on the orientation of the magnetic quantum numbers (see below). States with $J=0$ or $J=\frac{1}{2}$ are intrinsically unpolarizable.

The amount of 'order' of a quantum level can be quantified by the density matrix of the mixed state of the level. The off-diagonal components of the density matrix describe the coherences between the different substates. The matrix is diagonal for a state with no atomic alignment.

Scattering polarization is observed on the Sun for lines with sufficient degeneracy and formation height, when observed at the limb of the Sun. Here, the emergent light is mostly light scattered at angles near 90° and furthermore the amount of anisotropy is higher due to limb darkening[3] Its dependence on radiation that originates elsewhere makes the formation of scattering polarization a particularly non-local process.

The spectral signatures in Stokes Q (with +Q taken parallel to the limb) observed near the limb of the quiet Sun look very different compared to the regular solar spectrum and is therefore referred to as the "second solar spectrum" (Stenflo & Keller, 1997). Both spectra of the Na D lines are given in figure 2.6. The degree of polarization of the second solar spectrum is very small (usually <<1%), because the anisotropy is very small. A full interpretation of the signals will be given below, but it is already obvious that the polarization profile of Na D2 is very different with respect to the D1 profile, due to the quantum numbers of the transitions.

F.2.6.
The regular spectrum and the "second solar spectrum" of the Na D lines, observed at $\cos\theta = xx$ (with θ the heliocentric angle). Taken from Stenflo & Keller (1997).

1 Na I D_2 and D_1

---
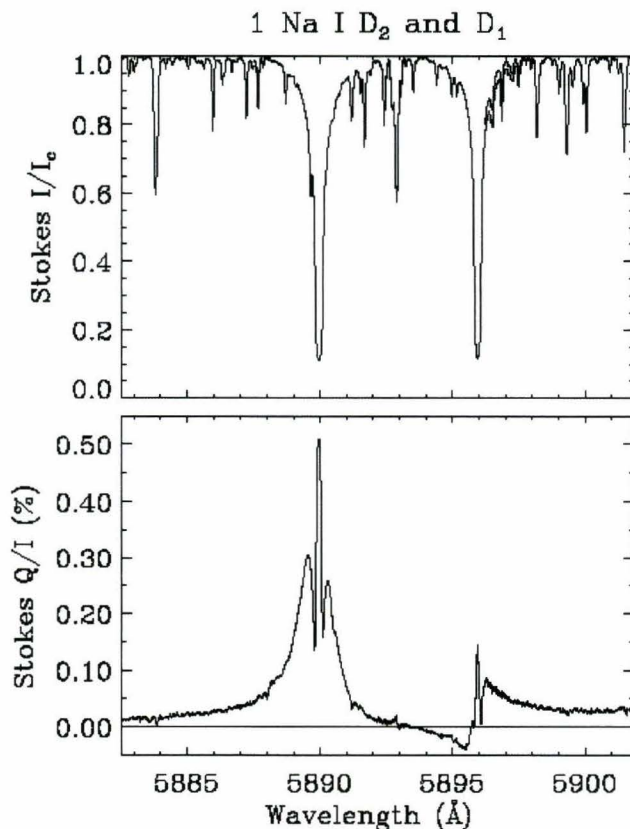
[3] The limb appears darker because optical depth unity is reached at a higher location in the solar atmosphere, due to the transport at an angle. The intensity of the light is lower due to the negative temperature gradient.

The oscillator model of figure 2.4 in the presence of
a) a horizontal field perpendicular to the line of sight,
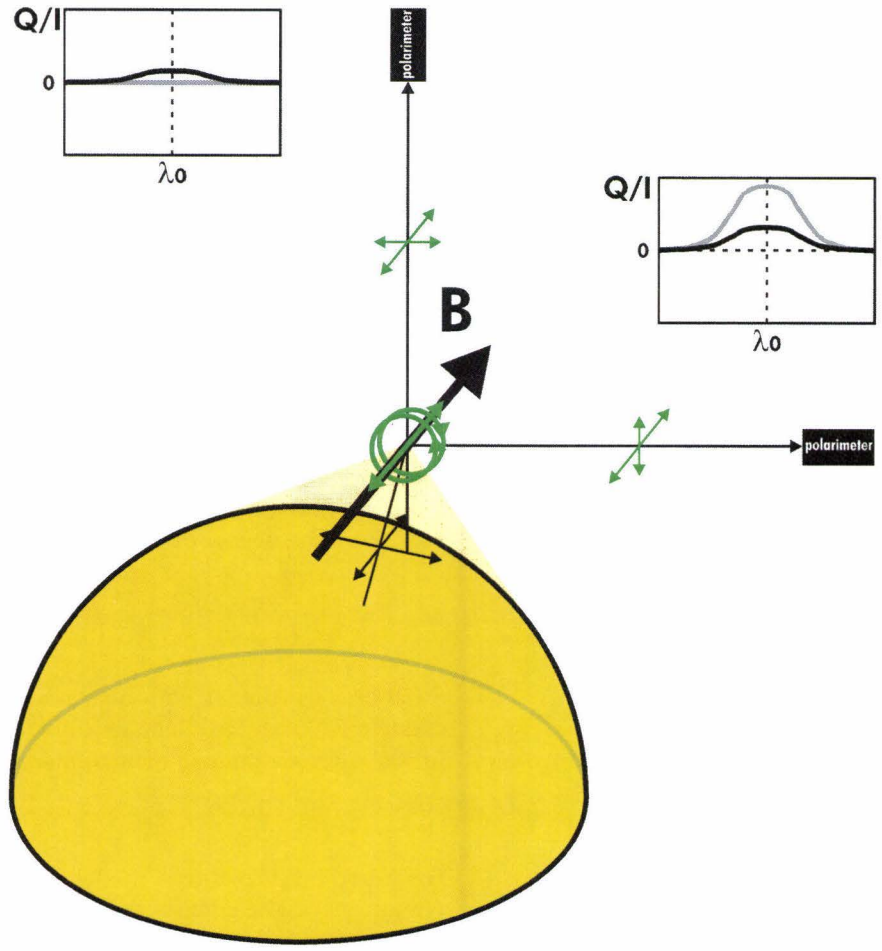
b) a horizontal field parallel to the line of sight.
The Hanle effect reduces and rotates the linear polarization create by coherent anisotropic scattering.
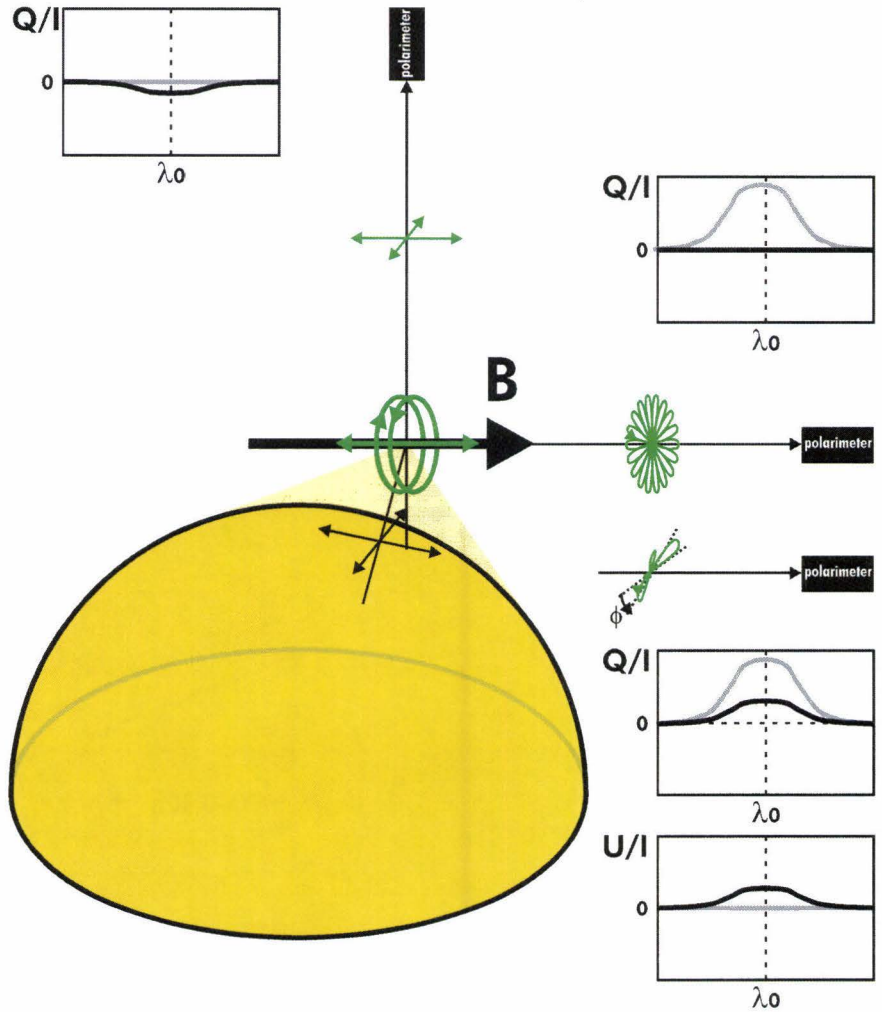
The Hanle effect itself involves modification of scattering polarization by weak magnetic fields. Consider the same oscillator model as in figure 2.4 in the presence of horizontal fields as indicated in figure 2.7.

Just like with the Zeeman effect, the magnetic field couples the oscillators perpendicular to the field direction and with it it orientates the σ and π components. First consider the field topology of figure 2.7.a. The induced polarization in the y direction is now coupled to the z direction, which leads to depolarization down to $1/3$ of the original linear polarization degree for $90°$ scattered radiation. The forward scattered light, however, now is linearly polarized parallel to the field direction due to the reduction of signal in the y direction.

The case of figure 2.7.b also creates linear polarization parallel to the field direction for forward scattering. The polarization at $90°$ is fully dominated by the induced polarization in the x oscillator and its evolution due to the rotation of the coupled x-z oscillator. The linear polarization with frequency ω_0 is rotated through the plane by the two circular oscillator with frequencies $\omega_0 \pm \omega_L$. If there is no damping, the resulting polarization degree in the y direction is therefore zero.

If a finite damping time is applied to the oscillation, the depolarization will not be complete. The degree of polarization is reduced to:

E.2.13.
$$Q_{obs} = \frac{Q_{max}}{\sqrt{1 + \left(2\omega_L t_{life}\right)^2}} .$$

Furthermore the direction of maximal polarization degree will be rotated counterclockwise for a magnetic field pointing towards the observer and clockwise for the opposite polarity. The rotation angle is given by:

E.2.14.
$$\tan 2\varphi = 2\omega_L t_{life} .$$

For a two-level quantum model the damping time of the oscillator is associated with the natural lifetime of the level involved in the transition. Equating this lifetime to the period of the Larmor precession this leads to the general formula for magnetic fields up to which the Hanle effect is sensitive:

E.2.15.
$$\frac{e}{2m_e} g_L B \approx 10^6 g_L B[G] = \frac{1}{t_{life}} .$$

This behavior can also be illustrated by looking at the coherences between the Zeeman substates. These coherences preserve the induced atomic alignment and are significant in regions of overlapping sublevels. Figure 2.8 depicts the evolution of a J=1 level in a magnetic field.

F.2.8.
The Zeeman splitting of a J=1 level with natural broadening $h/2\pi t_{life}$. From Rees (1982).
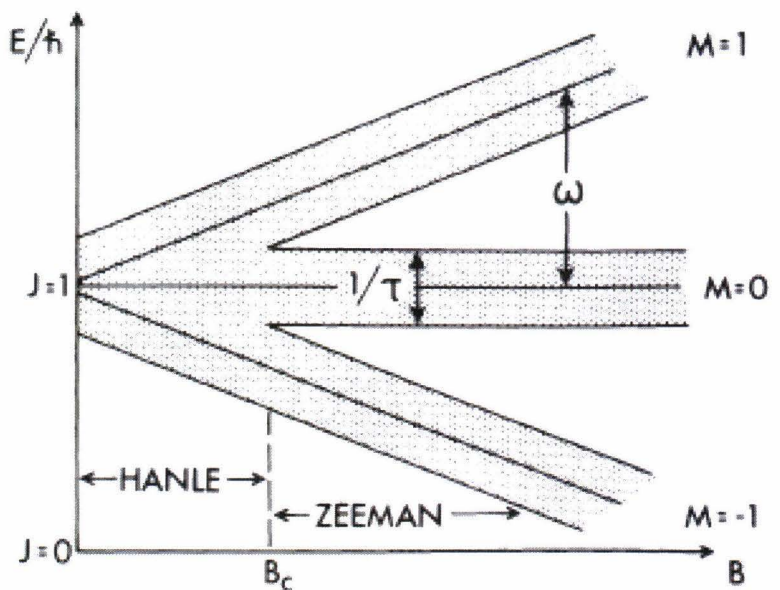
The natural broadening E (due to Heisenberg's energy-time uncertainty principle) of each of the sublevels is equal to $h/2\pi t_{life}$. Therefore, according to equation 2.9.a the Zeeman sublevels only overlap for magnetic fields smaller than the magnitude that is given by equation 2.15. In this regime the coherences maintain the induced atomic alignment.

Typically the upper level of a dipole transition has an Einstein A coefficient of 10^7-10^8 s^{-1}. The magnetic fields to which the Hanle applies are therefore of the order of 10-100 G. Lower levels and especially metastable ground levels tend to have longer lifetimes and are therefore already sensitive to sub-Gauss fields.

A field topology conform figure 2.7.a will not completely depolarize the signal, also for fields larger than the field indicated by equation 2.15. For fields higher than the field strength indicated by equation 2.15 the degree of polarization is sensitive to the field orientation and not its strength. Only collisions can fully destroy the coherences between the sublevels.

Comparing figure 2.4.b and 2.7.a shows that there is also a 90° ambiguity of the polarization direction relative to the magnetic field direction. At an angle of 54,7° (the Van Vleck angle) between the direction of anisotropic radiation and the magnetic field vector the induced atomic alignment is zero (House 1974). For angles smaller than the Van Vleck angle the polarization direction is perpendicular, for larger angles the polarization direction is parallel to the field.

The oscillator model indicates that in general mixed polarity turbulent fields will induce depolarization with respect to the field-free 90° scattering case. If Stokes Q is chosen to be parallel to the solar limb, any signal in Stokes U will then be due to line of sight fields if the transverse Zeeman effect can be neglected.

By measuring and modeling the second solar spectrum of the Sr 4607 line at various positions on the disk Trujillo Bueno et al. (2004) were able to infer a turbulent field strength of 130 G for the quiet Sun and concluded that a significant fraction of the Sun's magnetic energy is contained in such field configurations. As this turbulent field strength varies with the solar cycle, also the signal strength of the second solar spectrum varies with the solar cycle (Bommier & Molodij 2002).

With models for the creation and modification of linear polarization, Landi degl'Innocenti (1998) was able to explain the linearly polarized signals of the Na D lines (figure 2.6). The coherences due to the many HFS level crossings of the upper level of the D2 line cause the high polarization degree. It was proven that the metastable lower level alignment has a definite influence on the profile of the D1 line. This led to the conclusion that no canopy-like horizontal fields can be present to depolarize this level. However, Trujillo Bueno et al. (2002a) showed that lower level coherences are not completely destroyed when horizontal fields are present.

As shown in the oscillator models of figure 2.7, linear polarization can be created by selective absorption (dichroism) of forward scattering radiation. This effect is indeed observed for transitions with a polarizable lower level (Trujillo Bueno et al. 2002b). In contradiction to the selective emission due to the Hanle effect, selective absorption creates polarization with increasing field strength. However, this lower level Hanle effect is an order of magnitude smaller than the regular Hanle effect and also the Van Vleck effect hampers the interpretation of the signals.

The Hanle effect is a successful technique to characterize the magnetism of the quiet Sun. It is also used to measure the field strength of prominences (e.g. Casini et al 2005, López Ariste et al. 2005), filaments (Lin et al. 1998) and of chromospheric magnetic foot-points at supergranular boundaries, which at the limb appear as spicules (e.g. Trujillo Bueno et al. 2005).

It is clear that the Hanle effect is mostly complementary to the Zeeman effect. While the Zeeman effect produces polarization with increasing field strength, the Hanle effect involves depolarization. The Hanle effect is purely in the domain of coherent scattering physics, while the Zeeman effect also is present for levels that are collisionally populated. Furthermore, both effects have their own field regimes (see figure 2.8): the Zeeman effect is sensitive to stronger fields (>100 G) than the Hanle effect. Particularly the transverse Zeeman effect -being a second order effect- has a very limited influence on the linear polarization signals of the Hanle effect (Trujillo Bueno 2001). Also, the Hanle effect is more sensitive to turbulent field topologies. For measurements of weak line of sight fields, the first order magnetograms (equation 2.10.c) and Hanle measurements are fully complementary.

It is easy to distinguish between both effects, when observing in two lines with known Zeeman sensitivities and with different signals in the second solar spectrum. Stenflo et al (2002) used both Na D lines to spatially map the Zeeman and Hanle signals caused by the magnetic field topology near the solar limb.

Landi degl'Innocenti & Bommier (1993) showed that the Hanle contribution to the transverse Zeeman effect in a heavily scattering transition (a transition with an upper level with a small lifetime) can be used to solve the 180° ambiguity.

2.2.3. Beam impacts

Not only anisotropic radiation, but also a unidirectional beam of particles induces atomic alignment. The degree of emergent polarization depends on the energy of the colliding particles and on the angle of observation (Vogt & Hénoux 1996). The angular momentum of the beam along the propagation direction is assumed to be zero. For particles with energies only slightly higher than the excitation energy, the velocity and thus the angular momentum of the particle after the collision is negligible. Therefore only the transitions that do not harbor any angular momentum (the π components) will be excited. With increasing beam energies the main velocity variation after the collision is perpendicular to the beam direction, so in order to conserve the angular momentum also the σ components will be increasingly populated.

An observer with a line of sight perpendicular to the beam direction will see a positive Stokes Q signal for low energy beams and a negative Q signal for high energies, if +Q is chosen parallel to the beam direction. At a certain turnover energy the degree of polarization is zero.

Various observers report on beam impact polarization of 2-20% in both positive and negative Stokes Q (when taken parallel to the solar disk radius) due to flares (Vogt & Hénoux 1999, Firstova et al. 2003, Hanaoka 2003) and in smaller reconnection events as Ellerman bombs (Zharkova & Kashapova 2005), which are all observed in Hα. In these cases of magnetic reconnection in the corona, both electrons and protons are accelerated. These beams cause intense heating down to the formation height of Hα. Model calculations by Vogt & Hénoux (1996) show that only protons above the 100 keV energy range maintain a non-zero degree of anisotropy down to this height. Isotropic collisions with thermal electrons will considerably depolarize the upper level of the transition (Sachal-Bréchot at al. 1996).

Polarimetry of flares is very susceptible to spurious signals, which are caused by the large spatial and temporal gradients during the flare. In recent measurements Bianda et al. (2005) found no sign of linear polarization in a wide range of flares at different disk positions with the very accurate ZIMPOL instrument (see chapter 4). Therefore they raise the question if there is any degree of anisotropy of proton beams at the Hα formation level.

2.2.4. Other polarization effects

A well-known polarization effect is Faraday rotation of linear polarization of radiation propagating parallel to the field direction. This effect will cause an erroneous interpretation of the field azimuth angle in sunspot penumbrae (Makita 1985, Ye & Jin 1987, Su & Zhang 2004). In polarized radiative transfer models this effect countered with the inclusion of magneto-optical effects in the propagation Mueller matrix.

The Faraday effect is useful to measure the low field strengths in the corona by observing the rotation of linear polarization of an (artificial) radio source through the corona. The transverse Zeeman effect of 'forbidden' coronal lines (magnetic dipole transitions) is treated in terms of single scattering events (House 1974) and is due to the long lifetimes of the upper levels subject to the Van Vleck effect. Only the longitudinal Zeeman effect in long wavelength allows a direct measure of the coronal field strength of about 4 G (Lin et al. 2004)

Scattering events can also cause non-zero polarization for continuum radiation. Stenflo (2005) shows that scattering at neutral hydrogen in its ground state (Lyman scattering) and to a lesser extent Thomson scattering causes a degree of linear polarization up to 0.1% in the visible spectrum.

The Kemp effect or the alignment-to-orientation mechanism is explained with similar oscillator models as the Hanle effect. This mechanism involves the production of circular polarization by anisotropic illumination (Kemp et al. 1984). If this radiation is circularly polarized it will orientate the atomic levels along its propagation direction. Also lateral radiation for instance from a sunspot penumbra towards the umbra is able to induce orientation of the atom The direction of emergent circular polarization from such orientated atoms is not governed by magnetic fields and therefore the Kemp effect influences Zeeman magnetogram measurements in lines with many level crossings for weak fields (Brown at al. 2003). The Kemp mechanism is a zero order effect that produces broad circular polarization which leads to net circular polarization in the Zeeman profile.

The Stark effect involves production of polarized spectral profiles through level splitting in the presence of strong electric fields. Contradictory to the Zeeman effect this splitting is a second order effect and appears quadratic instead of linear (Casini & Landi degl'Innocenti 1996). The electric fields in the highly conductive solar atmosphere are usually not sufficient to produce a significant effect..

3. Ba II 4554 and Hβ

This chapter gives an overview of literature describing solar observations in the Ba II 4554 line and in Hβ. These two lines are optimally transmitted by the 80 mÅ bandpass Lyot filter on which the DOT polarimeter is based (see chapter 5). Special interest will be given to polarimetric measurements in each of the lines. Also, measurements and their interpretation of the longitudinal Zeeman effect in the Barium line are presented.

3.1. Ba II 4554

3.1.1. Theory

The Ba II line at 4554 Å due to the resonance transition from $6p^2P_{3/2}$ to the ground level $6s^2S_{1/2}$ is the strongest line of the ionized Barium spectrum. Due to the low ionization potential of 5.21 eV, most Barium atoms are ionized throughout the photosphere (Tandberg-Hanssen & Smythe 1970). With an oscillator strength of 0.69 (Rutten 1978, Davidson et al. 1992), Ba II 4554 is a heavily scattering transition that forms a relatively deep (unblended) absorption line (see figure 3.1). The upper level population is more dependent on the radiation field than on collisional excitations. Therefore LTE cannot be assumed for the source function of this transition, although it is sensitive to temperature (with lower temperature resulting in a deeper line). The lower level is represented by regular Barium ions and therefore the opacity of the line is determined by the Barium abundance at the formation height.

Non-LTE radiative transfer models by Sykorski & Merkulenko (1988) and Uitenbroek & Bruls (1992) show that the core of the Ba II 4554 line is formed at about 700 km above the photosphere, near the canonical temperature minimum. The wings are formed in deeper layers of the photosphere. Eclipse measurements by Rutten (1977) show that the line wings have emission features on the extreme limb, which can be explained by assuming partial frequency redistribution (PRD) in the scattering coherency (Rutten & Milkey 1979). Coronagraphic measurements by Shilova (1966) show that Ba II 4554 emission is present in chromospheric structure (off-limb). Faint emission of Ba II 4554 is also observed in prominences (Tandberg-Hanssen 1964) and flares (Zirin 1964), although at those circumstances (>10 eV) most Barium atoms are already ionized twice to Ba III (Landman 1983).

The Ba II 4554 transition has the same quantum numbers as the very useful Ca II K and Na I D2 lines. Due to a lower abundance (almost ten orders of magnitude lower than Hydrogen, Holweger & Müller 1974), the Barium line is formed in a lower region than the Calcium H and K lines (see figure 1.1.b) and is therefore as interesting a diagnostic of the upper photosphere as the Calcium lines are of the lower chromosphere.

Figure 3.2 shows observations with the Ba II 4554 Lyot filter by Sütterlin et al. (2001) at the former 0.5 m Swedish solar Vacuum Telescope on La Palma, which were performed as a test for the future DOT Barium channel.

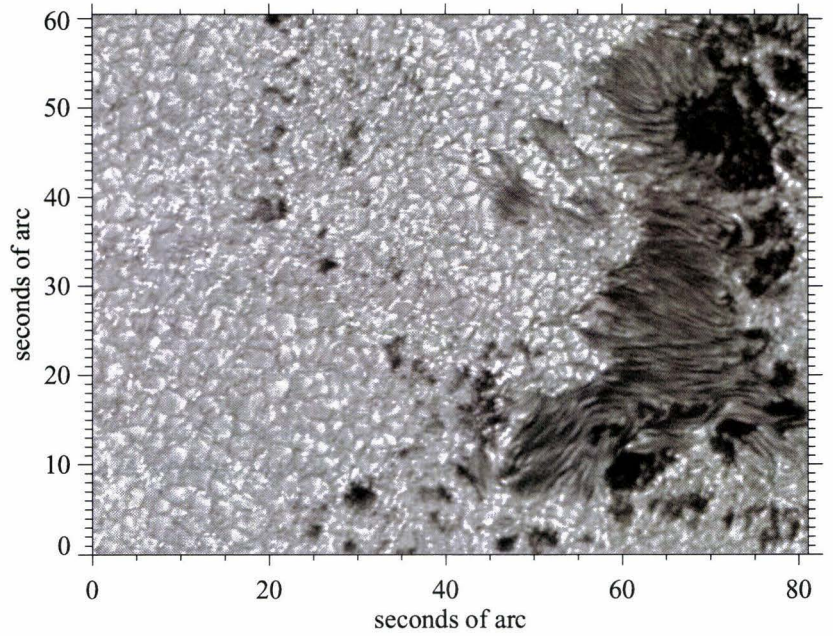**F.3.1.**
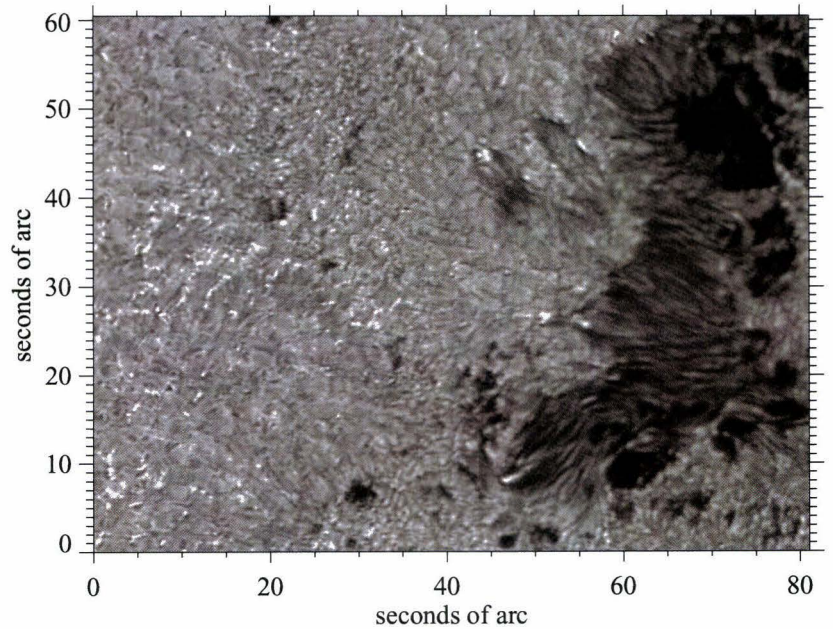The spectral profile of the Ba II 4554 line. From the quiet Sun, disk center spectral atlas by Neckel (1999).
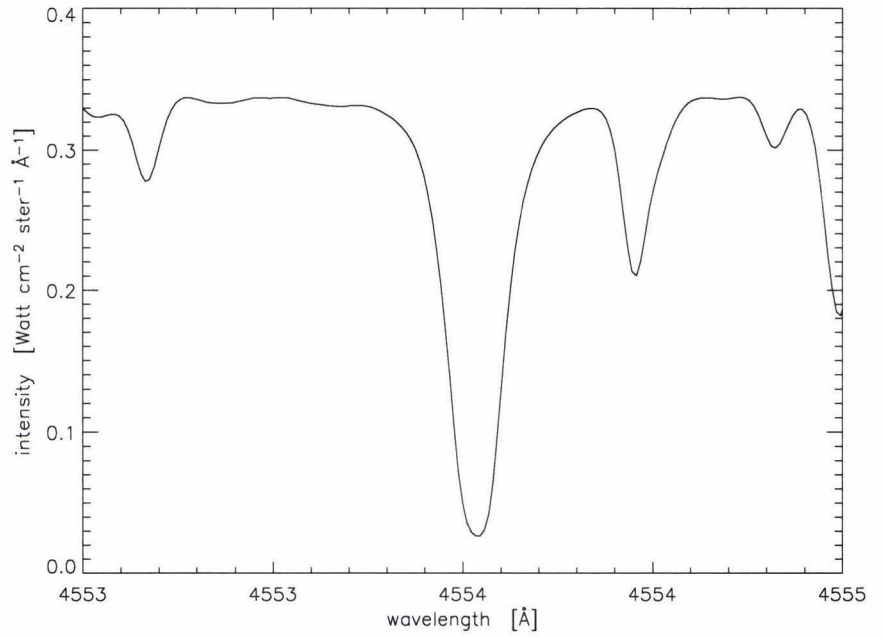
F.3.2.
Ba II 4554 observations of AR9077 on July 15th 2000 with the 80 mÅ Lyot filter at the SVST. The filter is scanned through the line at -70 mÅ (a), -35 mÅ (b), 0 mÅ (c), +35 mÅ (d), +70 mÅ (e) with respect to line center. From Sütterlin et al. (2001).
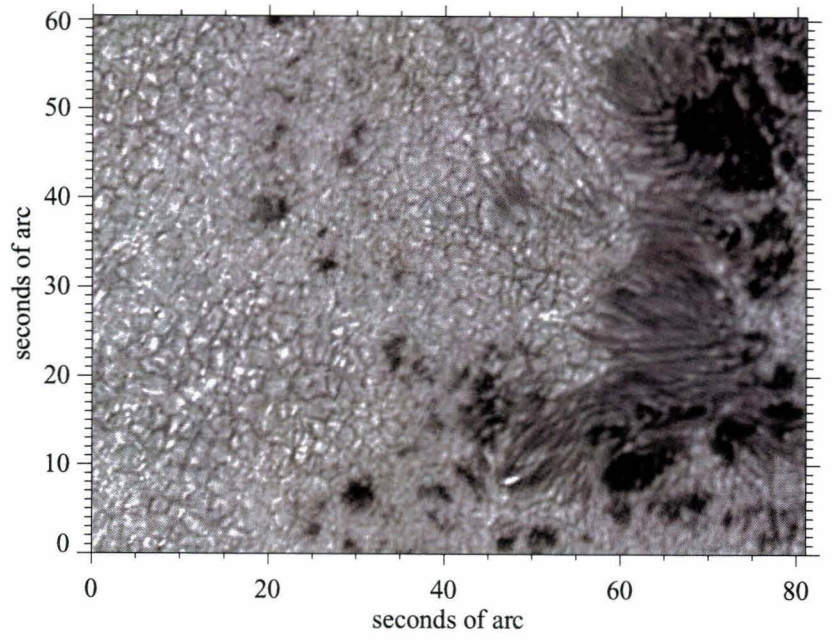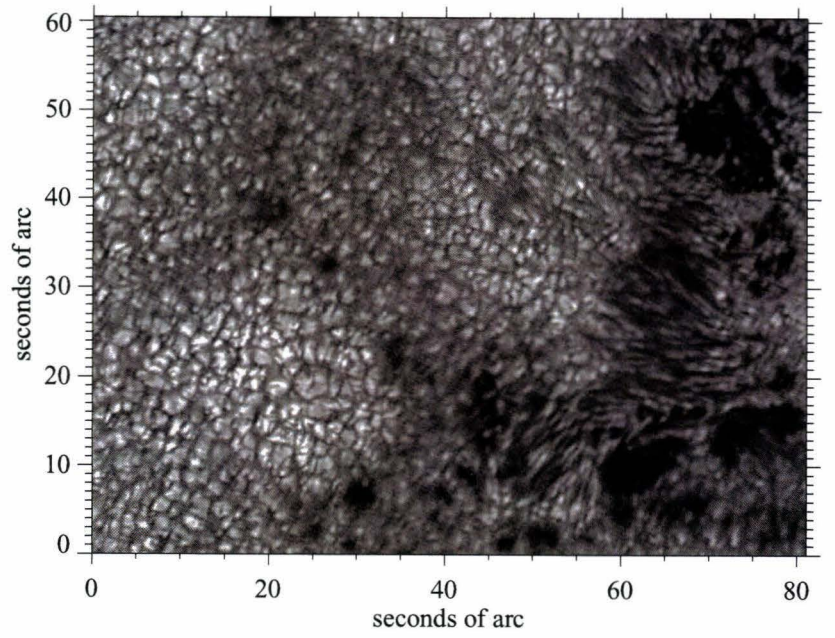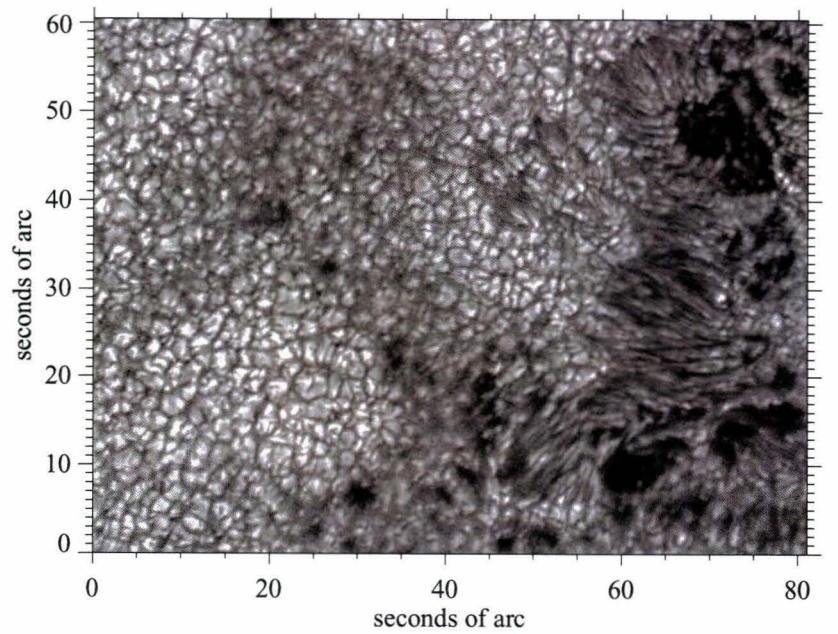
c

d

e

With these observations the Lyot filter was scanned through the line with steps of 35 mÅ. The resulting filtergrams show striking differences between the two line wings due to the large sensitivity to the granular velocity pattern (see below). The line center image has no clear signs of the granulation reversal of the lower chromosphere either due to the lower formation height or due to the large photospheric contribution of the line wings, which are partially sampled by the filter profile.

Barium atoms naturally occur in a range of nuclear isotopes (see table 3.1). About 18% of the atoms have an odd isotope number and therefore an non-zero nuclear magnetic moment with I=3/2.

T.3.1.
The occurrence of the different nuclear isotopes of Barium. From Cowley & Frey (1989).

isotope number	130	132	134	135	136	137	138
fractional abundance	0.64%	0.64%	2.7%	6.52%	7.4%	11.2%	70.9%

This means that for weak fields 18% of the line consists of hyperfine structure (HFS) components. As the splitting of the upper level with F=0,1,2,3 is a magnitude smaller than the HFS of the ground level with F=1,2 (Rutten 1978) , two groups of HFS components are present on both sides of line center (see figure 3.1).

F.3.3.
The hyperfine splitting pattern of the Ba II 4554 line. Taken from Rutten (1978).
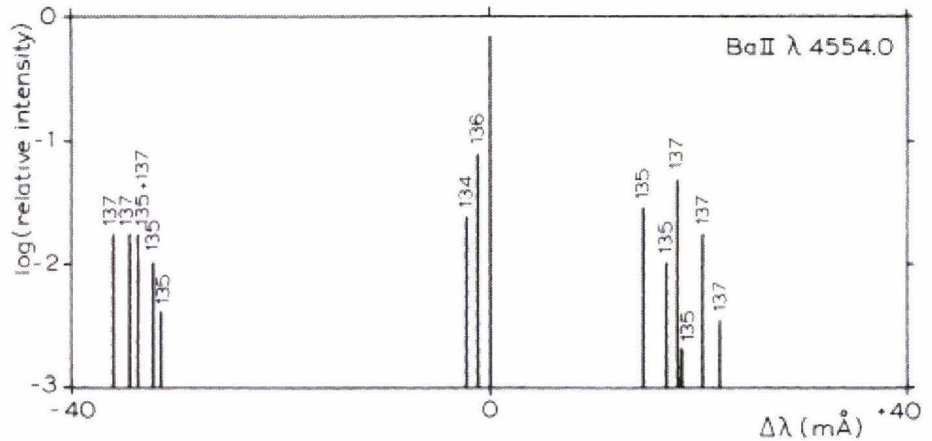
These HFS components give the spectral profile of Ba II 4554 in figure 3.1 its typical 'boxy' and slightly asymmetric look. Moreover, the line wings are very steep owing to the fact that Barium is a very heavy atom ("barius" means "heavy" in Latin). Therefore the line profile is not very sensitive to thermal Doppler broadening.
These properties make the Barium line particularly suitable for Doppler measurements of large scale velocity fields, especially for a telescope that is able to resolve structures down to the typical length scales of the plasma motions. The supergranulation velocity pattern is indeed best observed in Ba II 4554 (Noyes 1967) and also the solar 5-minute oscillation (p-modes) creates observable line shifts (Polyakov 1979), and can therefore be utilized for helioseismology (Uitenbroek & Bruls 1992).

The resulting Dopplergram (after filtering 5-minute oscillations) of the observations in figure 3.2 is presented in figure 3.4. It shows the rich structure of the velocity fields in the photosphere. Clearly visible are the rising granules, the intergranular downdrafts and flows along the penumbral pattern. Many small-scale downdrafts are most probably associated with the immediate surroundings of magnetic flux tubes that appear as bright points in the G band.
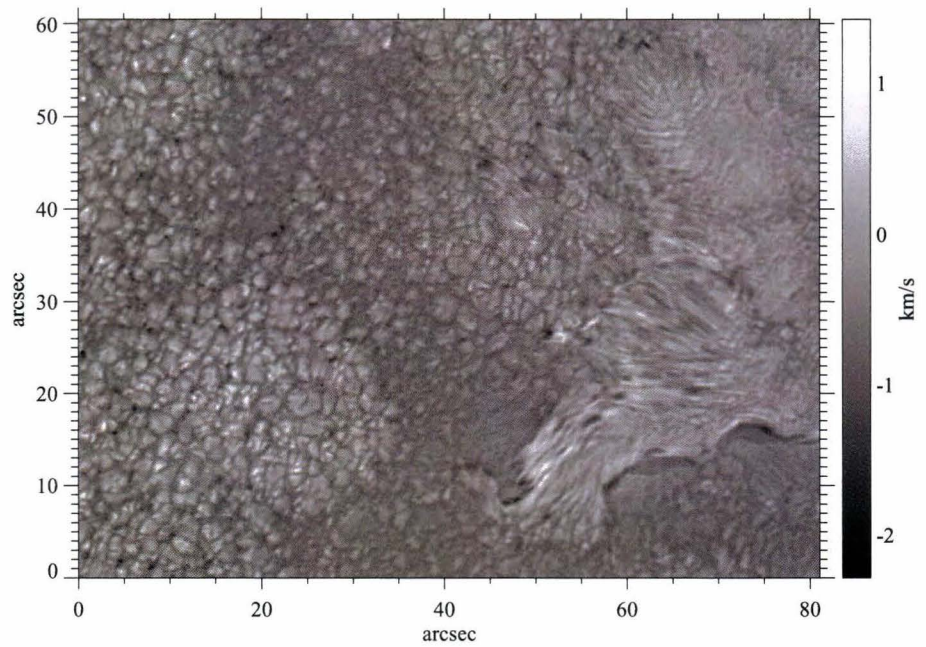
It was found that Dopplergrams in Ba II 4554 can also be accurately acquired by taking images in each line wing, at the wavelength of maximal steepness. There the signal is very sensitive to Doppler shifts. The Doppler velocities can then be calculated with:

E.3.1.
$$V = C \frac{I_{blue} - I_{red}}{I_{blue} + I_{red}},$$

with

E.3.2.
$$C \approx \frac{1}{2} \frac{c}{\lambda} \frac{d\lambda}{dI_{red,blue}}$$

in first order for the symmetric wings.

Positive V here indicates redshifts. The proposed method is independent on the spectral intensity.

Ba II 4554 has the strongest signal in the second solar spectrum (see the atlases by Gandorfer; 2000, 2002) which is presented in figure 3.5. Linearly polarized signals in this line were observed by Wiehr (1975, 1978, 1981), Stenflo et al. (1997), Stenflo & Keller (1997) and Bommier & Molodij (2002) and show variations with the solar cycle.

It has a peculiar triplet-like structure due to the presence of the HFS components in the wings. These components have a high degree of coherence in their scattering due to the many level crossings at weak fields. Stenflo & Keller (1997) and Stenflo (1997) successfully reproduced the shape of the polarized Ba II 4554 spectrum with model atoms according to the isotopic distribution of table 3.1. The central peak is due to the 82% of non-HFS components which are obviously polarizable to a lesser extent. Stenflo (1997) explains the visibility of the HFS components in the Stokes Q profile (in contradiction to the regular intensity profile) by the fact that polarization profiles are not subject to saturation broadening, which smears out the HFS components in the Stokes I profile.

Up to now no models were adopted to explain the signal strength of the Ba II 4554 line in the second solar spectrum. Several contributions can lead to high signal strength of the scattering polarization. First of all, Ba II 4554 is largely dominated by scattering and combined with the degeneracy of the upper level therefore prone to scattering polarization. Measurements of the center-to-limb behavior of the linear polarization by Stenflo et al. (1997) show that the variation in Ba II 4554 is only slightly steeper than that expected of a purely scattering atmosphere.

The core of the line is formed at a relatively high layer in the solar atmosphere. Therefore the degree of anisotropy of the radiation is higher than for other photospheric lines. Also the cores of the HFS components are formed higher layers than the rest of the line wing, which constitutes another explanation of the fact that the HFS components are separately visible in the Stokes Q profile.
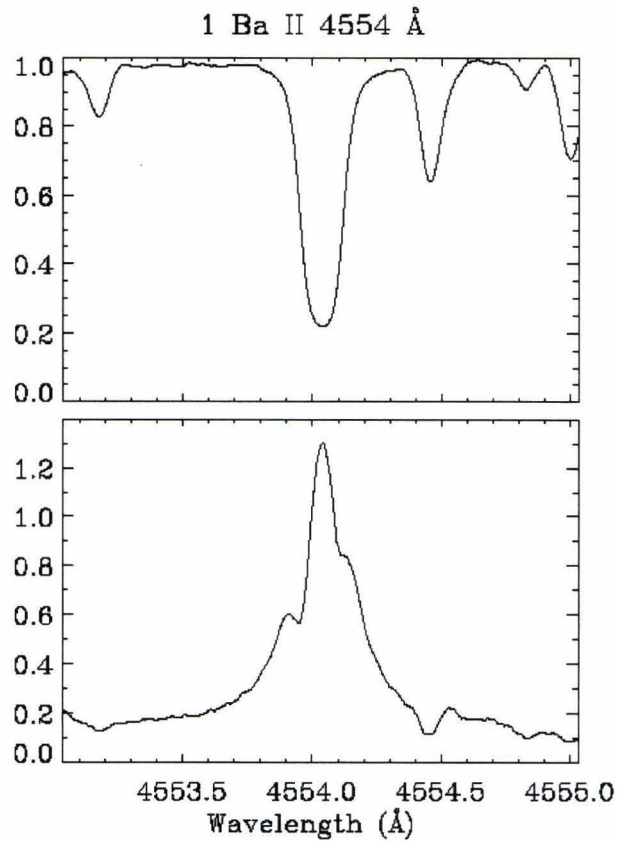
1 Ba II 4554 Å

For LTE-lines the average formation height is increased when the atmosphere is observed at an angle, which causes limb darkening in a negative temperature gradient. This is not the case for the heavily scattering Ba II 4554 line since the angle-averaged mean intensity which controls the line source function does not vary much with height in the layers around optical depth unity at line center. The thermal contribution to the observed line intensity increases towards the wings. (Uitenbroek & Bruls 1992).

Furthermore, also the high coherency in scattering (PRD) of the line inhibits strong spectral smearing of the linearly polarized spectrum, which lead to smaller and stronger signatures. The coherency width is additionally narrowed by the small extent of the Doppler redistribution. Finally, the short lifetime of the upper level of the transition prevents strong Hanle depolarization due to the weak turbulent fields.

These properties make Ba II 4554 an excellent candidate to perform Hanle measurements with. It is highly probable that conform observations by Trujillo Bueno et al. (2002a) in Na D2, the HFS components are depolarized by increasing fields to a lesser extent due to their high coherences than the central non-HFS components. The line may prove to be an excellent diagnostic of the weak turbulent magnetic fields, as the observation spanning almost two solar cycles show that the signal strength of Ba II 4554 in the second solar spectrum varies with the magnetic activity. The presence of the line in the lower chromosphere when observed off the limb and in prominences (although faint) may enable Hanle measurements of chromospheric magnetic structures. And since the lower level HFS components can harbor atomic alignment, maybe also selective absorption can be observed in strongly absorbing filaments.

These hypotheses of course have to be confirmed by measurements and models. Trujillo Bueno (private communication) will in the near future extend his existing models of the Na D2 line to the more difficult case of the level population and polarizability of Ba II 4554. The DOT Ba II 4554 polarimeter (see chapter 5) will explore the possibilities of Hanle measurements in each of the three spectral components which are observed in the second solar spectrum.

The most powerful feature of the Ba II 4554 polarimeter will be the creation of magnetograms at equal resolution and cadence as the rest of the DOT tomographic system. It is therefore critical to explore the Zeeman responses of this line to magnetic fields.

3.1.2. Zeeman observations

Spectropolarimetric measurements of the Ba II 4554 line were carried out at IRSOL in Locarno (Switzerland) by positioning the entrance slit of the spectrograph across sunspots at different heliocentric angles in the direction parallel to the limb. The seeing conditions were less than moderate (>2"). The polarization modulation was performed by the accurate ZIMPOL II polarimeter (see chapter 4). A Dove prism was used to compensate for image rotation due to the non-equatorial tracking of the 45 cm Gregory-Coudé telescope. The details of the four useful datasets are to be found in table 3.2.

dataset #	AR #	date observed	heliocentric angle	spot type
1	10606	14/05/2004	10.8°	unipolar
2	10713	24/12/2004	19.9°	unipolar
3	10715	30/12/2004	58.2°	bipolar
4	10613	15/05/2004	70.9°	unipolar

For each dataset observations were made with five minute's exposures of (I,Q,V) and five minutes of (I,U,V), resulting in a total integration time of ten minutes for I and V. After a spectral observation of Ba II 4554, the same observation was repeated for a spectral region containing the two Fe lines at 6301.5 Å and 6302.5 Å. Especially the latter line is a popular line for magnetograms (e.g. Berger & Lites 2002, Domínguez Cerdeña et al. 2003) with a formation height of about 200 km and a Landé factor of 2.5. This region is also popular due to the presence of two telluric lines that allow a careful wavelength calibration. The spectral data of both lines were aligned with atlas profiles from Neckel (1999) to obtain the correct wavelength values.

The spatial direction of the observations is sampled with about 0.7"/pixel. The spectral resolution is about 6.0 mÅ around 4554 Å and 7.0 mÅ around 6302 Å. The spectral data are smoothed with a 2 pixel wavelet, to reduce the noise level even further. All data are corrected for the polarization modulation, dark subtracted and flat-fielded. Also intensity gradients and image curvature are corrected for.

The telescope inherently has significant cross-talk components in its instrumental Mueller matrix for observations on dates far from the equinoxes (Stenflo et al. 1997). However, this cross-talk is approximately constant during the day and can easily be corrected for with the following recipe. Firstly, the continuum polarization on the Sun is assumed to be sufficiently small compared to the Zeeman measurements. Therefore, the continuum polarization which is largely caused by instrumental polarization is determined from the measurements and subtracted. Next, the Stokes spectra due to the Zeeman effect are analyzed for their (anti-) symmetry. it is assumed that any antisymmetric contribution to the Stokes Q and U profiles is due to cross-talk from Stokes V and vice versa. Accordingly the original signals in Q, U and V are reconstructed, using the orthogonal properties of the Stokes vector.

Stray light from the sky or in the telescope imposes an extra spectrally flat contribution on the observed unpolarized spectra. Unfortunately the observed spectra of active regions did not allow an accurate comparison with the quiet Sun spectral atlas to calculate the signal level of scattered light. Earlier observations by Stenflo et al. (1997) and Bianda et al. (2005) with the set-up showed a stray light contribution of about 1.5% of the continuum level. Therefore the polarization degree of X/I will only be slightly underestimated.

The line of sight magnetic field strength on each spatial position was determined for the Fe 6302 data with the weak field formula 2.10.c. and with the center of gravity method using equations 2.11 and 2.12 without the assumption of a purely symmetric I profile due to the blended O_2 line in the far red wing. The absolute field strength was determined from the splitting according to equation 2.9.b of the unpolarized line profile. The line broadness is a good measure for the Zeeman splitting if it is larger than the line's Doppler broadening. In these cases an absolute field strength larger than 1.2 kG are accurately retrieved within 2%. For smaller splittings a linear interpolation is adopted for the observed line broadness, which retrieves the absolute field strengths down to half that value within 5%.

These inversions of the absolute and longitudinal magnetic field strengths are all based on successful model-independent techniques. However, the weak field approximation is no longer valid for fields stronger than 3.5 kG/g_L and therefore the COG method is adopted for absolute fields stronger than 1 kG. The weak field formula is less sensitive to noise for lower values of V/I and therefore it is used for absolute fields smaller than 1 kG. The typical results for the absolute field strengths

B_{abs} and the line of sight field strengths B_{LOS} across a unipolar sunspot is presented in figure 3.6. An empirical factor >1 had to be applied to the longitudinal field strength from the COG method, due to the stray light contribution and the presence of the blended telluric line in the wing and the unpolarized π component in the line center, that both lead to an incorrect retrieval of the center of gravity. The factor was chosen such that the longitudinal field strength in the center of the spot is equal to the absolute field strength, assuming circular symmetry. For sunspots observed at an angle the profiles of the corrected $B_{LOS}/\cos\theta$ will also coincide with B_{abs} at the center of the spot only if the spectrograph slit is aligned perpendicularly to the local heliocentric direction.

F.3.6.

The typical signature of the absolute field strength (solid line) and the absolute value of the longitudinal field strength (dashed line) across sunspot #2 of table 3.2. It clearly illustrates the presence of inclined fields in the sunspot penumbra. The dotted lines represent the inaccurate values retrieved by the COG method for $B_{abs} < 1$ kG and by the weak field approximation for $B_{abs} > 1$ kG. The dash-dotted line represents $B_{LOS}/\cos\theta$ and shows that the radial field strength in the center of the sunspot is equal to the absolute field strength.
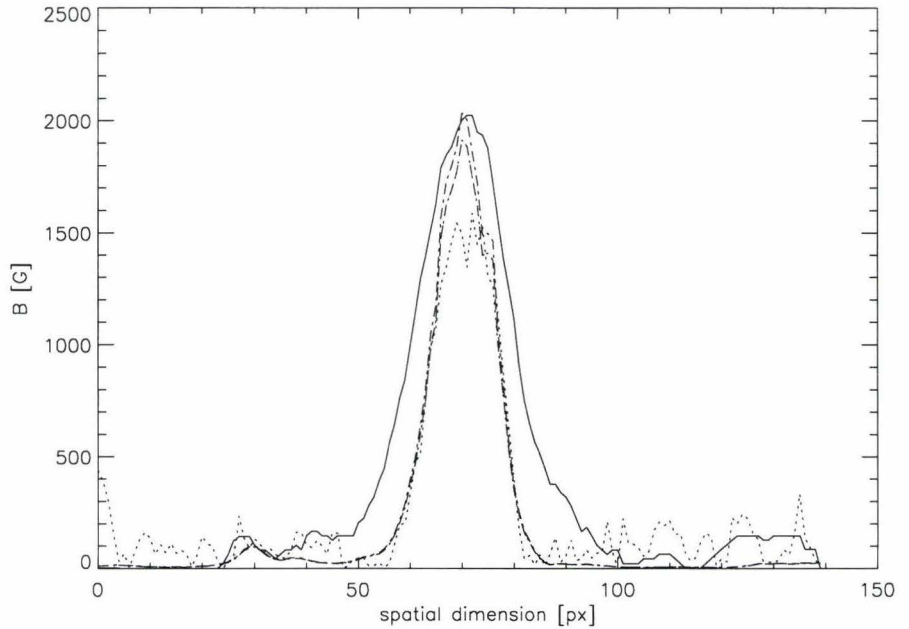
By means of cross-convolution the retrieved magnetic signatures of the sunspot are spatially aligned with the data at 4554 Å. The resulting V/I behavior of Ba II 4554 as a function of B_{LOS} as observed for spot #1 is presented in figure 3.7.

F.3.7.

The spectral response in Stokes V of Ba II 4554 to a line of sight field as observed for spot #1.
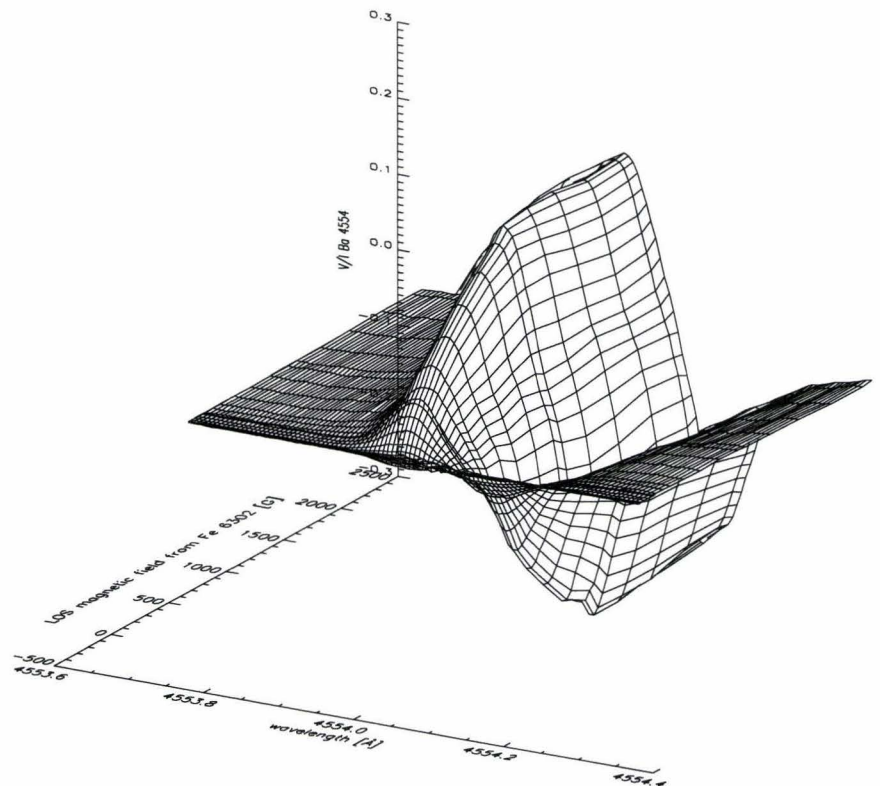
The typical antisymmetric signal of the longitudinal Zeeman effect is obvious. At B_{LOS}=1 kG there is a very sudden and sharp saturation of V/I at about 23%. This effect is more clearly illustrated by the plot of the absolute value of the two extrema versus the line of sight field strength for all four spots in figure 3.8.
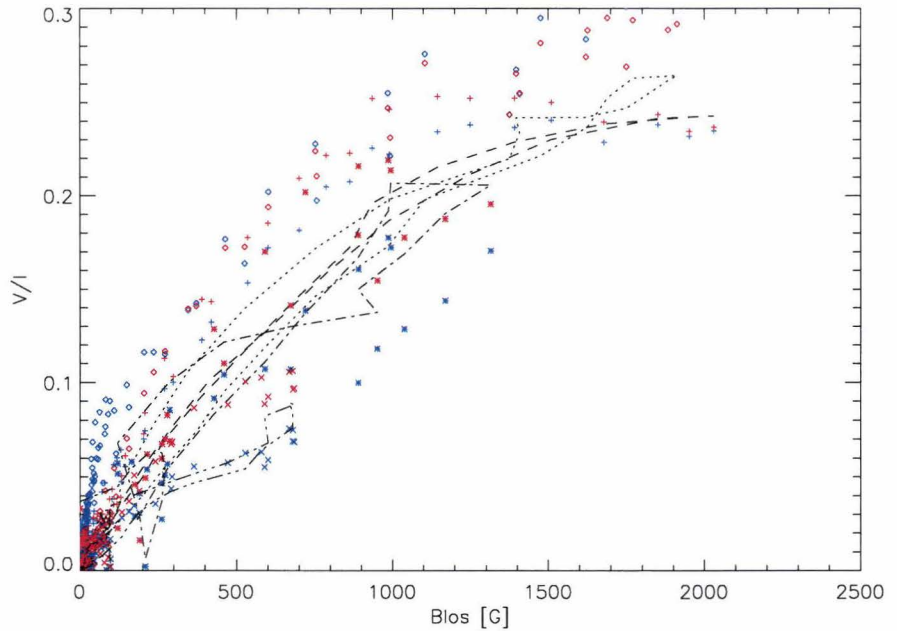
F.3.8.

Plot of the absolute signal strength of V/I for the blue (+72 mÅ) and the red wing (+60 mÅ) of all four datasets. The symbols + represent measurements from dataset #1, ◊ from #2, * from #3 and X from #4. The lines represent the maximal V/I signals of Fe 6302 for each dataset: dashed #1, dotted #2, dash-dotted #3, dash-dot-dotted #4.

It is clear that the sharp saturation effect is only clearly present in datasets 1 and 4, but sets in for different longitudinal field strengths and therefore at lower values of V/I. A saturation effect is also present in datasets 2 and 3, albeit much less pronounced. The scatter is also much larger in these two datasets. It is also apparent that the response of V/I to B_{LOS} is steeper for Ba II 4554 than for Fe 6302 which is represented by the lines. The measurements of datasets 1, 3 and 4 indicate that the signal level in the red wing (indicated by the red color within the individual datasets) is even higher than the extrema of V/I in the blue wing, colored blue. The location of the maximal values of V/I in the line wings are found at 72 m Å in the red wing and at 60 mÅ in the blue wing, which also points to significantly asymmetric signals.

The scatter in these measurements is mainly caused by inaccurate alignment or inaccurate pointing of the telescope. The moderate seeing conditions do not influence the alignment of the datasets of both lines, as long as the average seeing is constant for the duration of both observations. Within the about 30 minutes per total dataset is not to be expected that the active region considerably evolves at this low spatial resolution.

It is tacitly assumed that the magnetic data inferred from Fe 6302 is also applicable to Ba II 4554, but there is a difference in formation height between the two lines, although the wings of the Barium line –where V/I has its extrema- are formed lower in the photosphere than the core. For a sunspot is relatively safe to assume that in its center the magnetic flux stays constant for this range of altitudes.

The linearly polarized signals due to the transverse Zeeman are not analyzed due to their more complex nature. Their polarization degrees of ~1% are too low anyway to be accurately determined with DOT Ba II 4554 polarimeter (see section 5.5).

3.1.3. Zeeman modeling

In order to explain the observed behavior of figure 3.8, it is logical to model the Zeeman effect of the Ba II 4554 line. Naïve application of the weak field approximation for Stokes V conform equation 2.10.c, using the effective Landé factor of 1.167 (Sütterlin et al. 2001) and the spectral profiles $I(\lambda)$ and $dI(\lambda)/d\lambda$ as a function of B_{LOS} from dataset #1, results in the dashed curve in figure 3.9.

F.3.9.
Plot of the same datasets as in figure 3.8. The lines with the same styles as in figure 3.8 represent the V/I signal level based on the magnetograph formula, using unpolarized line profiles from the same datasets. The horizontal lines represent saturation levels at heliocentric angle zero and the respective heliocentric angles of the four datasets.

The solid blue and red lines represent the signal levels as modeled with the DIAGONAL code with a field parallel to the line of sight including 18% HFS.
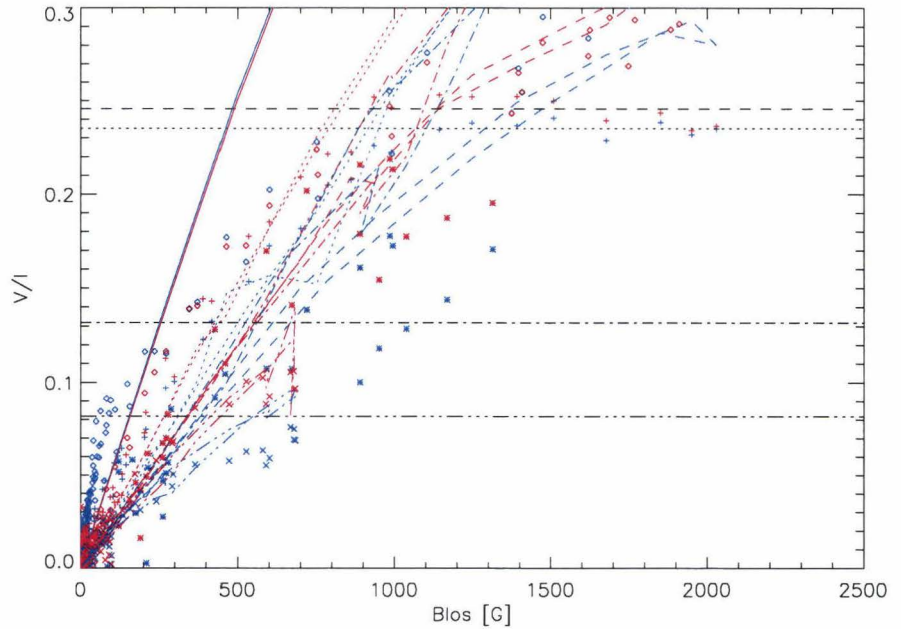
It is obvious that the regular magnetogram formula is not able to reproduce the observed data, neither in steepness of the response nor in the saturation. However, the steepness of the response is higher than expected for other Zeeman sensitive lines at these wavelengths due to the steepness of the line wings of the unpolarized spectrum. A slight decline in the signal response is observed at the same longitudinal field as the saturation point of dataset #1 due to the reduction of the steepness of the line wings for the corresponding field strength.

The steeper response than what is expected from the regular magnetogram formula and the possible presence of asymmetries in the Stokes V profiles point to an influence of the HFS components. At weak fields the HFS components can be considered to be two blended lines in the wings with their individual antisymmetric Zeeman signals (see figure 3.3). It is likely that these signals both happen to enhance the Zeeman signal of the total line. To investigate the effects of the HFS, a more intricate model is adopted, which is based on the DIAGONAL full Stokes radiative transfer code by López Ariste & Semel (1999). This code uses analytic solutions to the radiative transfer equation and is also upgraded to solve for the HFS Hamiltonian in the incomplete Back-Goudsmit regime (López Ariste et al. 2002).

DIAGONAL is not able to include non-LTE effects of the radiative transfer, which are required for an accurate description of the Ba II 4554 transition. However, Stokes inversion modeling by Westendorp Plaza et al. (1998) shows that in general not all physical parameters of a spectropolarimetric dataset can be retrieved with sufficient accuracy. Therefore the Stokes I profile of the zero field atlas by Neckel (1999) is modeled by transfer through a single layer Milne-Eddington atmosphere with physically incorrect parameters for the Doppler broadening, damping, absorption and emission gradient under the premise that then the magnetic signatures of Stokes V will be sufficiently accurate to give general information about the magnetic response of Ba II 4554. The calculation is performed for an atom without HFS and for an atom with HFS structure conform the data presented by Rutten (1978). The resulting Stokes profiles of both calculations are linearly superposed conform the isotopic distribution of table 3.1. Figure 3.10 shows the results of the line fitting process of the Ba II 4554 profile from the Neckel atlas at zero field.

The line profile of the Ba II 4554 line from the Neckel atlas (here represented with ◊ symbols) as modeled with physically incorrect parameters of the DIAGONAL code. The dotted line is the modeled line profile for zero field. The dashed line is the profile at $B_{abs} = 1.5$ kG; the dash-dotted line is the profile at 3 kG.
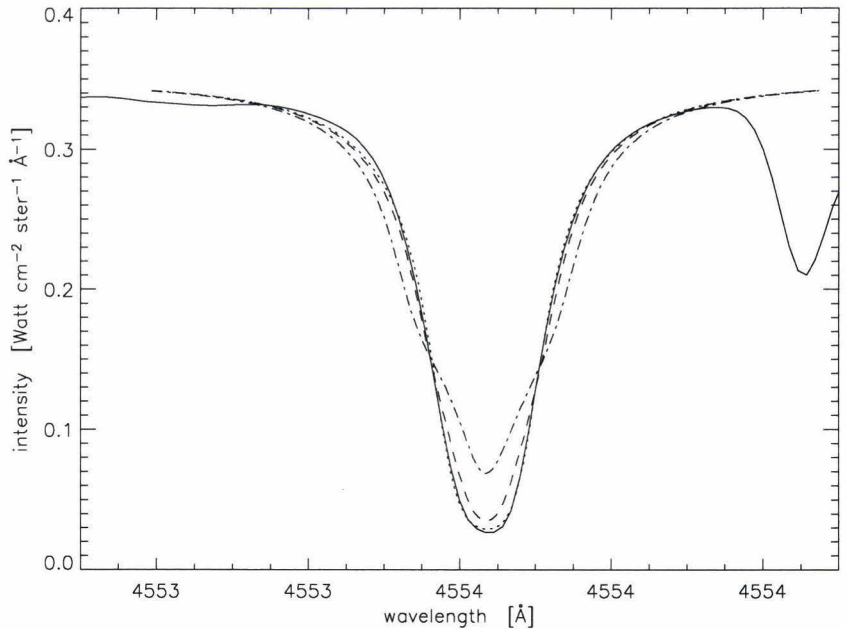
The results for the maximum absolute signal strengths in the line wings for longitudinal fields are plotted in figure 3.9 as blue and red solid lines. It appears that only the steep response for weak fields is reproduced by the model. For absolute fields of about 1.5 G, the HFS components are destroyed and their magnetic signatures are 'redistributed' over the full line profile, making it a regular Zeeman sensitive line. Despite the presence of the asymmetric HFS components no significant asymmetry is produced, due to compensation by the asymmetric line wings. Nonetheless, datasets 1, 3 and 4 point to an even steeper response in the red wing. This asymmetry may be explained by the asymmetrical HFS components in the line wings, but this is not decisively modeled by the DIAGONAL code, due to physically incorrect values for the model parameters. For instance the value for the Doppler broadening is far too high and wipes out much of the asymmetric HFS signals. Therefore a more realistic non-LTE model should be applied to determine the influence of the HFS and the reality of asymmetries in V/I. Such asymmetries would enable differential measurements between the two line wings to infer field strengths in the incomplete Goudsmit-Back regime due to the asymmetry of the response, although the signal to noise ratio of the difference of already differential measurements will be poor. Khomenko (private communication) is planning to model the Stokes profiles of Ba II 4554 using the non-LTE SIR code by Ruiz Cobo (1998), including HFS and PRD effects in a sunspot model atmosphere.

A bend of the modeled Zeeman response due to the reduction of $(dI(\lambda)/d\lambda)/I(\lambda) = d(\ln I)/d\lambda$ is also present here (see the dashed and dash-dotted profiles of figure 3.10) but it is by far not strong enough to explain the saturation of the observed signals. It is therefore instructive to look at the saturation of the observed V/I profiles of the Fe 6302 line, which is mainly caused by Zeeman saturation. Assuming a linear dependence of the Doppler broadening on wavelength and an inverse dependence on the square root of the atomic weight and using equation 2.9.b for the Zeeman splitting, the field strength for which the Zeeman splitting of Ba II 4554 becomes larger than the Doppler broadening is about 1.9 times the value for Fe 6302. The saturation of the Ba II 4554 signals in figure 3.8 sets in for fields of the same order as for the Zeeman saturation in Fe 6302 therefore it is concluded that the sharp saturation in the V/I profiles of Ba II 4554 is partially caused by Zeeman saturation.

For absolute field strengths larger than 1 kG all the V/I profiles of datasets 1 and 4 are fully saturated. Less strong saturation effects are also present in the other two datasets. This saturation effect of the V/I profiles is also not reproduced by the model due to non-physical parameters for the Doppler broadening, causing a severe underestimation of the Zeeman saturation and the HFS effects. The fact that only datasets 1 and 4 (which were obtained on the same date) show such sharp saturations might point to an instrumental origin. A non-negligible contribution of stray light can cause a significant decrease in the V/I signal in the dark umbral region, especially for the deep Barium line. Such possible levels of stray light disqualify the application of the DIAGONAL model even further, as the model assumes negligible stray light contributions. In this case the less sharp saturation of dataset 2 is a more realistic

representation of the V/I saturation in Ba II 4554, which can therefore more accurately described by the Zeeman saturation in comparison with the saturation of Fe 6302. Another possible contributor to the saturation is the destruction of the HFS components, resulting in less enhancement of the V/I signal in the line wings. Also here, a more accurate model has to be applied to test this hypothesis. Both Zeeman saturation and the destruction of the HFS are governed by the absolute field strength and therefore it is useful to test if the saturation level of V/I is a exclusive function of $B_{LOS}/B_{abs}=\cos\theta$. Vertical dashed lines are plot in figure 3.9 for the four datasets according to this formula with a V/I saturation level of 25% at $\theta=0$. The saturated data from dataset 1 and 4 and to a lesser degree dataset 3 are in agreement with the respective horizontal lines.

Saturations can also be caused by inherent saturation of the strong Ba II 4554 line. Furthermore, differences in formation between Ba II 4554 and Fe 6302 can have an influence on the observed saturation effects if the field has a large divergence between the formation height of Fe 6302 and Ba II 4554.

However, it is clear that the strong saturation for absolute fields larger than 1 kG effectively inhibits the retrieval of the longitudinal field strength. If in this regime the destruction of the HFS strongly enhances the Zeeman saturation, the sharp saturated signal strength is largely dependent on the angle between the magnetic vector and the line of sight. This effect might prove an interesting diagnostic of the field inclinations in sunspot penumbrae.

In conclusion, the measurements of the Zeeman response of the Ba II 4554 line show some striking results. Firstly the Zeeman response to weak fields of Ba II 4554 is even steeper than that of the regularly used magnetogram-line Fe 6302. This is a very important property since the Barium line is further into the blue and therefore its magnetograms have a smaller diffraction limit than Fe 6302 magnetograms created with the same telescope. Magnetograph measurements in Ba II 4554 will therefore be able to observe magnetic structures with smaller length scales and lower longitudinal field strengths.

The applied weak field model and the DIAGONAL model are not capable to give a definite explanation of the observed steep response, the saturation and the possible asymmetries. A more accurate model is required to obtain valid inversion curves for the longitudinal field strength in both line wings of the V/I profile.

Since the line profiles of Ba II 4554 up to the saturation are not very sensitive to turbulent Doppler broadening and are mainly governed by the HFS components and the Zeeman splitting itself, the Zeeman effect of line is less influenced by different circumstances in the solar atmosphere and is therefore a more generic tool for measuring magnetic fields than Fe 6302. Due to the range of formation heights along the wings, the Zeeman profiles are considerably sensitive to vertical magnetic gradients and velocity gradients.

The reduction of $d(\ln I)/d\lambda$ with increasing field strength and also the possible asymmetry will also have an influence on the determination of the Doppler velocities with equations 3.1 and 3.2, although in general magnetic structures inherently have only small velocities (see e.g. Berger et al. 2004). The dashed line in figure 3.9 shows that fields up to about 1 kG have no significant influence on the value of $d(\ln I)/d\lambda$ at the position of maximal steepness in the line wings and therefore not on the Dopplergrams. This is also reproduced in figure 3.10, despite the incorrect representation of the Zeeman saturation.

The most mutual influences of the magnetograms and the Dopplergrams will be found in regions of the small intergranular flux tubes. Strong downflows of about 2 km/s are observed in the immediate surroundings of the flux tube (e.g. Sütterlin et al. 2001), which causes both strong Zeeman signals and Doppler shifts within one resolution element if the tube is unresolved or if the resolution element samples only the wall of the tube.

3.2. Hβ

Hβ is the second line in the Hydrogen Balmer spectrum (n=4→n=2) and therefore it has similar diagnostic capabilities as Hα. Due to the very high excitation energy (10 eV) of the lower level, both the Balmer-line opacities and the Balmer-line source functions are formed far out of LTE conditions. In addition, many of the chromospheric structures observed on the Balmer lines are optically thin and in some cases effectively thin while optically thick (meaning transparent for photons in multi-step scattering sequences). The Hβ line has 6 times smaller opacity than Hα, so that some structures that are thick in Hα will be thin in Hβ. In 'one-dimensional' standard models of the solar atmosphere Hβ has a correspondingly lower formation. Qu & Xu (2002) show that the contribution function of the 80 mÅ broad core of Hβ in a quiet Sun model atmosphere has significant quantities at heights of 700-2000 km above the photosphere, while Hα is formed mostly above 1200 km. Also the region around 300 km altitude has a considerable contribution to the core of Hβ. The extended Stark broadened wings are photospheric and blended with one strong Fe line and several weaker lines (see figure 3.11).
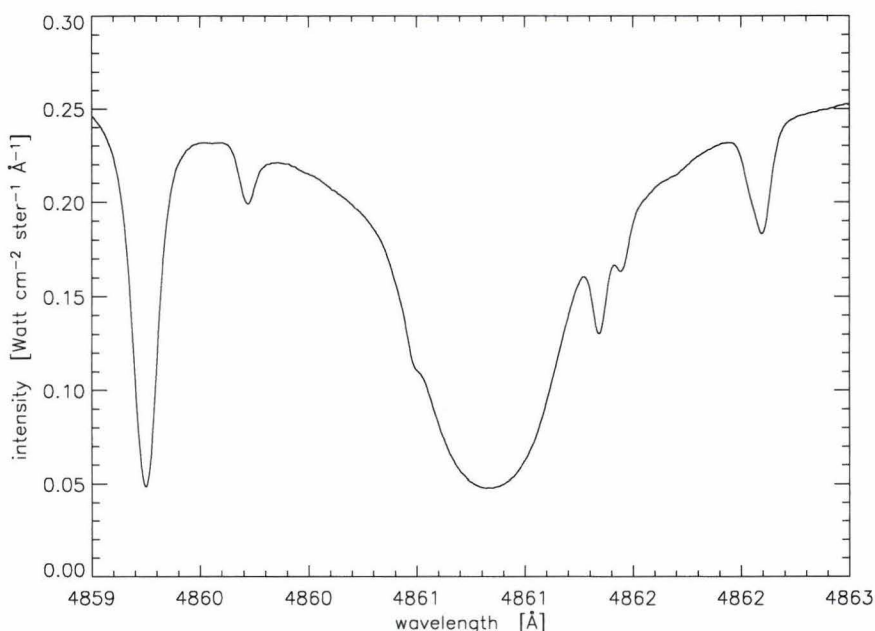
For solar observations the unblended and stronger Hα line is routinely used for studies of the upper chromosphere (e.g. Tziotziou et al. 2003). Combined spectral observations in Hα and Hβ are used to study emission profile differences in prominences (Landman & Mongillo 1979, Stellmacher & Wiehr 1994, 2000, 2005), filaments (Schmieder 1992) and flares (Zirin et al. 1982) to retrieve information about the plasma parameters and the optical thickness.

Hβ is a Hanle sensitive line which depolarization is used for the determination of prominence field strength and topology (Nikolsky et al. 1982, Bommier et al. 1986a, Landi degl'Innocenti et al. 1987, Wiehr & Bianda 2003) and the electron density (Bommier et al. 1986b). The degree of linear polarization is usually less than 1%. The line is also prone to the Kemp mechanism for circular polarization (Wiehr & Bianda 2003). Similar diagnostics exist for filaments (Bommier et al 1989).
Also Hanle measurements of spicules like in Trujillo Bueno et al. (2005), would yield a significant signal in the Balmer lines.
Trujillo Bueno (2003b) hypothesizes that differential absorption will induce a significant amount of linear polarization in Hα for penumbral structures as in figure 1.1.c.

As discussed in section 2.2.3 high energy protons beams can induce a sizable degree of linear polarization of Hα and Hβ in flares and Ellerman bombs, although observations by Bianda et al. (2005) indicate that beam impact polarization may be non-existent due to the reduction of the beam anisotropy at the formation level of Hα and even more so for Hβ. Nevertheless Vogt et al. (2002) and Hénoux & Karlicky 2003 simultaneously observed orthogonal and parallel directions of linear polarization respectively for Hα and Hβ with a polarization-free telescope, indicating a physical and not an instrumental origin for the emergent polarization of the flare.

Hβ is also sensitive to the Zeeman effect. Stenflo et al. (1984) show that the Stokes V signature of Hβ is proportional to the derivative of the unpolarized line profile. Calculations by Casini & Landi degl'Innocenti (1994) show that for all the Balmer lines a Landé factor of 1 has to be adopted. These properties nominate Hβ as a line for chromospheric magnetograms. Such magnetograms are routinely created at the Huairou observing station (e.g. Zhang 1993, Wang et al.2003) and are significantly different from regular photospheric magnetograms. Hβ magnetogram extrapolations by Zhang & Wang (2000) are comparable with coronal UV images.

The use of the weak field magnetograph formula for Hβ (Liu et al. 1996, Zhang & Zhang 2000) and Hα (Socas-Navarro & Uitenbroek 2004) indicate that the field strength at those formation heights is about 3, 5.4 and 2.5 times weaker respectively than the photospheric field strength due to the divergence of the field with increasing height.

Balasubramaniam et al. (2004) show that in the formation of the Stokes V signal in the wings of Hα there is a large contribution from photospheric magnetic fields (see also Qu & Xu 2002). With Hβ also the blended Fe line in the red wing will have a significant influence on the magnetogram signal. Furthermore, emission features will lead to an inversal of the Stokes V signature (Sánchez Almeida 1997) and also the Kemp effect will affect this signature. All these properties indicate that a lot of caution is recommended when interpreting 'chromospheric' magnetograms in Hβ.

4. Instrumentation for polarimetry

This chapter gives an overview of design options for a polarimeter. An extensive review of the technical issues concerning polarimetry is given by Keller (2002). This text mainly focuses on the background of the DOT imaging polarimeter design (see chapter 5).

To be able to accurately quantify all the effects that were described in chapter 2 on the Sun, an ideal polarimeter would operate at a two-dimensional spatial resolution of ~0.1", temporal cadence of ~10 s, spectral resolution of ~10^5 and have a polarimetric sensitivity and accuracy of ~10^{-5}. In reality compromises have to be made between these requirements to suit the needs of only a few observational capabilities.

In general a polarimeter at a telescope consists of a polarization modulator, a spectrometer and a detector. The choice of the spectral dispersive element constitutes two major categories of polarimeters. The first is based on a spectrograph, which entrance slit can be scanned across the solar scene. The second option is the use of a tunable filter, which is spectrally scanned through the line. Hybrid solutions with a different trade-off between spatial, temporal and spectral resolution are obtained for instance with a Fourier transform spectrograph, an MSDP (multi-channel subtractive double pass through a spectrograph; e.g. Mein 2002), a two-dimensional fiber feed to a spectrograph (e.g. Rutten 1999, Lin et al. 2004) or ideally with a 'three-dimensional' detector with spectrally sensitive pixels as proposed by Keller et al. (1995). For the remainder of this chapter only the case of imaging polarimetry with the use of a tunable filter will be considered.

Modulation of linear polarization has to be performed conform the definition of the Stokes vector in figure 2.1. This modulation can be obtained with only linear polarizers. Several physical effects can be applied to construct useful linear polarizers: Selective absorption or dichroism of one component the electric vector of radiation in a medium is observed for certain crystals. It can also be induced in artificial materials by creating a preferential absorption direction. For instance a conductive wire grid with a spacing approximately equal to the radiation's wavelength effective absorbs radiation with an electric vector parallel to the grid. Also certain polymer films can be made dichroic by chemically, electrically or mechanically aligning the polymers.

A second option is to absorb one of the two orthogonal linear polarization directions using a reflection at a dielectric interface. The Fresnel equations (e.g. Born & Wolf 1975) show that if the incident angle is equal to Brewster's angle, only the component polarized parallel to the interface is reflected.

The third option is to make use of birefringent crystals. These materials have different indices of refraction for the different linear polarization directions. Uniaxial crystals can be described with an ordinary refractive index and a smaller extraordinary index along the so-called fast axis of the medium. A ray that enters such a birefringent crystal is generally split into two orthogonally polarized components due to the differences in refractive index. This behavior is used in a Glan-Thompson prism to

have one polarization component undergo a total internal reflection. Wollaston prisms deflect both beams with opposite angles.

The Mueller matrix for an ideal polarizer was given in formula 2.4. The Mueller matrices for partial polarizers are to be found in Shurcliff (1962).
The emergent intensity of unpolarized light through two ideal linear polarizers with their polarizing axes at an angle α with respect to one another is given by:

**E.4.1.** $\quad I' = \frac{1}{2} I_0 \cos^2 \alpha$.

In order to also measure the degree of circular polarization (Stokes V) conform figure 2.1 one has to convert the circularly polarized light to a linearly polarized state so it can then be identified by a linear polarizer. Therefore the phase of the leading component of the circular polarization has to be retarded such that the oscillation will be linear. The principle is illustrated in figure 4.1.a.

F.4.1.
The modification of the polarization states by
a) a quarter-wave and

$1/4\ \lambda$
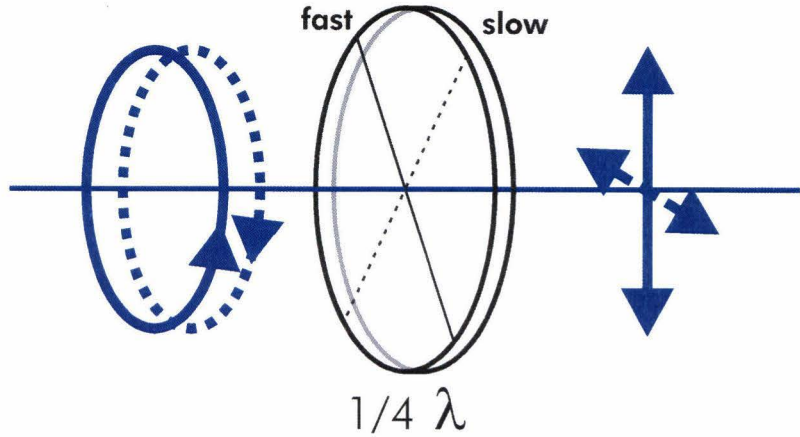
b) a half-wave retarder.

$1/2\ \lambda$
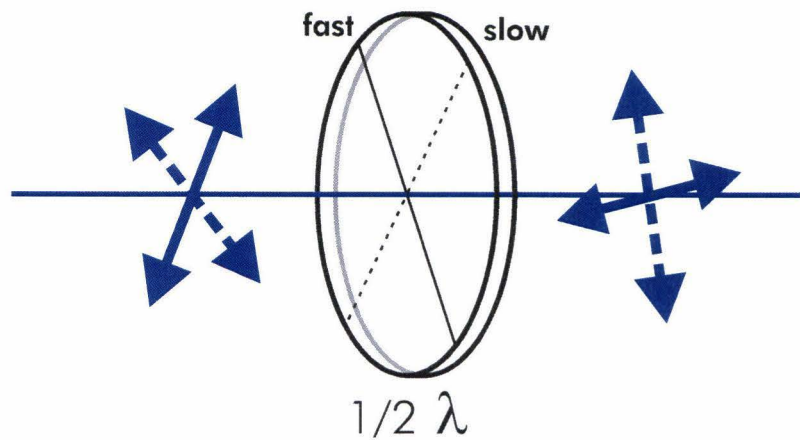
If the incident beam is right-circularly polarized, then the retarder has to induce a phase shift of a quarter of the wavelength by slowing down one component of the circular polarization to convert the polarization state to linear polarization. The resulting direction of linear polarization is at 45° with respect to this slow axis. Left-circular polarization will be converted to linear polarization at -45° with respect to the slow axis. For retardation of three-quarter wave (or minus quarter wave), these results are vice versa. Note also that linear polarization is converted into circular polarization for the reversed beam.
Such retarders can also be used to rotate the direction of linear polarization as indicated in figure 4.1.b. If the retardation is half wave, then the emergent linear polarization will be 'mirrored' around the fast axis. The direction of circular polarization then changes sign.

Birefringent components with its fast axis perpendicular to the optical path are polarization phase retarders due to the difference in refractive index between the direction of the fast axis (n_e) and the other perpendicular direction (n_o), which is the slow axis of the retarder. The retardation for a birefringent material with thickness d is caused by the different propagation velocities of the ordinary and the extraordinary ray and is given by:

E.4.2. $\delta\lambda = d(n_e - n_o)$,

where δ represents the induced phase retardance expressed in waves. The Mueller matrix of a retarder with its slow axis at 45° and parallel to the direction of negative Q is respectively given by:

E.4.3.   a) $\begin{pmatrix} 1 & 0 & 0 & 0 \\ 0 & \cos\delta & 0 & -\sin\delta \\ 0 & 0 & 1 & 0 \\ 0 & \sin\delta & 0 & \cos\delta \end{pmatrix}$ and

b) $\begin{pmatrix} 1 & 0 & 0 & 0 \\ 0 & 1 & 0 & 0 \\ 0 & 0 & \cos\delta & -\sin\delta \\ 0 & 0 & \sin\delta & \cos\delta \end{pmatrix}$.

The emergent intensity of unpolarized light with wavelength λ through a configuration with the retarder of equation 4.2 between two parallel and crossed polarizers respectively is given by:

E.4.4.   a) $I_{//} = \frac{1}{2}I_0 \cos^2\left(2\pi \frac{d(n_e - n_o)}{\lambda}\right)$;

b) $I_\perp = \frac{1}{2}I_0 \sin^2\left(2\pi \frac{d(n_e - n_o)}{\lambda}\right)$,

if the retarder's axes are at 45° from the polarizers' axes.

If in equation 4.2 $\delta<1$ then the component is a first order N wave retarder for the specified wavelength. If the phase shift is larger than one full wave, then the retarder becomes increasingly dependent on deviations from the specified wavelength. The chromatism of for instance an (n+¼) wave retarder (with n integer) is significantly reduced with an additional n wave retarder with its fast and slow axis in the direction of the slow and fast axis of the first retarder. By choosing different materials for the two retarders with opposite wavelength dependence of (n_e-n_o), the configuration can be made achromatic for a certain wavelength region.

Quarter wave and half wave retarders can be fabricated from birefringent crystals for a specific wavelength according to formula 4.2. A Babinet compensator variable retarder is obtained by sliding two crystal wedges with respect to each other so that the thickness d is varied.
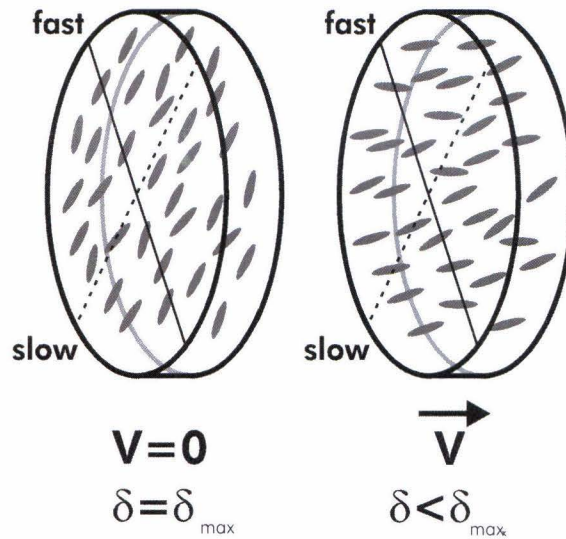The Fresnel equations show that for a total internal reflection at Brewster's angle, the induced phase shift is 45° and independent on wavelength. The combination of two or four TIRs in a Fresnel rhomb are used to create achromatic quarter wave and half wave plates.

Also nematic liquid crystals that consist of aligned birefringent molecules are bulk zero order retarders. The long axis of the crystal molecules defines the slow axis. An electric field in the optical direction induces a dipole moment in the molecules and effectively rotates them towards the field direction. This way the birefringence of the liquid crystal element is reduced as illustrated in figure 4.2.a.
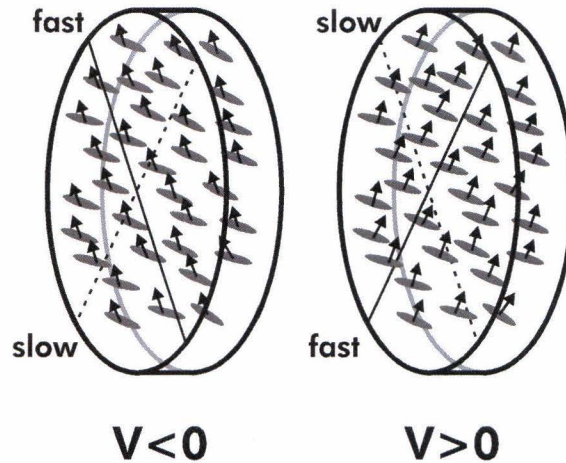
The principle of the modification of the birefringence in
a) LCVRs,

b) fLCs.

fast

slow

V=0

$\delta = \delta_{max}$

fast

slow

$\vec{V}$

$\delta < \delta_{max}$

fast

slow

V<0

slow

fast

V>0

The electric field in such a liquid crystal variable retarder (LCVR) is created between two transparent electrodes (e.g. ITO) and has to be modulated as a square wave to avoid charge build-up at the electrodes. The transition between two different values of birefringence typically takes about 10 ms. The alignment of the crystal elements is strongly dependent on the temperature. LC retarders have a large acceptance angle due to the thin birefringent layer. LCVRs can be used for a wide wavelength range due to the variable birefringence.

A second type of liquid crystal retarder consists of tilted chiral molecules with two stable states of their fixed electric dipole moment. Application of an electric field results in a transition of the dipole moment to the other state and therefore in a rotation of the slow axis of the birefringent liquid crystal as illustrated in figure 4.2.b. This rotation happens at a time scale of 100 μs and therefore ferroelectric liquid crystals (fLCs) are used as fast switching bistable retarders. Note that in this case the birefringence is constant. Only the slow axis is rotated by for instance 45° or 90°. Gisler et al. (2003) show that a Pancharatnam configuration of three fLCs can be used to create a relatively achromatic retarder.

Birefringence can be induced in otherwise isotropic optical materials by applying uniaxial strain (photoelastic effect) or a strong electric field (Kerr effect and Pockels effect in the case of crystal materials). Photoelastic modulators (PEMs), Kerr cells and Pockels cells can be used for fast polarization modulation. The drawback of PEMs is that they require resonant oscillation to modulate the birefringence and therefore it is not possible to obtain a square wave modulation. Kerr cells require high electric fields to induce a significant change in the birefringence.

Retarders are used in combination with a linear polarizer to measure the full polarization state. The simplest configuration consists of a rotating wave plate with retardance δ and a linear polarizer that 'selects' the polarization state that is converted to (partial) linear polarization by the wave plate at a certain angle. If the retardance is about 127° then all the polarization directions X are modulated with similar amplitude (Keller 2002). This way Q and U are modulated at twice the frequency of V and it requires measurements at at least eight angles to determine the full Stokes vector.

A set-up of two LCVRs and a selecting linear polarizer can measure the four Stokes components without any moving parts. The principle and the required alignment of the slow axes of both LCVRs are illustrated in figure 4.3.
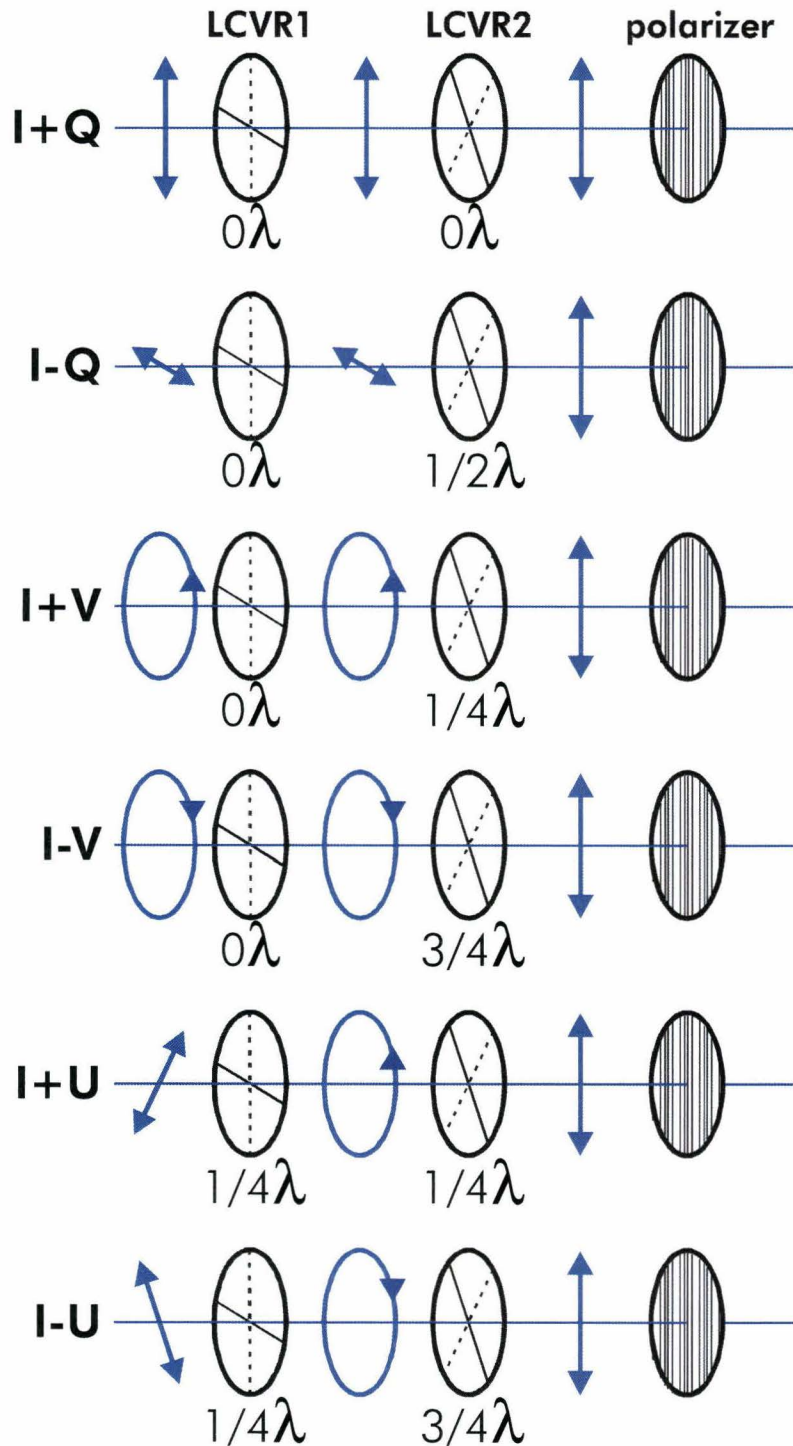
If LCVR1 at set at $\delta=0\lambda$ then LCVR2 transforms the polarization state of +Q and –Q to the polarization state of the linear polarizer by modulation between 0λ and $\frac{1}{2}\lambda$. Note that in this case the components of U and V only contribute to I in the emergent I±Q signals. Similarly this set-up is able to measure +V and –V by modulating between $\frac{1}{4}\lambda$ and $\frac{3}{4}\lambda$. In order to measure +U and –U it is necessary to first convert those polarization states to +V and –V with LCVR1 at $\frac{1}{4}\lambda$ and subsequently modulate LCVR2 to measure the circular polarization. Note that is also possible to measure the full Stokes vector with one LCVR if the whole set-up can be rotated by 45°. The modulation scheme described in Mickey et al. (1996) transmits optimal linear combinations of the Stokes components, which enables the retrieval of the full Stokes vector with four measurements.

A trade-off to the polarimeter's design lies in the choice of polarization modulation. I+X and I-X can be acquired simultaneously on different detectors (spatial modulation) or a single detector can consecutively obtain observations in I+X and I-X (temporal modulation). If the polarizer of figure 4.3 is replaced with a polarized beamsplitter (such as a Glan-Thompson or a Wollaston prism), both the positive and the negative polarization state can be measured simultaneously. A large drawback to this modulation lies in the fact that no two detectors are identical in their response. This causes errors in the determination of the polarization degree X which requires subtraction of the signals obtained by the two detectors.

On the other hand, temporal modulation on one detector causes spurious signals if the observed source has changed in the time between the two measurements. With astrophysical polarimetry the largest disturbances of the observed source are caused by refractive index inhomogenieties of the turbulent atmosphere (seeing). Temporal evolution of the observed scene is only a small contribution for high-resolution solar observations. Of course also erroneous guiding of the telescope will lead to spurious polarization signals.

Several techniques exist to counter the spurious polarization from seeing effects. Firstly, if the images in both I+X and I-X are integrated long enough for the seeing point spread function to be fully sampled, the two images will be equally washed out by the seeing and therefore not be subject to spurious signals. It is obvious that this is at the expense of spatial resolution.

A major fraction of the seeing effects can be compensated for by an adaptive optics (AO) system. Another option is the use of post-processing techniques as Speckle reconstruction (see references in Rutten et al. 2004) to remove the effects of seeing from a burst of frames. The seeing effects in each frame are determined with an atmospherical model and can then then be removed in Fourier space to retrieve the original undisturbed image. Keller & Von der Lühe (1992) show that the Speckle reconstruction technique can also be applied to the two time-modulated images in I±X to significantly reduce the effects of seeing with the use of cotemporal broad-band observations at similar wavelengths.

The third option is to use fLCs or PEMs to modulate faster than the typical change time of the atmosphere of about 10 ms. Since current CCD cameras typically require more than 100 ms for the read-out of one frame, modulation at kHz frequencies require dedicated demodulating cameras. The ZIMPOL concept (Povel 1998) consists of a PEM and a special CCD camera with on-pixel demodulation. Of each group of four pixels, three pixels are masked and one pixel receives the incident light of the area of four pixels through a microlens. Instead of reading out the full CCD array with each modulation, the charge of the active pixel is only shifted to the neighboring masked pixel and the charge of one of the masked pixels is shifted to the active pixel. This way each group of pixels builds up charge according to I±Q and I±V within the seeing change time before the entire CCD is read out. I±U is acquired by rotating the set-up by 45°. ZIMPOL is the only current polarimeter that is able to reach polarimetric sensitivity up to 10^{-5}.

The accuracy of polarimetric observations is generally limited by instrumental polarization of the telescope primary and secondary optics and by noise. The Fresnel equations govern the reflection coefficients of the linear polarization states parallel to the reflective surface (P polarization) and the orthogonal S polarization state (with S again derived from "senkrecht") from an interface with higher refractive index. The P polarized components have a higher reflection coefficient than the S components for reflection at a certain angle (which is not 0° or 90°) and therefore oblique reflections from a dielectric medium generally induce a degree of linear polarization in the direction parallel to the reflecting surface. The refracted beam will be partially polarized in the orthogonal direction.

For optical reflecting of refracting components with rotational symmetry around the optical axis these effects influence each off-axis ray to an equal extent and therefore the net induced polarization degree will be zero. It does cause a weak depolarization of a linearly polarized beam. Any deviation from rotational symmetry will cause a non-zero degree of linear polarization. Such deviations are present for all rays that originate from a source that is not on the optical axis. Seeing can also introduce this effect for axially symmetric rays (Sánchez Almeida & Martinez Pillet 1992). In telescopes the rotational symmetry of the primary mirror's aperture is mostly broken by the presence of the obstructive secondary optics and its support structure.

In case of a total internal reflection (like in a Fresnel rhomb) there will be a phase shift between the S and P components, resulting in cross-talk between the linearly polarized components and the circular polarization.

No piece of glass can be considered to have a uniform index of refraction. Due to internal stresses in the glass a certain amount of random birefringence will be present in each lens and each planar component (e.g. filters and entrance/exit windows). For regular BK7 glass the amount of random retardation is about 5 nm per centimeter of glass (Keller 2002). This effect is about 12 times less for fused silica.

Scattered light from unpolarized sources, for instance by mirror dust, generally leads to a reduction to the polarization degree X/I. It can cause a significant linearly polarized signal, especially when observing off the limb (Keller 2002). Also ghost images contribute to errors in the observed polarization signal.

If the axes of the polarization modulators are not aligned accurately enough, this will lead to deviations for the desired modulation. This is also the case if the desired phase retardation is not fulfilled by the retarder for instance due to chromatism of a wave plate and due to incorrect calibration, temperature effects, inhomogenieties or dependency of the transmission on the retardance setting of a LCVR.

The noise level of a polarimetric observation at intermediate resolution is generally dominated by the photon noise of the regular unpolarized observation. An observation in Stokes X is obtained by the difference of the measurements of $\frac{1}{2}(I+X)$ and $\frac{1}{2}(I-X)$, but the photon noise is governed by Poisson statistics is therefore approximately equal to the square root of the sum of $\frac{1}{2}(I+X)$ and $\frac{1}{2}(I-X)$. The noise is enhanced when determining the polarization degree X/I.

CCD cameras also have an intrinsic read noise which contributes to the noise level independent of the light intensity. A non-linear response of the camera to increasing light levels will create an unbalance between the observations of $\frac{1}{2}(I+X)$ and $\frac{1}{2}(I-X)$ and therefore lead to an underestimate of I, X and X/I when the response is sub-linear.

5. Design of the Ba II 4554 / Hβ channel

This chapter gives a full overview of the optics, hardware and software of the Ba II 4554 / Hβ imaging polarimeter on the DOT. The first two sections sketch the context of the design. Section 5.3 will focus on the details of the Ba II 4554 / Hβ channel itself.

5.1. The Dutch Open Telescope

The Sun has a similar spectral intensity per steradian as any G-type stars; its solid angle is only much larger due to the Sun's proximity. The huge energy flux from the Sun puts important constraints on the construction of a solar telescope. A primary mirror with a diameter of 0.5 m (which is considered tiny by the current night-time standard of about 8 m) already generates so much heat in its focus (~200 W), that the resulting atmospheric turbulence (seeing) drastically limits the spatial resolution of the observations. This effect is avoided by building the telescope inside a big vacuum chamber with the entrance window also serving as the primary imaging component. This principle is successfully applied for the 1 m Swedish solar Telescope (SST; Scharmer et al. 2003). Current vacuum technology limits this design to apertures of about 1 m.

Another approach to the seeing problem was pioneered in Utrecht in the 1970s. It relies on a stable wind to 'flush out' the telescope of turbulences. Such an open telescope construction has to be mechanically stiff to avoid wind shake of the optical components which cause pointing inaccuracy, image shake, defocusing and image deformation. The dome that protects the telescope from severe weather conditions has to be completely retractable and therefore takes the form of a clamshell canopy. It is advantageous to put the telescope on a stiff, open tower to place the telescope in higher more stable air layers. A tower based on isosceles triangles is only susceptible to translational motion and not to rotational motion, which is a requirement for accurate pointing. The open tower allows flushing of the turbulence caused by ground layer heating. It also prevents the creation of turbulences by deflection of the wind itself.

The Dutch Open Telescope (Rutten et al. 2004a) was built conform these design criteria on the Canary Island of La Palma and it saw first light in 1997. The current configuration is shown in figure 5.1.

The DOT is located at the Observatorio del Roque de los Muchachos at 2.4 km above sea-level close to the SST. This site has excellent diurnal weather and seeing conditions (Rutten et al. 2004a) and is frequently hit by a laminar trade-wind from the north. The 45 cm primary mirror and the highly accurate optics in principle allow solar observations with a diffraction limit of 0.2" in the blue wavelengths. The secondary optics of the DOT is in its entirety mounted on top of the telescope and is discussed in detail in the next section.

The Dutch Open Telescope on La Palma.

Typical seeing conditions usually still inhibit observations at the diffraction limit and therefore the images are post-processed with the Speckle reconstruction technique (see Rutten et al. 2004a and references therein). Speckle processing of a day's worth of data is sped up significantly with the commissioning of a water-cooled 70 CPU parallel processor.

The combination of a revolutionary design, an excellent location and Speckle processing, enables the DOT to observe the Sun at the telescope's diffraction limit for the duration of several hours. These observations are not subject to image rotation due to the telescope's equatorial mount. With its multi-wavelength imaging system (see next section) the DOT specializes in cotemporal and cospatial high-resolution tomographic movies of the solar atmosphere. These observations cover a wide range of dynamic processes on the Sun and are particularly complementary to ground-based spectropolarimetric observations and UV observations of the corona from space.

5.2. The DOT multi-wavelength system

The optical configuration of the DOT is schematically depicted in figure 5.2.

F.5.2.
The configuration of the DOT multi-wavelength channel optics. From Bettonvil et al. (2003).
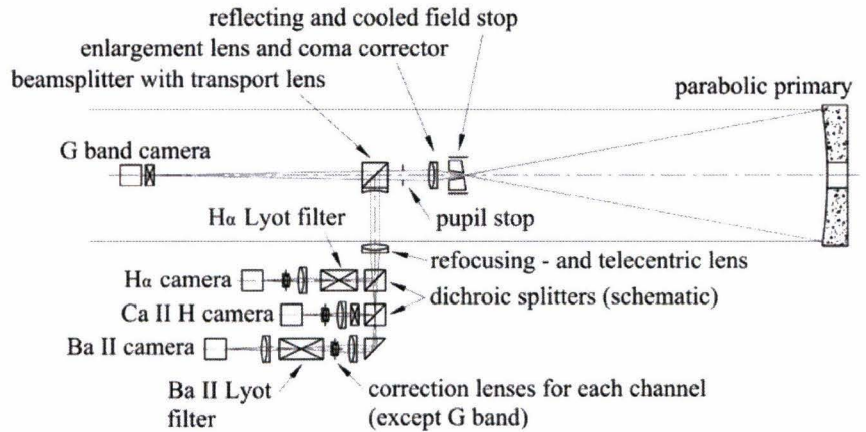
The 45 cm parabolic mirror has a focal length of 2 m. There a field stop is located that reflects about 90% of the light and constricts the transmitted field diagonal to 3'. Additional cooling is obtained by water circulation and air suction.

The F/4.44 beam is re-imaged by a 10x magnifying lens combination (L1, L2), which is corrected for spherical aberration and corrects the coma of the parabolic primary mirror at the spectral region around 4305 Å. This lens system also forms a nearby image of the pupil (the primary mirror). Here a pupil stop is located to reduce the amount of stray light and to cover the outer parts of the primary mirror. The effective entrance pupil is 438 mm in diameter at the mirror surface, where the back image of the pupil stop is formed. Hence, only a rim of 6 mm wide is not used for eliminating the unavoidable less excellent shape of the extreme edge.

80% of the final F/45 beam is split off by a beamsplitter (BS1) into the multi-wavelength system (see below). A narrow wavelength range of the remaining 12% of the beam is selected by a 10 Å broad interference filter at 4305 Å (G band). The diffraction limit of 0.2" at 4305 Å at the secondary image plane is fully Nyquist sampled with 10 bits 6.7x6.7 μm^2 (which corresponds to 0.07"x0.07") pixels of the 1296x1030 px^2 Hitachi KP-F100 CCD cameras that can attain a read-out rate of 12 frames/s with a read-out time of 87 ms. The field of view that is sampled by the camera is 92"x73". With a photospheric sound speed of about 7 km/s it takes about 20 s for the solar scene to evolve significantly at this resolution, which imposes a maximum time duration to one Speckle burst. This criterion is not met for some chromospheric and supersonic shock phenomena.

Focusing is achieved by sliding the entire set-up from the field stop to the G band camera along the optical axis. It is controlled by a feedback loop with the focus camera, which feeds of light reflected by the G band filter and BS1. This way the focusing system is applied as a zero order AO system for atmospheric correction. The beamsplitter and the multi-wavelength system are fixed.

The light going into the multi-wavelength system is firstly converted into a near-collimated transport beam by a negative lens L3, which is cemented to BS1. L4 refocuses the beam to its original convergence and also serves as telecentric lens by imaging the pupil plane at infinity. This way the transmission through spectral filters is independent of the place in the image and the field size is invariant to defocusing by seeing, which is advantageous for Speckle reconstruction. At the final image planes the effective focal length is 20 m and the beam can therefore be considered to be near-telecentric.

The multi-wavelength was designed to obtain images in six wavelength bands. The specific wavelengths are given in table 5.1. The current situation also requires the construction of a seventh channel and the relocation of the focus camera (see below).

channel	wavelength [Å]	filter FWHM [Å]	tuning
G band	4305	10	fixed interference filter
blue continuum	4319	6	fixed interference filter
Ca II H	3968	1.28-1.35	tiltable interference filter
red continuum	6550.5	2.5	tiltable interference filter
Hα	6563	0.25	tunable Lyot filter
Ba II 4554 / Hβ	4554 / 4861	0.08 / 0.09	tunable Lyot filter
Ba II 4554 / Hβ continuum	4505 / 4817	6 / 6	fixed interference filter

In the multi-wavelength system the light is split into three wavelength ranges by two dichroic mirror beamsplitters (BS2 and BS3). The first one transmits the red wavelengths to the Hα channel and the red continuum channel. The reflected beam is consecutively split by reflecting the violet wavelengths required for Ca II H. The remainder of the light is divided between the blue continuum channel and the new Ba II 4554 / Hβ channel, its reconstruction channel and the focus camera. This optical configuration is discussed in detail in section 5.3.1. The final split channels are each equipped with a wavelength filter as indicated in table 5.1. The images in each of the channels are acquired with identical cameras as for G band which are all synchronized. Due to the long optical paths, the secondary foci of all the channels except blue continuum are located somewhere along the way. Therefore the beams have to be re-imaged yet another time. This also creates a new pupil plane which is used to correct for aberrations (sphecrical aberration and coma) that are not completely corrected for by L1 and L2 at the specific wavelength, which deviates from the region around 4305 Å. This effect is called sphero-chromatism. Also coma is slightly dependent on the wavelength. By inserting meniscus lenses of negligible power near the pupil plane, the amount of spherical aberration and coma is corrected for completely.

More details of the multi-wavelength system are to be found in Bettonvil et al (2003).

Observations in narrow wavelength bands at this high spatial resolution are almost as photon starved as observations of any other G-type star. The signals through the extremely narrow Lyot filters at Hα and Ba II 4554 / Hβ (see section 5.3.2) are therefore too weak to accurately Speckle reconstruct. Due to the many optical components, the moderate quantum efficiency in the blue, the 80 mÅ band-pass and the low intensity of the deep Barium line it takes about a second to fill up the full well capacity of the CCD while a maximum exposure of 100 ms is allowed for sampling the atmospheric disturbance. The atmospheric phase information for reconstruction of Hα and Ba II 4554 / Hβ bursts is therefore obtained from the corresponding burst in the much broader nearby red continuum channel and the Ba II 4554 / Hβ reconstruction channel respectively according to the method described by Keller & Von der Lühe (1992).

### 5.3. Optical design of the Ba II 4554 / Hβ channel

5.3.1. The imaging optics

The largest part of the imaging optics design for the Ba II 4554 / Hβ channel as presented by Bettonvil et al (2003) has been found useful to adopt for the full polarimeter's design. The Zemax ray-tracing model of the final design for the imaging optics is depicted in figure 5.3.

F.5.3.

The Zemax model of the imaging optics.
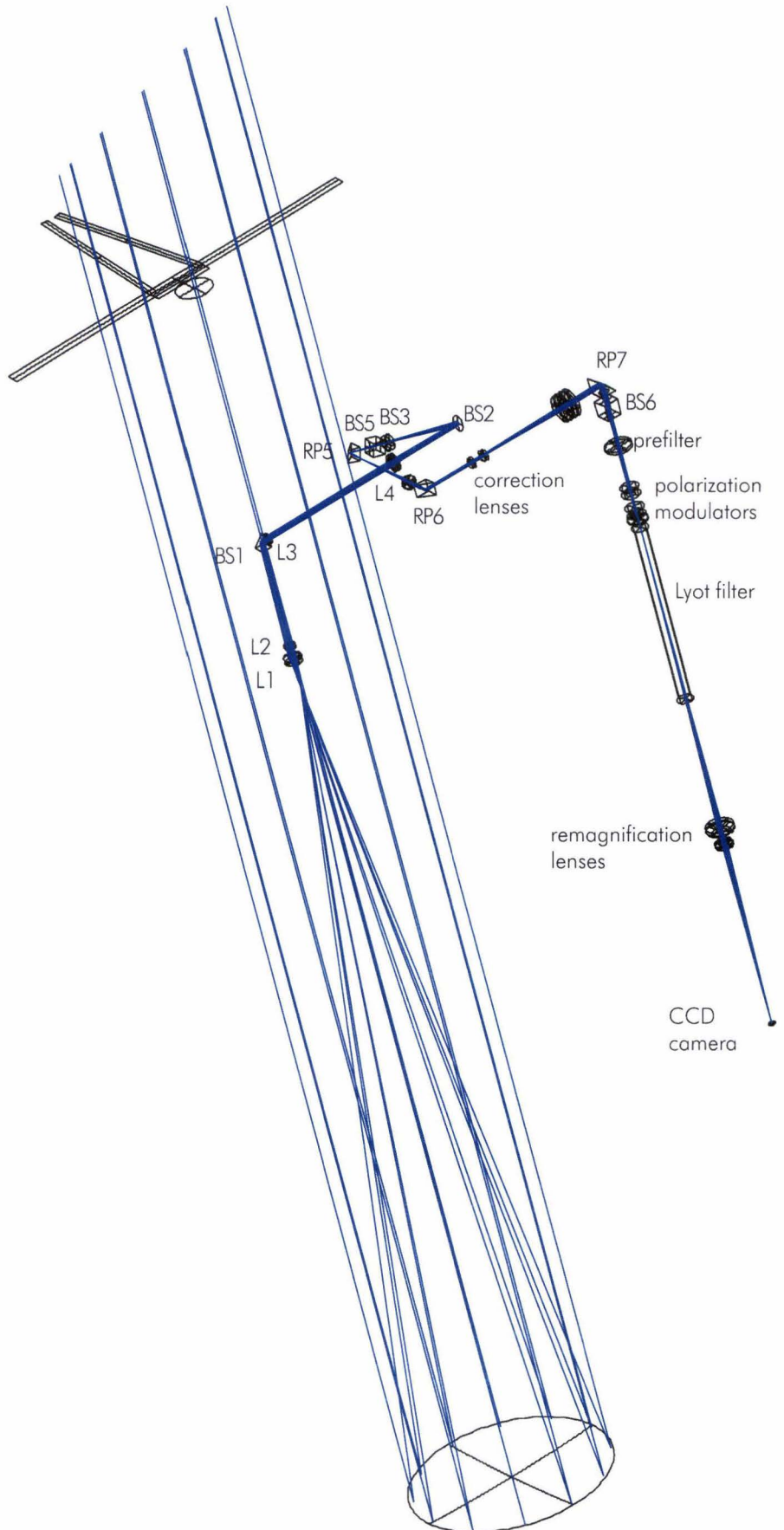
At the entrance of the multi-wavelength system, the two dichroic mirrors (BS2 and BS3) are placed at an 8° angle to fully split the beams and still minimize the introduced amount of astigmatism. After the final (transmitting) dichroic mirror the light for the blue continuum channel is split off by a 90% transmitting beam-splitter BS5. The remaining light is dedicated for the Ba II 4554 / Hβ channel and its reconstruction channel (plus the focus channel). It has to be transported by right-angle prisms all around the existing channels due to mechanical constraints caused by the size of the Barium Lyot filter (see the figures in the next section). Therefore the beam has to be re-imaged twice. The first image plane is not located in close proximity to any optics to avoid a strong dependence of the final image quality on the surface quality of the optics. Near the first pupil plane there are two correction lenses to correct for aberrations at 4554 Å. The next lens images the pupil to infinity again to feed the filters and polarization optics with a telecentric beam.

The prefilter stage of the Lyot filter is dismantled from the original filter construction. A new set of prefilters for Ba II 4554 and Hβ is now located in front of the polarization optics to reduce the heat load. The set-up of the polarization modulators is described in detail in section 5.3.3. All the polarization optics can be transported out of the beam and replaced with planar glass pieces with equal focal displacement. The polarization modulators use the entrance polarizer of the Lyot filter as their 'selection' polarizer to avoid light losses by inserting an additional polarizer in the beam. Therefore the polarization modulation is performed almost at the end of the optical path. Ideally the polarization modulation is performed before BS1, but this would also affect all the other channels.

The third image plane is located within the Lyot filter due to its limited field acceptance. The filter has to be positioned such that the image plane is not coincident with an optical surface. The beam is then finally re-imaged again to form its final image plane on the camera's CCD. Due to 8° reflection at BS2, the camera has to be rotated by 16° around the optical axis.

Because the beam is already corrected for aberrations at that point, it is possible to build in a demagnification system to increase the photon flux on the pixels by a factor of two. By sliding the final lens set approximately 100 mm further into the beam and pushing back the camera by about 40 mm, the field size is increased about √2 to just fit within the 3', which is determined by the field stop, of course decreasing the resolution by the same amount.

The light for the reconstruction channel is split off from the Ba II 4554 / Hβ channel right before the filters and polarization modulators with BS6 (90% transmission). Its optical configuration is equal to that of the final part of the main channel including demagnification, with the exception of the polarization modulators and the Lyot filter. Its filter wheel contains interference filters as specified in table 5.1.

Figure 5.4. shows the through-focus spot diagrams in the final image plane. It is clear that all traced rays are well within the system's Airy disk, allowing for some fabrication and alignment margin of the optics. The focus at the wavelength of Hβ is located about 1.5 mm after the focus at Ba II 4554. In spite of the large focal depth it may therefore be necessary to shift the camera by that amount when switching from Barium to Hβ observing mode. It is also clear that the correction of the aberrations is optimal for Ba II 4554 and only acceptable for Hβ.

F.5.4.
Through-focus spot diagrams with steps of 0.5 mm at the image plane of the Zemax model of figure 5.3. Blue denotes a wavelength of 4554 Å and green represents 4861 Å (Hβ).
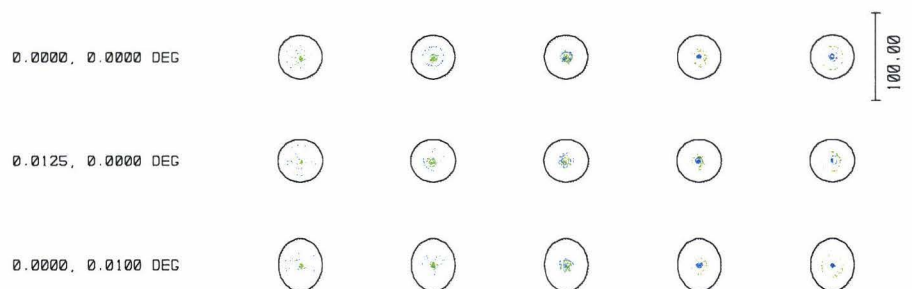

The transmission of the full system was calculated by Zemax to be 16%, not even including the factor of ½ due to the Lyot filter's entrance polarizer.

5.3.2. The Lyot filter

The wavelength dependence of a retarder which is sandwiched by linear polarizers is given by formula 4.4. By cutting a piece of birefringent material such that it has a maximal transmission between two crossed polarizers at a certain wavelength and creating an optical train of polarizers and birefringent materials with thickness ratios of 1, 2, 4, 8, etc. conform figure 5.5, the resulting transmission will show separated narrow spectral bands.

The principle of the Lyot filter. From Lyot (1944).
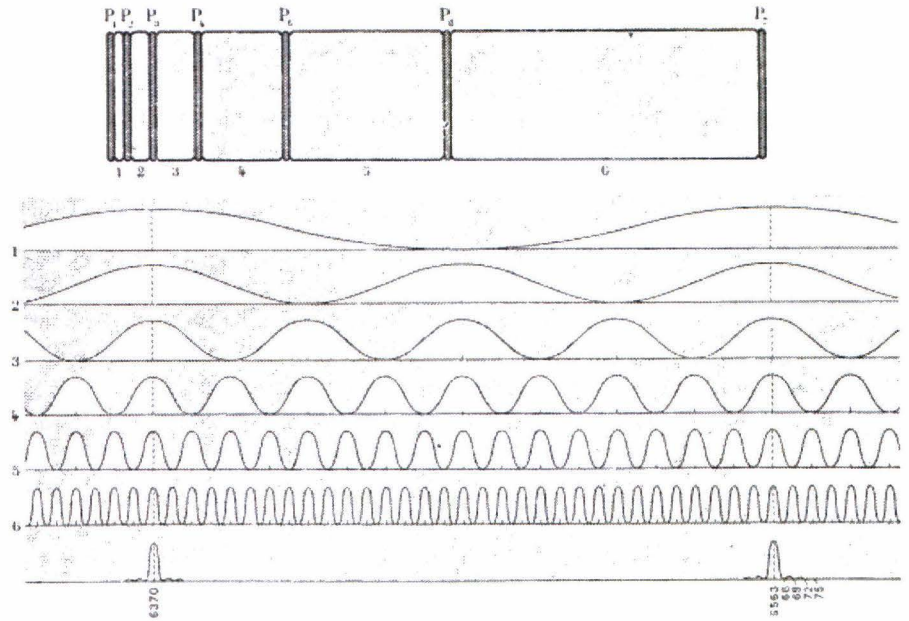
It is clear that the band-pass of such a Lyot filter (Lyot 1944) is determined by the thickest birefringent stage and that the peak separation is determined by the thinnest stage.

This design was improved upon by Evans (1949) by introducing a splitting component in each birefringent stage (see figure 5.6.a), effectively reducing the number of polarizers. The introduction of a splitting half wave plate like in 5.6.b results in elliptical interference fringes instead of hyperbolic ones. This indicates that the field acceptance is much larger than in the original configuration, better suiting the filter for wide-field (solar) observations than Fabry-Perot etalons.

The filter can easily be converted into a tunable filter by introducing a variable phase shifter as the splitting component (see figures 5.6.c and d). Such a component can consist of two fixed quarter wave plate and a rotating half wave plate.

F.5.6.

a) Configuration of a Lyot filter with Evans split.
b) Configuration of a wide-field Lyot filter with Evans split.
c) Configuration of a tunable wide-field Lyot filter with Evans split.
d) Configuration of a fully tunable wide-field Lyot filter with Evans split.
From Aleksandrovich et al. 1975.
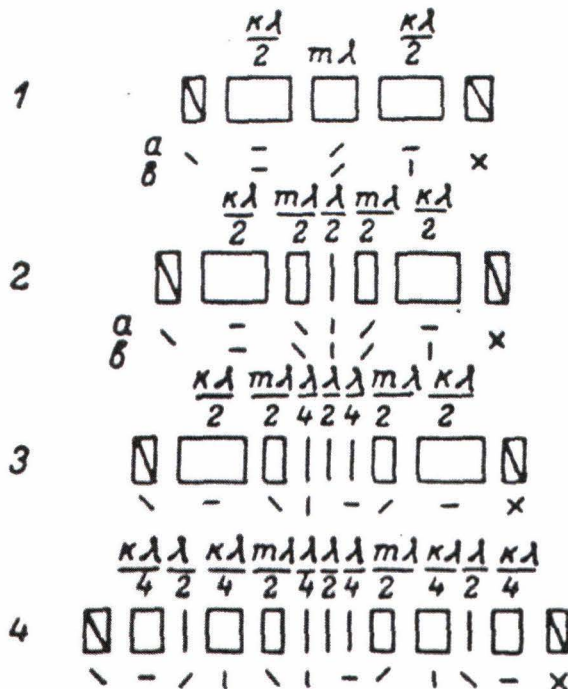
A tunable Lyot filter optimized for Ba II 4554 and Hβ was built by Aleksandrovich et al. 1975 in Irkutsk. Its optical configuration is presented in figure 5.7.

F.5.7.

Optical and mechanical configuration of the Ba II 4554 / Hβ Lyot filter built by Aleksandrovich et al. 1975.
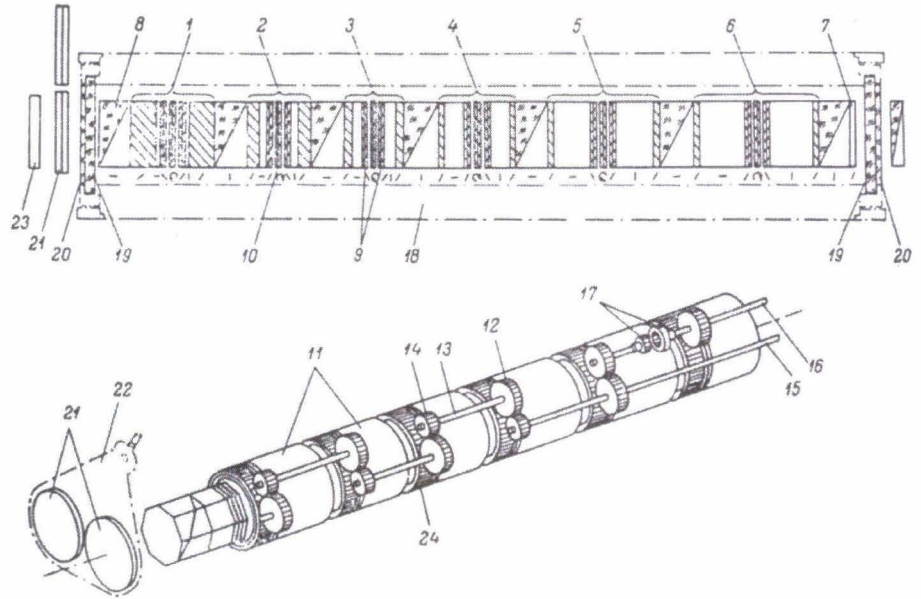
The filter consists of twelve birefringent stages of which six are made of strongly birefringent calcite and six of quartz, which is only weakly birefringent. To reduce the number of polarizers, each stage consists of an Evans split calcite stage and a quartz stage. The prism polarizers are consecutively crossed to minimize the introduction of astigmatism.

The band-pass of the filter is determined by the thickest calcite stage of 60 mm, which also has a role of correcting stage. The other five calcite stages have thicknesses of 52 mm, 26 mm, 13 mm, 6.5 mm and 3.25 mm. The amount of birefringence is kept constant by regulating the immersion oil temperature at 38.5 °C with a thermostat controller. By adjusting the rotating half wave plate in the thickest stage it is possible to optimize the pass-band around 4554 Å and 4861 Å. The quartz stages determine the separation of the transmission bands of about 95 Å around 4554 Å and 110 Å around 4861 Å. Interference filters are used to suppress the transmission features other than the pass-band at those two wavelengths.

Due to the configuration with crossed polarizers it is easy to rotate all the half wave plates with the correct ratio with the use of simple 2:1 gears. An additional gear with ratio 15:13 is between the half wave plates of the stages with 60 and 52 mm calcite. The adjustable calcite stages allow tuning within ±1.5 Å from the central pass-band. The quartz stages are not tunable and therefore they will generate ghost peaks when tuning further away from the central wavelength. It is therefore also necessary to tune an additional correction stage at the entrance by rotating its entrance polarizer and to raise the operating temperature by 2 °C to accurately 'set' the quartz stages when switching from observations in Ba II 4554 to Hβ. Also the calcite correction stage has then to be adjusted by rotating the exit polarizer.

Spectroscopic measurements by the manufacturers determined the pass-band of the current configuration to be 0.08 Å at 4554 Å and 0.09 Å at 4861 Å. The transmission of the filter at Hβ but operating at the temperature of Ba II 4554 showed some minor ghost peaks around the central band-pass of 0.09 Å (Skomorovsky, private communication). Measurements of the filter with a 50 W light source, an additional polarizer, an optical chopper and a photo-detector feeding a lock-in amplifier show that the polarization direction of the entrance filter operating at 4554 Å as fixed by the manufacturers is at 138° from the vertical. For Hβ it is at 152° at elevated temperature and its optimal band-pass at 38.5 °C is obtained with the entrance polarizer at 148°. These settings determine the alignment of the polarization modulators. The exit polarizer has to be rotated by more than 90° when switching from Ba II 4554 to Hβ. The filter's throughput of only the transmission band at 4554 Å was not measurable even with the lock-in detector, which according to the specifications of the used equipment establishes the transmission of the filter to be 10% at maximum. Currently the transmission is being improved on by renewing the immersion oil.

5.3.3. The polarization optics

The desired flexibility of the polarimeter determines the selection of liquid crystal variable retarders (LCVRs) as polarization modulators. The tunable birefringence of these elements allows specific wavelength calibration, rotation of the axes of linear polarization and compensation of instrumental cross-talk. Due to the thin birefringent polymer layer, the acceptance angle of LCVRs is high. The three LCVRs purchased form Meadowlark optics have excellent optical quality and their operating temperature can be controlled.

The Ba II 4554 / Hβ channel is equipped with the same camera as all the other channels to obtain tomographic observations of the same field and resolution. The modulation speed of the LCVRs (<20 ms) is fast enough for the read-out time of this camera. Only a dedicated demodulating camera would require faster modulators such as fLCs.

Four LCVRs can be simultaneously controlled by one computer interface. Unfortunately only one LCVR temperature controller can be addressed at the same time.

The characteristics of the LCVRs were measured in a laboratory environment with low ambient light levels, low dust contamination and a controlled temperature. The LCVR was set-up between parallel and crossed polarizers with its axes at 45°. From equations 4.4.a and b it can be derived that the retardance of the LCVR is obtained by:

E.5.1.
$$\delta = \tfrac{1}{2}\arccos\left(\frac{I_{/\!/} - I_{\perp}}{I_{/\!/} + I_{\perp}}\right),$$

after dark subtraction of the measured intensities.

The locations of n/2 wave (with n integer) are also easily obtained by locating the extrema of either curve. The points of (n/2 + ¼) wave are then located halfway between the values of the extrema if the detector is linear.

The acquired curve of one LCVR's retardance at 4554 Å as a function of applied voltage is presented in figure 5.8.b and compared with the curve supplied by the manufacturer. It is clear that the curve is accurately reproduced with the exception of the n/2 wave points. This is due to the steepness of the arcos function at those points. The real values of the retardance are in those cases more accurately represented by the determination of the extrema of the signals in figure 5.8.a.

F.5.8.

Measured curves as a function of the applied voltage for one of the LCVRs.
a) The dark-subtracted signals with parallel and crossed polarizers.
b) The obtained retardance curve.
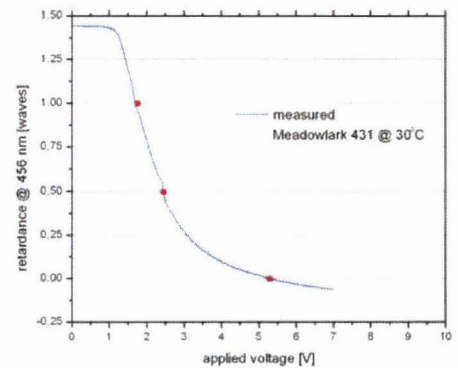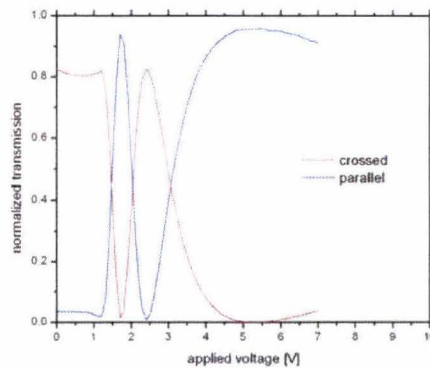
The retardance curve in terms of absolute wavelength units is slightly chromatic. Therefore the retardance settings for 4554 Å cannot be proportionally adopted for 4861 Å.

The homogeneity of the LCVR was determined by aligning its fast axis with the entrance polarizer. Modulation of the LCVR showed no significant change in the minimal output signal for rotations of ±1°.

Measurements by the manufacturer of the same curve as in figure 5.8.b as a function of temperature shows that the retardance of the element is reduced by 2 nm/°C.

The transmission of the LCVR may differ at zero and maximal applied voltage due to change in internal structure. However, this effect was not accurately measurable with the set-up.

The design of the polarization modulation package is illustrated in figure 5.9.
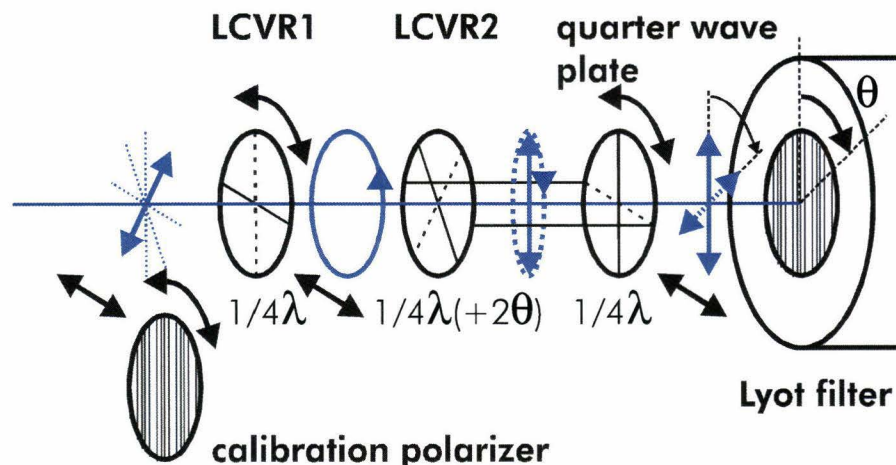
The principle of the modulation is the same as in figure 4.3. An additional polarizer can be inserted in front of the LCVRs to enable calibration measurements similar to figure 5.8. This calibration produces a table of voltage settings for the required retardances at the operating wavelengths (4554 and 4861 Å) and temperature. The calibration routines are described in detail in section 5.5.

The LCVRs can be inserted into the beam individually. Therefore it is possible to only utilize LCVR2 if only measurements in Stokes V (and/or Q) are required. Usually only this LCVR will be temperature controlled.

Both LCVRs are aligned with the Lyot entrance polarizer. If the operating wavelength of the filter is switched from Ba II 4554 to Hβ, this polarizer has to be rotated. If the polarization axes of the Stokes vector are required to be fixed for both observations, the directions of linear polarization can be rotated to match the axis of the polarizer by the additional quarter wave plate, which is fixed to LCVR2. If the polarizer is rotated by an angle θ, then the retardance of LCVR2 has to be increased by 2θ to feed the quarter wave plate with the correct elliptical polarization. As indicated in figure 5.9, the quarter wave plate will convert this elliptical polarization to the required linear polarization. The new settings for LCVR2 will be automatically obtained by performing the standard calibration with the additional polarizer.

This quarter wave plate will not influence regular magnetogram observations if the LCVRs are aligned with the Lyot filter's entrance polarizer, provided that also this quarter wave plate has excellent optical quality. A choice of a zero order quarter wave plate at 4700 Å will introduce an underestimate of approximately $0.1\% \cdot \sin^2 2\theta$ in the determination of Stokes Q, U and V. The cross-talk components $U, V \leftrightarrow Q$ will then be of the order $5\% \cdot \sin 2\theta$. In principle this can be compensated by modifying the retardance setting of LCVR1, which is aligned with the axes of the quarter wave plate. But if only Stokes V and/or Q is observed, it may be better to only insert LCVR2 as the expected cross-talk from LCVR1 may also be of the order of several percents.

Since the LCVRs are rotatable by themselves, their axes can also be rotated to match the linear polarizer's axis. The rotation of the LCVRs' axes can be used to choose the direction of Stokes Q and U on the Sun. The quarter wave plate then compensates for any deviation between the LCVR axes and the polarizer's axis. However, the dynamical range of the LCVRs' retardance (see figure 5.8.b) only allows compensation of all required retardance settings $(0/1\lambda, \frac{1}{4}\lambda, \frac{1}{2}\lambda, \frac{3}{4}\lambda)$ for a rotation of about -90° and +45° with respect to the polarizer's axis. This rotational freedom enables the observer to choose the direction of either +Q or –Q parallel to the solar limb, which is preferable for Hanle and beam impact measurements (see sections 2.2.2 and 2.2.3).

Due to the many optical components, a significant amount of instrumental cross-talk can not be avoided. The largest contributions are to be expected from the three cube beam-splitters in the optical path and the three ight-angle prisms (RPs). To reduce their effects these components are taken in pairs positioned at 90° to cancel each other's effect. The induced degree of linear polarization and the retardation due to the dielectric layer in BS1 is canceled by a similar reflecting layer on the hypotenuse of RP5, even after the reflection on BS2. At first, an aluminium layer

will be coated on RP5, but if this does not mimic the effects of BS1 accurately enough, BS1 will be refabricated in two duplicate versions. The second version will then serve as RP5, despite some additional light losses. BS5 and BS6 are equal optical components and are both passed in transmission. They are also set-up at 90° respective to each other to cancel their (small) polarizing effects. RP6 and RP7 are also positioned at 90° and can therefore be used in TIR to avoid further light losses. Mirror dust is a particular problem for the DOT as the primary mirror is occasionally hit by eastern winds containing Sahara sand. To minimize the amount of instrumental polarization due to stray light, the mirror has to be frequently cleaned.

The remaining instrumental polarization will be due to the dielectric layers of the two dichroic mirrors at 8°. The large amounts of glass that the beam has to pass will introduce considerable retardance of about 20°. Therefore it is necessary to measure the instrumental Mueller matrix to be able to analyze polarimetric observations. Because the DOT is an equatorial telescope, this instrumental polarization will not be variable during the day or during the year. A calibration unit has been designed to measure the instrumental Mueller matrix due to the optics from BS1 to the polarization optics. The calibration procedures are discussed in section 5.5. It was not possible to design a reliable calibration unit that covers the entire aperture with polarizer sheets, firstly because no accurate circular polarizer sheets are available at the required wavelength and secondly due to stability issues in the wind. A calibration unit located before the field stop is not viable due to the large heat load and the fast converging beam.

The Mueller matrix due to the non-circular aperture (see figure 5.3) was calculated by Keller (private communication) to be:

E.5.2.

$$
\begin{pmatrix}
1.000000 & -0.000026 & -0.000005 & 0.000000 \\
0.000026 & -0.999997 & 0.000000 & 0.000001 \\
-0.000005 & 0.000000 & 0.999997 & 0.0000004 \\
0.000000 & -0.000001 & 0.000004 & -0.999993
\end{pmatrix}
$$

and can therefore be neglected. The measured instrumental Mueller matrix should be clear from minus signs in their diagonal components. The matrix has to be multiplied twice (right and left) with the rotation matrix of formula 2.6 if the axes of Q and U are chosen differently from the axes of the instrumental Mueller matrix.

When the instrumental Mueller matrix is known, the LCVRs can be used to counter the retardance of the other optics. If the instrumental Mueller matrix takes the form:

E.5.3.

$$
M_{instr} = T
\begin{pmatrix}
1 & Q \to I, O(1) & U \to I, O(1) & V \to I, O(1) \\
I \to Q, O(1) & Q \to Q, O(0) & U \to Q, O(2) & \sim \sin\alpha \\
I \to U, O(1) & Q \to U, O(2) & U \to U, O(0) & \sim \sin\beta \\
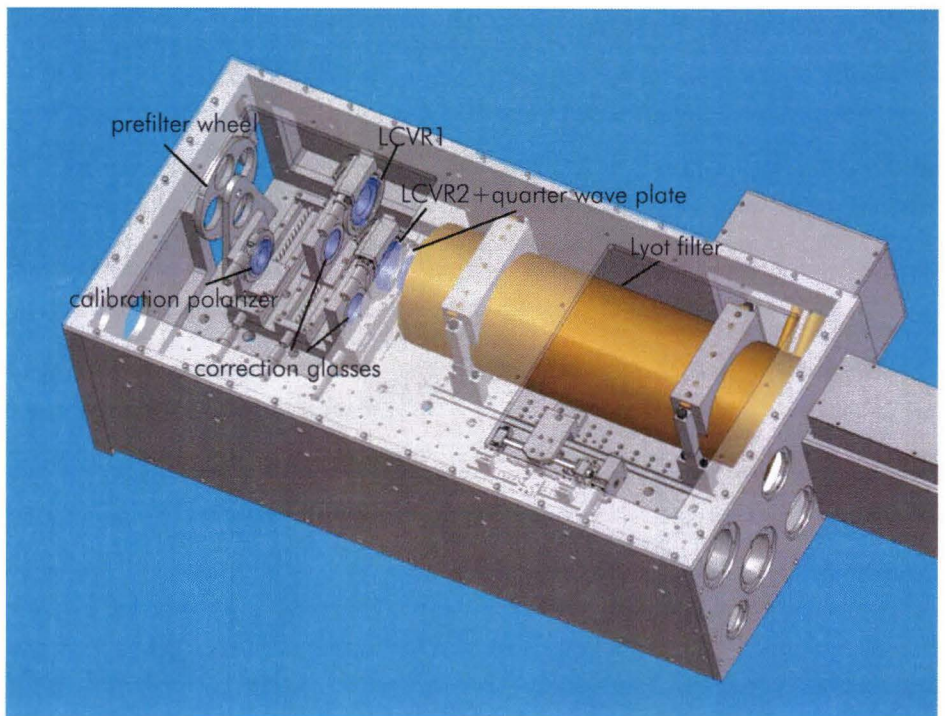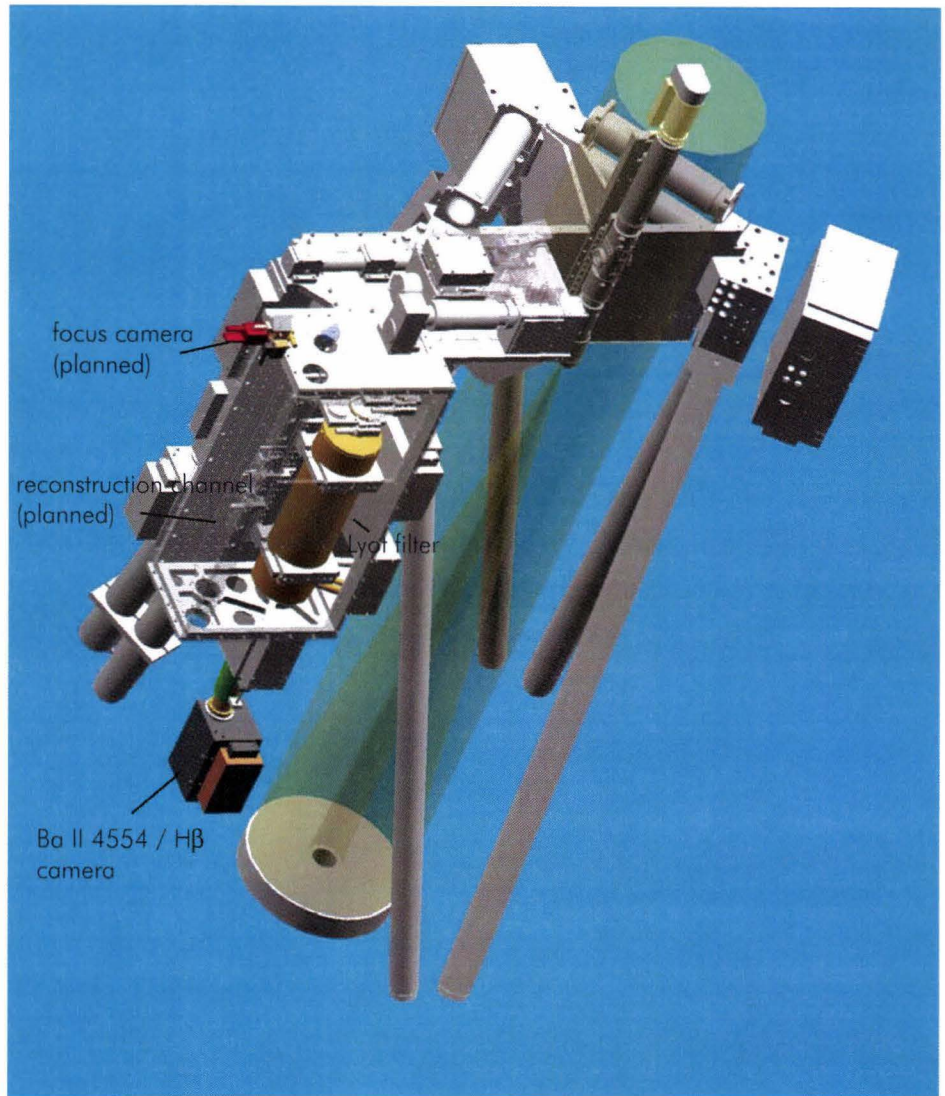I \to V, O(1) & \sim -\sin\alpha & \sim -\sin\beta & V \to V, O(0)
\end{pmatrix},
$$

then it can be diagonalized to first order by increasing the retardance settings of LCVR1 by β and the settings of LCVR2 by α. Note that this instrumental Mueller matrix represents an average across the field and that therefore inhomogenieties may exist. The dichroic components I↔X and their higher order effects in for instance Q↔U can not be compensated with the LCVRs. Therefore the final instrumental Mueller matrix should be carefully considered with the interpretation of all polarimetric observations with this set-up. Camera non-linearities are not covered by this matrix. The measurement in the instrumental Mueller matrix should be performed at least once a year.

5.4. Mechanical design of the Ba II 4554 / Hβ channel

The current design status of the Ba II 4554 / Hβ is presented in figure 5.10.

focus camera
(planned)

reconstruction channel
(planned)

Lyot filter

Ba II 4554 / Hβ
camera

prefilter wheel

LCVR1

LCVR2 + quarter wave plate

Lyot filter

calibration polarizer

correction glasses

The plate that supports the Lyot filter and the polarization optics will actually form the top side of the box that contains all the active components after installation on the telescope to ensure stiffness of the construction. The maintenance hatches will then be located at the bottom of the multi-wavelength system when the telescope is in its parking position. The Lyot filter is suspended such that it is in its regular upright position during tracking of the Sun to ensure the correct extraction of air bubbles in the immersion oil.

Because all the optical components are out of reach during observations, all active components have to be controlled from a remote location. Therefore all the moving parts are motorized to give the observer full flexibility. The tuning of the Lyot filter is performed by turning a single wheel, which is performed by a Maxon gear motor with precious metal brushes and linear servo amplifier. This solution is equal to the tuning of the Hα Lyot filter and is selected due to the motor's low noise signal in order not to interfere with the CCD cameras. All the other moving parts are not operated during observations and are therefore driven with the robust and simple in use brushless Faulhaber motors with pulse width modulated amplifiers. It takes a total of 15 actuators to select the prefilter of both channels, to translate the LCVRs and the calibration polarizer, to rotate them, to position the Lyot filter for optimal image quality, to rotate the filter's entrance and exit polarizer and to translate the final lens set and the camera for demagnification of both channels. Unfortunately no satisfactorily robust solution was found to rotate the entire polarization modulation package all at once to reduce the number of actuators. All the Faulhaber controllers can be daisy-chained to allow for communication by a single computer connection. The computer control of all the active components is discussed in the next section. The camera is aligned manually.

The box containing the active components is thermally isolated and therefore subject to active heating by the Lyot filter and passive cooling at the wall. It has to be tested how long it takes to establish thermal equilibrium for typical observing circumstances. The optical input to and output from the box has been designed such that no heat plumes will interfere with the beam.

The entire optical path of the channel is outfitted with baffles between the optical components to avoid ghost images and to reduce the amount of stray light.

5.5. Software design of the Ba II 4554 / Hβ channel

Basically, the Ba II 4554 / Hβ channel is controlled by three computers. A local PC104 will communicate with the LCVR controller box, the Maxon interface and the Faulhaber motors. A separate machine accommodates the camera frame grabbers. The observations are controlled by the acquisition software running locally in the observing room. For the other channels this acquisition software only commands the required wavelength position of the filters and controls and synchronized the camera exposure and read-out. The new LCVR retardance tuning will be treated in the same way as the wavelength tuning of a filter. The requested wavelength or retardance is converted to a motor setting and a driving voltage respectively by the PC104. The controls of all the active components are multithreaded and therefore virtually simultaneous. Interpretation of a command from the acquisition software is executed with calibration tables present on the PC104. That means that these calibrations have to be performed separately before observations can take place. Also the camera response curve is measured before observations.

Calibration of the wavelength tuning is performed by tuning the filter through the line and comparing the obtained spectral profile of the defocused quiet Sun observations at disk center with an atlas profile. Calibration of the LCVRs is performed in a similar way by inserting the calibration polarizer into the beam and aligning it parallel and crossed with the Lyot filter's entrance polarizer. The defocused image of the quiet Sun at disk center is assumed to be unpolarized. Sweeping the voltage on the LCVRs (aligned at 45°) results in a curve as in figure 5.8.b. Calibration of the filters and the LCVRs involves direct communication between the PC104 and the frame grabbers. The acquisition software always assumes correct calibrations at the operating wavelength. The position (in or out of the beam) and the rotation of the LCVRs can be controlled by the acquisition software.

For calibrations of the LCVRs, first LCVR2 is inserted into the beam with its regular alignment (see figure 5.9) and the table of retardance as a function of the applied voltage at the operating wavelength is acquired with use of formula 5.1 and/or the determination of the extrema of the curves with parallel and crossed polarizers.

Both methods are only weakly dependent on non-linearity of the camera, but are still preferably performed in the linear regime of the camera. If the Lyot filter's entrance polarizer is rotated with respect to the regular alignment, the obtained calibration curve is automatically corrected due to the quarter wave plate. LCVR1 can be calibrated in the same way by inserting only this LCVR into the beam and rotating it so its alignment is now equal to that of LCVR2. It is also possible to leave the calibrated LCVR2 in the beam with ¼ wave retardance and calibrate LCVR1 at its original alignment with the calibration polarizer now rotated at 45° from the axes of LCVR1. The resulting calibration curve is then shifted by a ¼ wave.

The measurement of the instrumental Mueller matrix at both operating wavelengths is performed in the same way. Firstly, the degree of polarization due to the unpolarized light at defocused disk center is determined with the calibrated LCVRs to measure the cross-talk components $I \rightarrow X$. Next, a motorized rotating linear polarizer is inserted into the beam before BS1 to determine the maximal signal and therewith the axes of Q and U on the Sun as a function of the rotation of the polarization modulators. By measuring the full polarization state, the cross-talk components of Q and U to the other Stokes components are obtained. The system's retardation is directly obtained by redoing the calibrations of LCVR2 and LCVR1 at their original alignments with the rotating polarizer before BS1 as the calibration polarizer. The shifts of the acquired calibration curves are a direct measurement of the system's retardations in the Q and U direction. Finally a third LCVR is inserted between the rotating polarizer and BS1 to be able to produce circular polarization at both operating wavelengths. This LCVR0 is not in a thermally stable environment and has to be temperature controlled. It is calibrated in the same way as LCVR2 with the rotating polarizer aligned parallel and crossed with respect to the Lyot filter's entrance polarizer (with LCVR1,2 transported out of the beam). The obtained calibration curve then has to be corrected for the system's retardation. With LCVR0 at ¼ and ¾ wave, the calibration unit before BS1 now produces circular polarization, allowing a measurement of the cross-talk of Stokes V into the other Stokes components.

The obtained instrumental Mueller matrix has to be carefully interpreted to be able to reduce the amount of instrumental polarization by replacing components and correcting in first order with the settings of the LCVRs as described in the previous section. This will lead to cross-talk components of the order of 10%.

The observer can specify in the acquisition software which wavelength and retardance tuning settings are required for each 20 s Speckle burst. Each sub-burst is then Speckle reconstructed separately and aligned with information from the reconstruction channel. It is for instance advantageous to obtain observations in eight filter positions for Hα to fully characterize the spectral features of each resolution element within the typical solar change time. During the tuning of any filter in the multi-wavelength system, the frame grabbers are idle. It is therefore convenient to fit the tuning schemes of all channels to this eight interval scheme. For the Ba II 4554 / Hβ channel there are several options. Regular Dopplergram observations require observations in both line wings (see formula 3.1) and therefore the Lyot filter has to be tuned once each burst. Regular magnetogram observations require observations in right- and left-circular polarization (see figure 2.1 and equation 2.10.c) and therefore the setting of LCVR2 has to be changed once each burst. A hybrid scheme for both Dopplergrams and magnetograms is obtained by acquiring (I±V) in each line wing. This can be performed within a fourfold tuning scheme within one burst or by sequencing twofold Doppler bursts and Zeeman bursts if the seeing is only moderate anyway. Magnetograms in both line wings might yield additional magnetic information due to the possible asymmetry of the spectral signal in Stokes V (see figure 3.9). Also the mutual influence of the Doppler and the Zeeman signals can be investigated as discussed in section 3.1.3.

Measurements of Q and U at one spectral position in the line requires a tuning scheme of at least four settings (see figure 4.3.). Full Stokes measurements of the separate components require six settings, although a complete measurement of superposed components can be achieved with four settings.

It would be preferable to constantly modulate the LCVRs for each frame within the burst to counter waves of seeing. Unfortunately the current acquisition software is not accurate enough to synchronize the LCVR modulation with the camera read-out. A separate program may be devised to run on the PC104 that is able to directly control the frame grabber of the Ba II 4554 / Hβ channel to achieve this modulation.

As a test of the expected noise levels for the polarimetric observations, a regular unpolarized burst in the G band was split in half to represent I±X. The results for the sum of the two sub-bursts and the differences for different modulation schemes is presented in figure 5.11.

F.5.11.

Signal levels of the difference of sub-bursts with different processing techniques.
a) Sum of all the frames.
b) Difference of the first half of the frames and the last half.
c) Difference with frame-by-frame modulation.
d) Difference with aligned and rubbersheeted modulated frames.
Color schemes of b-d in percents of a.
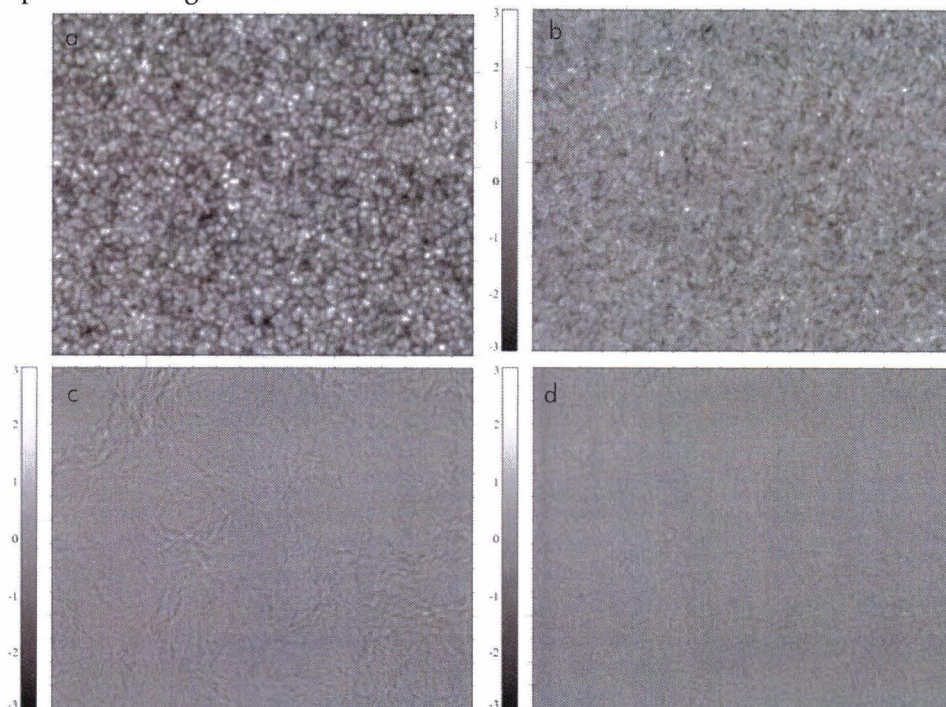
The noise signal in X/I from a half/half split is depicted in figure 5.11.b. The signal level is about 3%. The noise is considerably reduced by frame-by-frame modulating the I+X and I-X images as shown in figure 5.11.b. Here, the noise level is about 2%. After aligning and rubbersheeting of all the frames, the noise level drops to 1.2%. Unfortunately no test could be performed for the signal level of Speckle reconstructed bursts as no satisfactory two-channel datasets have yet been acquired with the reconstruction method of Keller & Von der Lühe (1992). Information from the reconstruction channel has to be used for alignment of the two Speckle reconstructed half-bursts or the remaining seeing disturbance will generate huge noise signals due to the signal gradients at high resolution. It is expected that the noise levels of aligned Speckle reconstructed magnetograms are similar to the signals of figure 5.11.a and b (for the different modulation schemes). The size of the spurious signals is reduced due to the increase in resolution. These signals may be distinguished from real polarization signals by performing the same reconstruction of the unpolarized frames of the reconstruction channel. The expected photon noise level will be higher in the Ba II 4554 / Hβ channel (~1%) due to the lower light levels.

To reduce the level of photon noise and spurious polarization, demagnification has to be applied to the both the Ba II 4554 / Hβ channel and its reconstruction channel. The signal will then increase by a factor of two (reducing the photon noise level by $\sqrt{2}$) and the effective burst duration will be increased by a factor of $\sqrt{2}$, of course at the expense of spatial resolution. If frames are co-added for much longer durations than the maximal time scale allowing for Speckle reconstruction such that the seeing will be fully sampled by the frames in both (I+X) and (I-X), the resulting image in Stokes X will not be subject to spurious polarization signals. The resolution of this image is determined by the point spread function of the seeing. A correlating rubbersheeting strategy (possibly with information from the reconstruction channel) may be adopted for more accurate co-adding.

When switching observations from Ba II 4554 to Hβ (e.g. in the case of a transient phenomenon as a flare), the settings of the motor that selects the prefilter, the motors rotating the Lyot filter's entrance and exit polarizers and the camera translation motor are changed to the desired new values separately from the acquisition software. Also the calibrations of the filter and the LCVR tuning have to be redone. The acquisition software only checks a flag that indicates if the current settings are for Ba II 4554 or for Hβ. The temperature of the Lyot filter has to be raised for correct operation at Hβ by manually adjusting the thermostat at the telescope platform. If this and the duration of the temperature stabilization takes too long for the observer, it can be decided to operate the filter at Hβ at the temperature of Ba II 4554 at the expense of ghost peaks in the spectral transmission.

6. Future observables

Assembly of the full Ba II 4554 /Hβ channel will be completed in May 2005. After installation on the telescope in June 2005, the system first has to be fully tested and minimized for instrumental polarization as described in section 5.5. Then the operation of the imaging polarimeter should be calibrated by accurate comparison with established polarimetric instruments as the SOUP filter (see Berger & Lites 2002) at the SST, the photospheric magnetograms of the SOLIS telescope (Keller et al. 2003) or the MDI instrument on board the SOHO satellite.

The observational capabilities of the Ba II 4554 /Hβ imaging polarimeter is a major extension to the current DOT configuration will cover a broad range of solar phenomena governed by magnetism.

The main observational mode of the Ba II 4554 /Hβ channel will be the production of Speckle reconstructed Dopplergrams and magnetograms with the extremely narrow-banded Lyot filter (see section 5.3.2.) as discussed in sections 3.1.1 and 3.1.3 respectively. Both Dopplergrams and magnetograms will form a powerful addition to the current DOT tomographic capabilities.

Due to its high atomic weight, the Barium line is particularly sensitive to systematic plasma velocities instead of thermal broadening and earlier observations by Sütterlin et al. (2001) show that Ba II 4554 Dopplergrams reveal a large amount of structure in the photospheric velocity pattern.

Spectropolarimetric measurements presented in section 3.1.2 show that despite its lower wavelength the Barium line has a steeper response to weak magnetic fields due to the longitudinal Zeeman effect (see section 2.2.1) than the frequently used magnetograph-line Fe 6302. This response is mostly caused by the steepness of the line wings of the unpolarized spectrum. The presence of the HFS components (which are present for 18% of the Barium atoms) possibly enhance the steepness and cause an asymmetry in the response of the blue and the red wing, but more realistic modeling is required to obtain an accurate curve of the expected signal strength in V/I as a function in the longitudinal field strength. The observed Zeeman properties make magnetograms obtained in Ba II 4554 an excellent diagnostic of magnetic features with field strengths lower than 1 kG and length scales in the order of 100 km, since the diffraction limit at 4554 Å allows observations at higher resolution than with other Zeeman sensitive lines with mostly longer wavelengths. More sensitivity can be achieved by implementation of a frame-by-frame modulation as discussed in section 5.5.

The expected signals strengths as a function of the magnetic topology are presented in figure 3.9. These signals will be slightly reduced by convolution with the filter profile (~9.5%). With an expected noise level derived from the tests of figure 5.11, the Ba II 4554 magnetograms will be able to discern polarization signals from longitudinal fields stronger than approximately 100 G with good seeing. The signal strength in sunspot umbrae will be to low to acquire sufficient signal to noise ratio in the Speckle reconstructed magnetograms. Furthermore, the transverse Zeeman will generally not generate enough signal to acquire Speckle reconstructed vector magnetograms.

It was unfortunately no possible to design an optical configuration for the Ba II 4554 / Hβ channel that is completely free of instrumental polarization and cross-talk. With compensating optical elements and the flexibility of the LCVRs as polarization modulators as described in sections 5.3.3 and 5.5 it is to be expected that the remaining cross-talk components are of the order of 10%. The magnetogram signals are therefore underestimated by not much more than 10%, which is in the same range of the accuracy of the determination of the magnetic field with a carefully modeled response curve due to their sensitivity to magnetic and velocity gradients. The combination of Dopplergrams and magnetograms as discussed in section 5.5 might enable an estimate of the mutual influences.

The magnetogram signal will saturate at absolute field strengths of about 1 kG as indicated in figure 3.9 for different angles between the magnetic field vector and the line of sight mostly due to Zeeman saturation and the destruction of the HFS. These saturation levels may therefore be used to measure inclination angles in sunspot penumbrae. But also for this diagnostic firstly a more accurate model has to be applied.

The imaging polarimeter is designed to be as flexible as possible to also furnish other polarimetric observations than the Ba II 4554 magnetograms. However, no compromises were made to the accuracy of the magnetograms.

Another promising feature of imaging polarimetry in Ba II 4554 is the exploration of the linearly polarized signals due resonance scattering and Hanle depolarization as discussed in section 2.2.2. Ba II 4554 has the strongest signal in the second solar spectrum (up to 1.5% for the upcoming solar minimum), which can be detected by aligning the direction of ±Q parallel to the solar limb (see section 5.3.3) and reducing the spatial resolution with the demagnification described in section 5.3.1. Some strong features may already be detected by taking bursts within the increased solar change time of 30 s and aligning and Speckle reconstructing the frames with information from the reconstruction channel. If the time restriction due to Speckle reconstruction is dropped, the signal strength can be considerably increased by co-adding lots of frames, optionally including correlating rubbersheeting with information from the reconstruction channel. Of course the resolution will then be determined by the seeing (~1"), but it still enables the mapping of magnetic structures due to the Hanle effect in the context of the other tomographic channels. If also Stokes U is included in the observations, those observed signals will be exclusively due to magnetic contributions after correction for instrumental polarization. For the Ba II 4554 line it will be interesting to explore the differences between the signals in the central peak and the two HFS peaks in figure 3.5, particularly when an accurate model of the respective responses becomes available.

The measurements of the low linear polarization degree will be hampered by the instrumental polarization. The induced degree of linear polarization (I→Q,U) has to be accurately known in the instrumental matrix. Also scattered light can cause significant linearly polarized signals when observing near the limb. The cross-talk from Stokes V→Q,U will be of the order of 10% and therefore the Hanle measurements at the 1% level will be contaminated by Stokes V signals in the 10% range. Therefore it is advisable to occasionally also obtain regular magnetograms between the Hanle measurements. These magnetograms can also serve as proxies of the transverse Zeeman effect, which also produces signals in the order of 1% for relatively weak radial field topologies near the limb. The demagnification may also enable the acquisition of vector magnetograms, but that will require further exploration and modeling.

Observations in Hβ will mainly form an additional diagnostic to Hα observations as discussed in section 3.2. Due to the higher frequency, Hβ reveals structures at a slightly lower formation height. Hβ is both a Zeeman sensitive and a Hanle sensitive line and therefore also polarimetry in Hβ can be used to analyze a wide range of phenomena in the upper chromosphere. The low signal strengths will probably not emerge from Speckle reconstructed polarimetric images.

Hβ is used for 'chromospheric' magnetograms, but the interpretation of the observed structures is hampered by a large photospheric contribution to the signal. Comparison with for instance G band and Hα images and photospheric magnetograms might enable distinguishing between the chromospheric signals and the photospheric signals.

Hanle measurements in Hβ at the 1% level can give information about the magnetic topology of prominences and spicules.

Beam impacts in flares are observed in Hβ (and in Hα Ellerman bombs), but such measurements are highly controversial due to the large sensitivity to a flare's large intensity and temporal gradients.

The flexibility of the Ba II 4554 / Hβ polarimeter allows the exploration of all these effects.

Most polarimetric observations with the Ba II 4554 / Hβ imaging polarimeter will be photon starved at 0.2" resolution. To significantly increase the number of photons, the aperture of the DOT has to be increased as proposed by Bettonvil et al. (2004). This "DOT++" upgrade is relatively straightforward as the telescope construction is large and strong enough to support a 1.4 m mirror. The multi-wavelength system remains intact and will be fed by a new secondary optics system including a low order AO system to counter the increased dependence on atmospheric turbulences. With a selection of the magnification value and the pupil stop, the observer can choose between observations at the new diffraction limit of 0.07" or at the current limit of 0.2" with triple signal strength. This upgrade will increase the polarimetric sensitivity by a much needed factor of 3. The Ba II 4554 magnetograms can still be produced at the telescope's diffraction limit and will show magnetic structures below 100 km.

An upgrade that can be implemented on a shorter time-scale is the replacement of the current cameras with more blue-sensitive 16 bit cameras that will sample the incident photon flux with more resolution and with a larger dynamic range than the current 10 bit cameras. Also the implementation of the accurate frame-by-frame synchronization of these cameras with the LCVR tuning needs to be explored.

7. References

Aleksandrovich, S.; Domishev, G.; Korovkin, A. & Skomorovsky, V. 1975, *Novaja Technika v Astronomii* **5**, p.34

Asensio Ramos, A.; Trujillo Bueno, J. & Collados, M. 2005, *ApJ* **623**, p.L57

Balasumabriam, K.S.; Christopoulou, E.B. & Uitenbroek, H. 2004, *ApJ* **606**, p.1233

Berger, T.E. & Lites, B.W. 2002, *SoPh* **208**, p.181

Berger, T.E.; Rouppe van der Voort, L.H.M.; Löfdahl, M.G.; Carlsson, M.; Fossum, A.; Hansteen, V.H.; Marthinussen, E.; Title,A. & Scharmer, G. 2004, *A&A* **428**, p.613

Bettonvil, F.C.; Sütterlin, P.; Hammerschlag, R.H.; Jägers, A.P.; Rutten, R.J. 2003, *SPIE* **4853**, p.306

Bettonvil, F.C.; Hammerschlag, R.H.; Sütterlin, P.; Rutten, R.J.; Jägers, A.P. & Snik, F. 2004, *SPIE* **5489**, p.362

Bianda, M.; Benz, A.O.; Stenflo, J.O.; Küveler, G. & Ramelli, R. 2005, *A&A* in press

Bommier, V.; Leroy, J.L. & Sahal-Bréchot, S. 1986a, A&A 156, p.79

Bommier, V.; Leroy, J.L. & Sahal-Bréchot, S. 1986b, A&A 156, p.90

Bommier, V.; Landi degl'Innocenti, E. & Sahal-Bréchot, S. 1989, *A&A* **211**, p.230

Bommier, V. & Molodij, G. 2002, *A&A* **381**, p.241

Born, M. & Wolf, E. 1975, *Principles of optics. Electromagnetic theory of propagation, interference and diffraction of light*, Oxford

Brown, A.; López Ariste, A.& Casini, R. 2003, *SoPh* **215**, p.295

Cauzzi, G.; Smaldone, L. A.; Balasubramaniam, K. S. & Keil, S. L. 1993, *SoPh* **146**, p.207

Casini, R. & Landi degl'Innocenti, E. 1994, *A&A* **291**, p.668

Casini, R. & Landi degl'Innocenti, E. 1996, *SoPh* **164**, p.91

Casini, R.; Bevilacqua, R. & López Ariste, A. 2005, *ApJ* **622**, p.1265

Cowley, C.R. & Frey, M. 1989, *ApJ* **346**, p.1030

Davidson, M.D.; Snoek, L.C.; Volten, H. & Dönszelmann, A. 1992, *A&A* **255**, p.457

Domínguez Cerdeña, I.; Kneer, F. & Sánchez Almeida, J. 2003, *ApJ* **582**, p.L55

Evans, J.W. 1949, *JOSA* **39**, p.229

Firstova, N. M.; Xu, Z. & Fang, C. 2003, *ApJ* **595**,p.L131

Gandorfer, A. 2000, *The Second Solar Spectrum. Volume I: 4625 Å to 6995 Å*, Zürich

Gandorfer, A. 2002, *The Second Solar Spectrum. Volume II: 3910 Å to 4630 Å*, Zürich

Gisler, D.; Feller, A. & Gandorfer, A.M. 2003, *SPIE* **4843**, p.45

Graham, J.D.; López Ariste, A.; Socas-Navarro, H. & Tomczyk, S. 2002, *SoPh* **208**, p.211

Hanaoka, Y. 2003, *ApJ* **596**, p.1347

Hénoux, J.-C. & Karlický, M. 2003, *A&A* **407**, p.1103

Holweger, H. & Müller, E.A. 1974, *SoPh* **39**, P.19

House, L.L. 1974, *PASP* **86**, 512, p.490

Jefferies, J.T.; Lites, B.W. & Skumanich, A. 1989, *ApJ* **343**, p.920

Jefferies, J.T. & Mickey, D.L. 1991, *ApJ* **372**, p.694

Keller, C.U. & Von der Lühe, O. 1992, *A&A* **261**, p.321

Keller, C.U.; Gschwind, R.; Renn, A.; Rosselet, A. & Wild, U.P. 1995, *A&A Suppl. Ser.* **109**, p.383

Keller, C.U. 2002, in *Astrophysical spectropolarimetry. Proceedings of the XII Canary Islands Winter School of Astrophysics*, Trujillo Bueno, J.; Moreno-Insertis, F. & Sánchez. F. (eds.) Cambridge, UK, p. 303

Keller, C.U.; Harvey, J.W. 7 Giampapa, M.S. 2003, *SPIE* **4853**, p.194

Keller, C.U.; Schüssler, M.; Vögler, A. & Zakharov, V. 2004, *ApJ* **607**, p.L59

Kemp, J.C.; Macek, J.H. & Nehring, F.W. 1984, *ApJ* **278**, p.863

Krivova, N.A. & Solanki, S.K. 2004, *AdSpR* **34**, p.361

Kushtal, G.I. & Skomorovsky V.I. 2002, *SPIE* **4900**, p.504

Landi degl'Innocenti, E. & Landi degl'Innocenti, M. 1973, *SoPh* **31**, p.299

Landi Degl'Innocenti, E. 1982, *SoPh* **77**, p.285

Landi Degl'Innocenti, E.; Bommier, V. & Sahal-Bréchot, S. 1987, *A&A* **186**, p.335

Landi Degl'Innocenti, E. & Bommier, V. 1993, ApJ 411, pL.49

Landi degl'Innocenti, E. 1998, *Nature* **392**, p.256

Landman, D.A. & Mongillo, M. 1979, *ApJ* **230**, p.581

Landman, D.A. 1983, *ApJ* **269**, P.728

Leenaarts, J. & Wedemeyer-Böhm, S. 2005, *A&A* **431**, p.687

Lin, H.; Penn, M.J. & Kuhn, J.R. 1998, *ApJ* **493**, p.978

Lin, H.; Kuhn, J. R. & Coulter, R. 2004, *ApJ* **613**, p.L177

Liu, Y,; Wang, J.; Yan, Y, & Ai, G. 1996, *SoPh* **169**, p.79

López Ariste, A. & Semel, M. 1999, *A&A Suppl. Ser.* **139**, p.417

López Ariste, A.; Tomczyk, S. & Casini, R. 2002, *ApJ* **580**, p.519

López Ariste, A.; Casini, R.; Paletou, F.; Tomczyk, S.; Lites, B.W.; Semel, M.;
    Landi Degl'Innocenti, E.; Trujillo Bueno, J. & Balasubramaniam, K.S. 2005,
    ApJ **621**, p.L145

Lyot, B. 1944, *Annales d'Astrophysique* **7**, p.31

Makita, M. 1986, *SoPh* **103**, p.1

Mein, P. 2002, *A&A* **381**, p.271

Mickey, D.L.; Canfield, R.C.; LaBonte, B.J.; Leka, K.D.; Waterson, M.F. & Weber,
    H.M. 1996, *SoPh* **168**, p.229

Neckel, H. 1999, *SoPh* **184**, p.421

Nikolsky, G.M.; Kim, I.S. & Koutchmy, S. 1982, *SoPh* **81**, p.81

Noyes, R.W. 1967, in *Aerodynamic Phenomena in Stellar Atmospheres*, R.N. Thomas (ed.),
    London, p.293

Polyakov, V.I. 1979, *SolD* **5**, p.86

Povel, H.P. 1998, in: *Astronomische Gesellschaft Meeting Abstracts, Abstracts of Contributed
    Talks and Posters presented at the Annual Scientific Meeting of the Astronomische Gesellschaft
    at Heidelberg, September 14-19*, talk #I07

Rees, D.E. 1982, *ProcASA* **4**(4), p.335

Rees, D. E. & Semel, M. D. 1979, *A&A* **74**, p.1

Ruiz Cobo, B. 1998, *Ap&SS*.**263**, p..331

Qu, Z.-Q. & Xu, Z. 2002, *CJAA* **2**, p.71

Rutten, R.J. 1977, *SoPh* **51**, P.3

Rutten, R.J. 1978, *SoPh* **56**, p.237

Rutten, R.J. & Milkey, R.W. 1979, *ApJ* **231**, P.277

Rutten, R.J. 1999, in: *High Resolution Solar Physics: Theory, Observations, and Techniques*,
    Rimmele, T.R.; Balasubramaniam, K.S.; & Radick, R.R. (eds.), *ASP Conf. Series* **183**,
    p.296

Rutten, R.J.; Hammerschlag, R.H.; Bettonvil, F.C.M.; Sütterlin, P. & de Wijn, A. G. 2004a,
    A&A **413**, p.1183

Rutten, R. J.; de Wijn, A. G. & Sütterlin, P. 2004b, *A&A* **416**, p.333

Rybicki, G.B. & Lightman, A. P. *Radiative processes in astrophysics*, 1979 (New York)

Sahal-Brechot, S.; Vogt, E.; Thoraval, S. & Diedhiou, I. 1996, *A&A* **309**, p.317

Sánchez Almeida, J. & Martinez Pillet, V. 1992, *A&A* **260**, p.543

Sánchez Almeida, J. 1997, *A&A* **324**, p.763

Scharmer, G.B.; Bjelksjo, K.; Korhonen, T.K.; Lindberg, B. & Petterson, B. 2003, *SPIE* **4853**,
    p.341

Schmieder, B. 1992, *SoPh* **141**, p.275

Shilova, N.S. 1966, *SvA* **10**, p.85

Shurcliff, W.A. *Polarized light; production and use* ,1962 (Cambridge MA)

Socas-Navarro, H. & Uitenbroek, H. 2004, *ApJ* **603**, p.L129

Socas-Navarro, H..; Trujillo Bueno, J. & Landi Degl'Innocenti, E. 2004, *ApJ* **612**, p.1175

Solanki, S. K.; Keller, C.U. & Stenflo, J. O. 1987, *A&A* **188**, p.183

Stellmacher, G. & Wiehr, E. 1994, *A&A* **290**, p.655

Stellmacher, G. & Wiehr, E. 2000, *SoPh* **196**, p.357

Stellmacher, G. & Wiehr, E. 2005, *A&A* **431**, p.1069

Stenflo, J.O., Harvey, J.W.; Brault, J.W. & Solanki, S. 1984, *A&A* **131**, p.333

Stenflo, J.O. *Solar Magnetic Fields; Polarized Radiation Diagnostics*, 1994 (Dordrecht)

Stenflo, J.O. 1997, *A&A* **324**, p.344

Stenflo, J.O. & Keller, C.U. 1997, *A&A* **321**, p.927

Stenflo, J.O.; Bianda, M.; Keller, C.U. & Solanki, S.K. 1997, A&A 322, p.985

Stenflo, J.O.; Gandorfer, A.; Holzreuter, R.; Gisler, D.; Keller, C.U. & Bianda, M.
    2002, *A&A* **389**, p.314

Stenflo, J.O. 2005, *A&A* **429**, p.713

Su, J. & Zhang, H. 2004 *SoPh* **222**, p.17

Sütterlin, P.; Rutten, R.J. & Skomorovsky, V.I. 2001, *A&A* **378**, P.251

Sykorski, J. & Merkulenko, V. E. 1988, *IGAFS* **83**, p.63

Tandberg-Hanssen, E. 1964, *ApJS* **9**, p.107

Tandberg-Hanssen, E. & Smythe, C. 1970, *ApJ* **161**, p.289

Trujillo Bueno, J. 2001, in *Advanced Solar Polarimetry: Theory, Observation and
    Instrumentation*, M. Sigwarth (ed.), *ASP Conf. Series* **236**, p.161

Trujillo Bueno, J.;, Casini, R..; Landolfi, M. & Landi Degl'Innocenti, E. 2002a, *ApJ* **566**, p.L53

Trujillo Bueno, J.; Landi Degl'Innocenti, E.; Collados, M.; Merenda, L. & Manso Sainz, R. 2000b, *Nature* **415**, 6870, p.403

Trujillo Bueno, J. 2003a, in *Stellar Atmosphere modeling*, Hubeny, I., Mihalas, D. & Werner, K. (eds.), *ASP Conf. Series* **288**, p.551

Trujillo Bueno, J. 2003b, in *Solar Polarization 3*, Trujillo Bueno, J. & Sánchez Almeida (eds.) ASP Conf. Series **307**, p.407

Trujillo Bueno, J., Shchukina, N. & Asensio Ramos, A. 2004, *Nature* **430**, 6997, p.326

Trujillo Bueno, J.; Merenda, L.; Centeno, R.; Collados, M. & Landi Degl'Innocenti, E. 2005, *ApJ* **619**, p.L91

Tziotziou, K.; Tsiropoula, G. & Mein, P. 2002, *A&A* **402**, p.361

Uitenbroek, H. & Bruls, J.H.M.J. 1992, *A&A* **265**, p.268

Uitenbroek, H. 2003, *ApJ* **592**, p.1225

Vogt, E. & Henoux, J.-C. 1996, *SoPh* **164**, p.345

Vogt, E. & Henoux, J.-C. 1999, *A&A* **349**, p.283

Vogt, E.; Sahal-Bréchot, S. & Hénoux, J.-C. 2002, in *Proceedings of the Second Solar Cycle and Space Weather Euroconference*, Sawaya-Lacoste, H. (ed.) ESA SP-477, Noordwijk, p.191

Wang, J.; Zhou, G.; Wang, Y. & Song, L. 2003, *SoPh* **216**, p.143

Westendorp Plaza, C.; del Toro Iniesta, J.C.; Ruiz Cobo, B.; Martinez Pillet, V.; Lites, B.W. & Skumanich, A. 1998, *ApJ* **494**, p.453

Wiehr, E. 1975, *A&A* **38**, p.303

Wiehr, E.1978, *A&A* **67**, p.257

Wiehr, E. 1981, *A&A* **95**, p.54

Wiehr, E. & Bianda, M. 2003, *A&A* **404**, p.L25

Ye, S.-H.; Jin, J.-H. 1987, *SoPh* **112**, p.305

Zharkova, V. V.& Kashapova, L. K. 2005, *A&A* **431**, p.1075

Zirin, H. 1962, *ApJ* **140**, P.1216

Zirin, H.; Liggett, M. & Patterson, A. 1982, *SoPh* **76**, p.387

Zhang, H. 1993, *SoPh* **146**, P.75

Zhang, H. & Zhang, M. 2000, *SoPh* **196**, p.269

Zhang, J. & Wang, J. 2000, *SoPh* **196**, p.377

8. Acknowledgements